UNIVERSITY OF CALIFORNIA,
IRVINE

Analyses of the Cellular Signaling Responses to DNA Damage and DNA Repair Factor
Recruitment Using Fluorescence Lifetimes and Fluctuations

DISSERTATION

submitted in partial satisfaction of the requirements
for the degree of

DOCTOR OF PHILOSOPHY

in Biomedical Engineering

by

Michael Masao Murata

Dissertation Committee:
Assistant Professor Michelle A. Digman, Chair
Professor Enrico Gratton
Professor Kyoko Yokomori

2018

DEDICATION

To my family

おかげさまで

TABLE OF CONTENTS

LIST OF FIGURES

Page

ACKNOWLEDGMENTS

I would like to first express my gratitude and appreciation for Dr. Michelle A. Digman for her years of guidance and support as my advisor. Because of the opportunities that she presented to me, I was able to learn and utilize advanced techniques in fluorescence spectroscopies for my research.

Much of this dissertation and my exploration of the DNA damage response would not have been possible without Dr. Kyoko Yokomori and Dr. Xiangduo Kong. My gratitude and admiration go to Dr. Yokomori for sharing her expertise in biology and mentoring me for a career in science research. To Dr. Kong, I offer my deepest thanks for your years of humble excellence in preparing samples that were the envy of my peers and providing the hands-on teaching that I needed.

I would also like to thank Dr. Enrico Gratton and the many members and visitors to the Laboratory for Fluorescence Dynamics over the years. It was only with Dr. Gratton's innovative analytical methods that I was able to conduct my research in ways that few other labs in the world could. To the other members and visitors to the LFD, I am thankful for the fruitful discussions and many coffee breaks that both advanced and provided relief from my research.

I am very grateful for the fellow members of the Digman lab. In particular, I would like to thank Linghao Kong for his intellectual curiosity that kept me motivated throughout our parallel journeys of scientific development, Dr. Jenu Chacko for his selflessness in sharing his expertise in physics and microscopy, and Andrew Trinh for challenging me to believe in the excellence and integrity of the scientific method and sharing the burden of a life in research.

Lastly, the pursuit of truth and knowledge is long and perilous, and I would not have been able to journey without my friends and family. I am very thankful to have had my partner Aimee Shimizu in my life to provide humor and companionship. I am grateful for my brother Eric, my sister-in-law Traci, and my nephew Alex who showed me how to prioritize the things in my life and supported my career in academia. Finally, everything that I am is because of my parents Paul and Arlene. Any number of words would be insufficient to describe their unwavering and overwhelming support and encouragement, but I am beyond fortunate to have them in my life for guidance and inspiration.

CURRICULUM VITAE

MICHAEL MASAO MURATA

EDUCATION

2018   Ph.D., Biomedical Engineering
University of California, Irvine

2016   M.S., Biomedical Engineering
University of California, Irvine

2013   B.S., Bioengineering and Materials Science and Engineering
University of California, Berkeley

RESEARCH EXPERIENCE

2014-2018   Graduate Student Researcher, *University of California, Irvine*
Laboratory for Fluorescence Dynamics
Advisor: Michelle A. Digman, Ph.D.

2011-2013   Undergraduate Student Researcher, *University of California, Berkeley*
Biologically-inspired Photonics-Optofluidics-Electronic Technology and
Science Group (BioPOETS)
Advisor: Luke P. Lee, Ph.D.

2010-2013   Undergraduate Student Researcher, *University of California, Berkeley*
Asian American and Pacific Islander Health Research Group
Advisor: Marilyn Wong, M.D., M.P.H.

2008   Research and Administrative Volunteer, *University of California, Los Angeles*
Asian American Network for Cancer Awareness, Research, and Training
Advisor: Marjorie Kagawa-Singer, Ph.D., M.N., R.N.

PUBLICATIONS

Murata, M. M., Kong, X., Hadraba, D., Yokomori, K., and Digman, M. A. Molecular dynamics of DNA repair factor recruitment using two-dimensional pair correlation of fluorescence fluctuations. *Manuscript in preparation.*

Kong, X., **Murata, M. M.**, Chacko, J., Yokomori, K., and Digman, M. A. Experimental measurement of the nanomechanical response of chromatin to a single DNA double strand break. *Manuscript in preparation.*

Murata, M. M., Kong, X., Moncada, E., Chen, Y., Wang, P., Berns, M. W., Yokomori, K. and Digman, M. A. NAD consumption by PARP1 in response to DNA damage triggers metabolic shift critical for damaged cell survival. *Manuscript submitted for publication.*

Murata, M. M., Kong, X., Moncada, E., Chen, Y., Wang, P., Berns, M. W., Yokomori, K. and Digman, M. A. (2018). NAD consumption by PARP1 in response to DNA damage triggers metabolic shift critical for damaged cell survival. bioRxiv 375212.

Kong, L.*, **Murata, M. M.***, Digman, M. A. (2018). Absence of REV3L promotes p53-regulated cancer cell metabolism in cisplatin-treated lung carcinoma cells. Biochemical and Biophysical Research Communications 496:199-204

Kong, L.*, **Murata, M. M.***, Digman, M. A. (2017). Restoring p53 Function and Silencing REV3L Suppresses the Cancerous Metabolic Phenotype in Cisplatin Treated Human Non-Small Lung Carcinoma Cells. bioRxiv 200816.

Jun, B.-H., **Murata, M.**, Hahm, E., and Lee, L. P. (2017). Synthesis method of asymmetric gold particles. Scientific Reports 7:2921.

* contributed equally

INVITED TALKS

Murata, M. M., Kong, X., Yokomori, K. and Digman, M. A. "Fluorescence Lifetime Mapping of NADH Reveals PARP1-Dependent Metabolic Shift in Response to DNA Damage." Gordon Research Seminar: Mammalian DNA Repair. San Buenaventura Ballroom, Four Points Sheraton, Ventura, CA. 18 February 2017.

Murata, M. M., Kong, X., Yokomori, K. and Digman, M. A. "Fluorescence Lifetime Mapping of NADH Reveals DNA Repair Activity and Epigenetic Regulation." Tsukuba Global Science Week 2016, University of Tsukuba. Conference Room 406, International Congress Center Epochal Tsukuba. 19 September 2016.

Murata, M. M., Kong, X., Yokomori, K. and Digman, M. A. "Fluorescence Lifetime Mapping of NADH Reveals DNA Repair Activity in Live Cells." 16th Annual UC Systemwide Bioengineering Symposium, Bioengineering Institute of California. Stevenson Room 150, UC Santa Cruz, Santa Cruz, CA. 23 June 2015.

ABSTRACT OF THE DISSERTATION

Analyses of the Cellular Signaling Responses to DNA Damage and DNA Repair Factor
Recruitment Using Fluorescence Lifetimes and Fluctuations

By

Michael Masao Murata

Doctor of Philosophy in Biomedical Engineering

University of California, Irvine 2018

Professor Michelle A. Digman, Chair

Genome integrity is continually challenged by threats including DNA replication
errors, toxic metabolic byproducts, and exposure to exogenous genotoxins. Responding to
and repairing damaged DNA requires coordinating a number of critical cellular events
including activating DNA repair, facilitating chromatin rearrangement, and delaying cell
cycle progression. Although the factors important for DNA repair have been identified, how
these activities are coordinated in the nucleus and the long-term cellular-wide
consequences of DNA repair are not well characterized.

Nicotinamide adenine dinucleotide (NAD) is a coenzyme involved in both cellular
metabolism and DNA repair. Thus, analyses of NAD species could provide new insight into
DNA damage signaling as well as damage-induced metabolic responses to various types of
DNA lesions. Here, we use the phasor approach to fluorescence lifetime imaging
microscopy in combination with genetically encoded fluorescent biosensors to measure
metabolic changes in single cells with high spatiotemporal resolution. We found that the
absence of the reversionless 3-like translesional synthesis DNA repair protein promotes
p53-mediated upregulation of oxidative phosphorylation (oxphos) in cisplatin-treated

H1299 lung carcinoma cells and increases cell sensitivity to this chemotherapeutic treatment. Furthermore, it has been well-documented that depletion of NAD+ leads to an overall metabolic collapse, but it is not clear whether or not regulating metabolism can overcome cell death pathways as a survival mechanism. We observe a PARP-dependent decrease in NAD species and an increased metabolic reliance on oxphos. In all, our analyses revealed a previously unrecognized long-term effect of DNA repair signaling on energy metabolism in DNA damaged cells.

Although the patterns of DNA repair protein redistribution following DNA damage have been systematically documented, understanding the complex response to damage requires the characterization of the molecular dynamics of these proteins with high spatiotemporal resolution. By using spatial pair cross-correlation function analysis in two-dimensions, we were able to visualize the barriers to molecular motion of DNA repair proteins in response to laser microirradiation-induced DNA damage.

In summary, my project utilized cutting-edge fluorescence dynamics techniques to reveal a connection between the DNA damage response and cellular metabolism and to develop a new method to characterize molecular diffusion in response to DNA damage.

CHAPTER 1

Introduction

1.1 Types of DNA Damage and DNA Repair

DNA as the molecule that preserves the genetic information plays a crucial role in our health and longevity. The integrity of this genetic material is continuously challenged by a variety of damaging events, which can number in the hundreds of thousands in a single cell per day[1,2]. During routine DNA replication, the DNA sequence can be spontaneously altered by the misincorporation of nucleotides, modification of bases via alkylation, and interconversion of bases via deamination. Cellular respiration and the inflammatory response can introduce reactive oxygen species such as hydroxyl radicals and superoxides, which are capable of introducing mutations. Furthermore, clinical treatments employing ionizing radiation can cause single strand breaks and double strand breaks in DNA. Importantly, damaged DNA cannot be replaced in the same way that defective proteins can be replaced by newly synthesized intact versions, and thus, it has to be repaired. As a result, there are a variety of mechanisms designed to preserve the integrity of the genome and together these comprise the DNA damage response (Figure 1.1)[3].
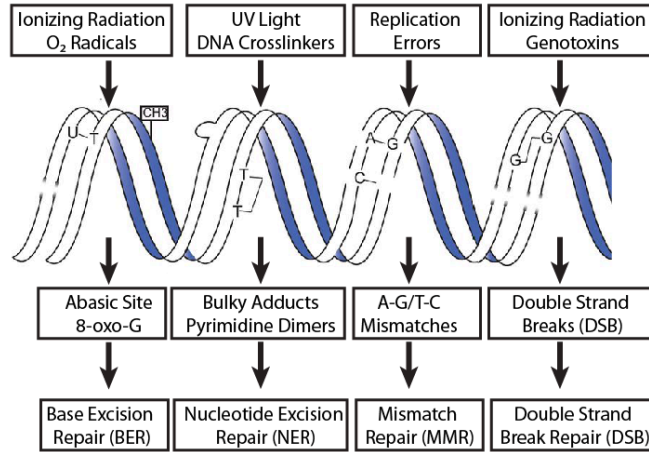
Figure 1.1. Types of DNA damage and DNA repair pathways[4] (Figure adapted from Ref 4).

Distinct lesion-specific pathways have evolved to address the varying types of DNA insults[5]. Mispaired DNA bases can be corrected through mismatch repair. Chemically altered bases can be replaced through base excision repair whereas more complex lesions such as intrastrand crosslinks and pyrimidine dimers can be addressed with nucleotide excision repair. Double strand breaks (DSBs) in DNA pose the greatest potential threat to genome stability as genetic information can be lost and apoptosis can be induced by a single unrepaired DSB, whereas base damages and single strand breaks are often rapidly repaired. The cellular response to DSBs is a multi-layered signal transduction pathway that includes DNA damage sensors, signal transducers, and repair factors, which combine to enhance the ability of an organism to survive.

1.2 DNA Damage Sensing by PARP-1

Studies in budding yeast have shown that a single persistent DSB can be detected and even initiate a global DNA damage response[6]. This reveals that the pathways involved in the DDR are sensitive and have a great capacity to amplify the signal in a rapid and

robust manner. One of the fastest sensors to arrive at a double strand break is the DNA

nick detector, poly(ADP-ribose) polymerase-1 (PARP-1). PARP-1 can bind to a variety of

DNA structures and once activated, is responsible for catalyzing the polymerization of ADP-

ribose moieties onto target proteins, termed poly(ADP-ribosyl)ation or PARylation[7,8]. This

rapid polymerization of ADP-ribose units to glutamate or aspartate residues functions as

the first post-translational modification in the response to DNA damage. The glycosidic

bonds between ribose units create a poly(ADP-ribose) (PAR) chain that can be linear or

branched. The resulting negatively charged polymer then acts as a scaffold for the

recruitment of other DNA repair factors including the Ku heterodimer and the MRN/ATM

complexes.

1.3 Double Strand Break Repair

DNA double strand breaks can be processed by two fundamentally different

pathways. The DSB ends can be rejoined with little or no processing as in non-homologous

end joining (NHEJ) or a homologous sequence can be used as a template for repair as in

homologous recombination (HR).

1.3.1 Non-Homologous End Joining (NHEJ)

The non-homologous end joining pathway repairs DSBs by directly ligating break

ends without using a homologous template. DNA ends are rapidly bound by the Ku

heterodimer (Ku70 and Ku80), an abundant nuclear protein that forms a ring to encircle

duplex DNA[9]. Upon DSB formation, a Ku heterodimer binds to each broken terminus to

form a bridging complex that stabilizes and aligns the DNA to promote end joining[10,11].

NHEJ is then initiated by the catalytic subunit of DNA-dependent protein kinase (DNA-PKcs)[12]. DNA-PK is a nuclear serine/threonine kinase that requires DNA as a cofactor for its phosphorylation activity. Once recruited by the Ku heterodimer, DNA-PKcs is responsible for a series of phosphorylation reactions that stabilize the ends and allow access for end processing enzymes while protecting the damage site from nucleolytic degradation. After DNA-PKcs is loaded, religation of the broken ends is carried out by XRCC4/Lig4. As a DNA damage dependent protein kinase, DNA-PK is particularly well-suited for DNA damage signaling and has been shown to target the tumor suppressor p53, which plays a key role in initiating apoptosis or halting the cell cycle[13,14].

1.3.2 Homologous Recombination (HR)

Homologous recombination (HR) or homology-directed repair utilizes a validating template to ensure accurate repair of damaged DNA sequences. The DSBs are recognized by the Mre11-Rad50-Nbs1 (MRN) complex, which indicates the activation of HR[15]. The Mre11 subunit stabilizes the DNA ends and has nuclease activity important for DNA end resection. Rad50 is a member of the structural maintenance of chromosomes (SMC) family and contains an ATPase domain that interacts with Mre11 and the DNA ends. Protein-protein interactions of the MRN complex are mediated by Nbs1 such as associations with ataxia telangiectasia mutated (ATM), a key effector in DNA repair signaling. The process of identifying the region of intact homologous DNA and facilitating strand invasion into the sister chromatid is mediated by Rad51[16]. The invading strand is then extended by DNA polymerases, annealed to the other end of the DNA break, and religated.

1.3.3 Differential Usage of NHEJ and HR

DNA repair is facilitated by a complex network of enzymes that can modify targets in a number of ways including phosphorylation, acetylation, ubiquitinylation, and PARylation. The significant number of factors allows for strict regulation of the modifications that can occur thereby directing repair choices in a precise way. Double strand breaks may need nucleolytic restructuring or can be directly ligated. Extensive condensation of chromatin may make homology search difficult if homologous chromosomes are even present at all. Although it often results in more accurate repair, HR is only active in the S/G2 phase of the cell cycle because it requires a homologous DNA template. In G1 phase, the only other available template would be the other homologous chromosome, but reliance on HR in this instance would lead to a gradual loss of heterozygosity[17]. Alternatively, because NHEJ directly ligates DNA ends, it is not restricted to a certain phase of the cell cycle and so higher eukaryotic cells use NHEJ more frequently than HR. The direct ligation of DNA ends, however, may result in chromosomal aberrations, translocations, and loss of nucleotides. Dissecting these decisions requires understanding the spatial and temporal coordination of these often-competing repair activities. The molecular mechanisms governing individual repair pathway choice have been intensively studied and recently, the focus of research in DNA repair has centered on how DNA repair signaling can coordinate activities throughout the entire cell.

1.4 The ATM Signaling Network in DNA Repair

One of the most critical signal transduction networks in DNA repair is mediated by the serine/threonine protein kinase ATM (ataxia telangiectasia mutated), the central regulator in a highly conserved protein kinase cascade (Figure 1.2)[18].
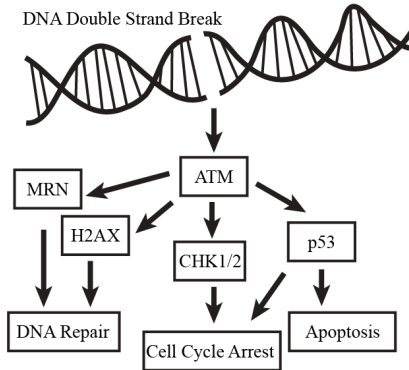
Figure 1.2. ATM signaling in DNA repair.

DNA end binding by Mre11 of the MRN (Mre11-Rad50-NBS1) complex responds to double strand breaks by activating several members of the PIKK (phosphatidylinositol 3-kinase-related kinases) family of protein kinases including ATM. When activated, ATM phosphorylates and modulates the activities of several key effectors in the DNA damage response including phosphorylating serine 139 on the histone variant H2AX in regions surrounding the double strand break[19]. This phosphorylation of H2AX, known as γH2AX, is one of the characteristic post-translational modifications in DNA repair that is highly associated with double strand breaks and easily visualized with immuno-fluorescence microscopy. The resulting γH2AX signal is recognized by MDC1 (mediator of DNA damage checkpoint protein 1) to facilitate the recruitment of additional MRN complexes to phosphorylate nearby H2AX thereby spreading the γH2AX signal and initiating a series of subsequent repair activity[20,21]. Furthermore, ATM phosphorylates mediator proteins, which amplify the DNA damage response by acting as recruiters of ATM substrates. These

targets are either phosphorylated directly by ATM such as the tumor suppressor p53 or

indirectly by downstream kinases such as the cell cycle checkpoint kinases, CHK1 and

CHK2[22]. Thus, the DNA repair signaling pathway mediated by ATM coordinates a variety of

cellular activities including the determination to undergo cell cycle arrest, initiate

apoptosis, regulate transcription, and activate DNA repair itself.

1.5 Cellular Metabolism and Links to DNA Repair Signaling

Biological functions have evolved to respond to the multitude of signals, conditions,

and external stimuli in order to maintain life. Central to the ability of cells to regulate

nearly every aspect of cellular behavior is the set of enzymatic reactions that comprise the

biochemical pathways in cellular metabolism, which facilitate the flow of energy between

energy-containing nutrients, intermediary metabolites, and cell macromolecules.

In order to fuel energy consuming processes such as DNA repair and chromatin

remodeling, cells harvest energy via catabolic reactions in cellular respiration[23]. The major

stages in the energy producing pathways are the breakdown of glucose to pyruvate in the

cytosol by glycolysis, the oxidation of acetyl-CoA in the citric acid cycle, and the

phosphorylation of ADP to ATP in the mitochondria by the electron transport chain.

1.5.1 Glycolysis

As its name implies, glycolysis is the degradation of a single glucose molecule into

two pyruvate molecules, a process that produces the high energy carrying metabolites, ATP

and NADH[23]. There are several steps and enzymes required to convert glucose into

pyruvate. The first step involves the phosphorylation of glucose by a family of enzymes

called hexokinases. The phosphorylation of glucose into glucose-6-phosphate (G6P) by

hexokinases serves to keep the concentration of glucose inside the cell low, which

promotes continuous transport of glucose into the cell and to prevent the export of excess

glucose since cells do not have transporters for G6P. Although HKs initially consume ATP

in glycolysis, the complete metabolism of glucose yields a net production of ATP and NADH.

Interestingly, hexokinases happen to be targets for PARP-1 and can be influenced by the

DDR[24]. When PARP-1 is activated by DNA damage, it PARylates hexokinases thereby

inhibiting their participation in the bioenergetic pathway.

1.5.2 Citric Acid Cycle

Several converging catabolic reactions result in the production of acetyl-coenzyme A

(acetyl-CoA), which is the starting point of the citric acid cycle[25]. The cyclic series of

reactions result in the production of the high-energy nicotinamide dinucleotide (NAD),

flavin adenine dinucleotide (FAD), and nucleoside diphosphate molecules[26]. Briefly,

pyruvate is decarboxylated in the mitochondrial matrix to form acetyl-CoA. Citrate

synthase converts acetyl-CoA into citrate by aldol condensation with oxaloacetate. Citrate

is then isomerized and oxidized to α-ketoglutarate and produces one molecule of NADH,

which is then decarboxylated to succinyl-CoA and produces another molecule of NADH.

Succinyl-CoA synthetase hydrolyzes succinyl-CoA to produce succinate and a nucleoside

diphosphate. A series of dehydrogenases regenerates oxaloacetate, which is able to re-

enter the citric acid cycle, and produces a molecule each of $FADH_2$ and NADH. Many of

these citric acid cycle intermediates are used elsewhere in the cell including the

mitochondrial electron transport chain and the nucleus. In particular, the DNA damage

response has been shown to cause post-translational modifications of proteins, which are driven by the availability of these intermediary metabolites[27,28].

1.5.3 Oxidative Phosphorylation

Oxidative phosphorylation using the electron transport system occurs on the cristae of the mitochondria and is closely linked with the citric acid cycle[29,30]. Indeed, succinate dehydrogenase, which catalyzes the oxidation of succinate to fumarate in the citric acid cycle, is bound to the inner mitochondrial membrane and reduces ubiquinone to ubiquinol in conjunction with its oxidative activity. The electron transport chain utilizes the energy stored in intermediary metabolites such as NADH to establish a proton gradient that drives the production of ATP by ATP synthetase. The first two complexes in the electron transport chain are NADH dehydrogenase (complex I) and succinate dehydrogenase (complex II). These enzymes catalyze the oxidation reactions that consume NADH to form NAD+, reduce ubiquinone into ubiquinol, and release protons into the intermembrane space of the mitochondria. The third complex is cytochrome c reductase (complex III), which shuttles electrons using the oxidation and reduction of ubiquinol and transfers protons into the intermembrane space. The final enzyme in the pathway is ATP synthetase, which uses a chemiosmotic gradient to drive the synthesis of ATP. These biochemical enzymatic reactions resulting the production of ATP provide the energetic molecules necessary for post-translational modifications of proteins in response to DNA damage, chromatin rearrangement for facilitating DNA repair, and initiating apoptosis, if necessary[27,31].

1.6 Overview of the Dissertation

This dissertation will focus on high spatiotemporal analyses of DNA damage response signaling and DNA repair factor recruitment. The factors important for DNA repair have been the subject of immense scrutiny, but away from the damage site, the long-term cellular-wide consequences of DNA repair and the coordination of DNA repair in the entire nucleus are not fully characterized. Here, we will investigate the relationship between DNA repair signaling and cellular metabolism as well as the molecular trajectories of DNA repair proteins in the nucleus using cutting-edge techniques in fluorescence dynamics.

Before we introduce our studies of DNA damage signaling and repair factor recruitment, Chapter 2 will first briefly review various methods for inducing DNA damage using chemicals and laser microirradiation. Then, advanced techniques in fluorescence microscopy with high spatiotemporal resolution will be introduced.

In Chapter 3, we will use the phasor approach to fluorescence lifetime imaging microscopy (FLIM) to gauge the response of p53-mediated metabolic regulation in response to cisplatin-induced intrastrand DNA crosslinks as a function of the reversionless 3-like translesional synthesis DNA repair protein. We will also discuss implications of this response for treatments using platinum-based chemotherapies.

The use of advanced fluorescence imaging technologies in combination with laser microirradiation and genetically encoded fluorescent biosensors to measure metabolic changes in single cells will be discussed in Chapter 4. The PARP-dependent role of metabolic regulation in cellular decision-making in damaged cells will be discussed.

Finally, the application of spatial pair cross-correlation function analysis in two-dimensions to DNA repair proteins will be discussed in Chapter 5. We will introduce and develop a quantitative method for visualizing the barriers to molecular motion of DNA repair proteins in response to laser microirradiation-induced DNA damage.

CHAPTER 2

Methods

2.1 Chemical Induction of DNA Damage

Free radicals can put oxidative stress on mammalian cells leading to mutagenesis and carcinogenesis. Hydroxy radicals in cells occur via the metal ion-dependent conversion from hydrogen peroxide generated by endogenous aerobic metabolism or exogenous exposure[32,33]. The overproduction of these oxidants can modify DNA bases or cause DNA-protein crosslinks that are typically repaired by base excision repair (BER), nucleotide excision repair (NER), or in some cases double strand break (DSB) repair. For DNA damage by oxidative stress, cells were treated with 500 µM hydrogen peroxide (H_2O_2) for 30 min prior to metabolic and cytotoxic analyses.

Methyl methanesulfonate (MMS) is a DNA alkylating agent that has been used to cause base mispairing by modifying guanine to 7-methylguanine and block replication by modifying adenine to 3-methyladenine[34]. These types of DNA lesions are primarily repaired by the base excision repair (BER) pathway and DNA alkyltransferases. For induction DNA damage via alkyation, cells were treated with 1 mM or 3 mM MMS for 1 hr prior to metabolic and cytotoxic analyses.

The anticancer drug *cis*-diamminedichloroplatinum (II) or cisplatin has been used as a potent treatment for esophageal, testicular, ovarian, and small cell lung cancers. When dissolved in aqueous solutions, water displaces the chloride ions generating a highly reactive electrophile that reacts with nucleophilic groups in nucleic acids such as N7 reactive center

in purines[35]. This results in adducts that disrupt the structure of DNA in a variety of ways including inter- and intra-strand crosslinks, DNA monoadducts, and DNA-protein crosslinks. Studies have shown that the majority of cisplatin-induced adducts are 1,2-intrastrand dGpG and dApG crosslinks, which cause severe local distortions in the DNA double helix[36]. These disruptions kink and unwind DNA leading to stalled DNA replication and apoptosis, but can be addressed by base excision repair (BER), nucleotide excision repair (NER), and mismatch repair (MMR). In addition, the translesion DNA synthesis (TLS) (to be described in Chapter 3) and homologous recombination (HR) pathways can respond to cisplatin-induced DNA lesions. To induce intra-strand crosslinks, cells were treated with 20 μM cisplatin (Sigma-Aldrich, St. Louis, MO) for the duration of the experiments.

2.2 DNA Damage Induction by Near Infrared Femtosecond Laser Irradiation

Ionizing radiation (IR) has been a powerful tool for imaging biological processes as well as for cancer therapies. However, it did not take long for researchers to discover the hazards of radiation. IR could be used both to induce and eradicate cancer, but the direct link between IR-induced DNA damage to mutation, development, and/or treatment of cancer is not easily identified. Advances in the understanding of DNA repair, cell signaling pathways, and genomics have presented opportunities for connecting DNA damage and repair events with potential health consequences by using lasers to manipulate and observe cellular events. In particular, there has been a large focus on researching DNA double strand break repair since it is a complex process involving a wide array of protein recruitment, post-translational modifications, and intricate cell signaling pathways. Thus, the laser micro-beam has developed as a precise tool to study DNA damage and repair.

There are a variety of chemical or ionizing radiation techniques to experimentally induce DNA double strand breaks[37,38]. However, these techniques introduce damage throughout the entire nucleus with poor time resolution since the damaging procedure can last up to 30 minutes. In order to effectively study the precise spatiotemporal kinetics of DNA repair, the induction and position of damage need to be highly defined. Focused laser light in the ultraviolet, visible, or near infrared spectrum has proven to allow for the requisite control over damage induction in time and space[39,40]. Another advantage of laser-induced DNA damage is that damaging events and subsequent monitoring can be achieved through the same imaging setup allowing for the detection of very fast processes. Recently, it has been reported that pulsed near-infrared light at 800 nm can induce DNA damage via three-photon absorption[41,42].

Although irradiation by near infrared radiation has already been shown to introduce highly localized DNA damage[42], it is important to characterize the cellular response to the system used for these experiments so as not to induce thermal heating and destruction of cellular structures. In these experiments, DNA damage induction and monitoring were performed on an inverted confocal Zeiss LSM710 (Carl Zeiss, Jena, Germany) or Zeiss LSM880 (Carl Zeiss, Jena, Germany) coupled to a titanium-sapphire 100 femtosecond pulsed laser (Spectra-Physics, Santa Clara, CA) at 80 MHz. A 40x 1.2NA water-immersion objective (Zeiss, Korr C-Apochromat) was used. DNA double strand breaks were induced via two-photon excitation irradiation tuned to a wavelength of 780 nm. Defined sub-micron linear tracts were bleached at a scan speed of 12.61 µs per pixel with 30%, 45% or 90% Zeiss LSM710 laser power corresponding to approximately 17.7 mW, 19.9 mW and 24.6 mW, respectively, of laser power measured after the objective.

Microirradiation on the LSM880 was performed at a scan speed of 16.38 μs per pixel with 35% Zeiss LSM880 laser power corresponding to approximately 22.6 mW of laser power measured after the objective. These microirradiation conditions have been optimized to specifically introduce DNA double strand breaks.

The laser power with respect to amount of DNA damage is calibrated by detecting DNA repair factor recruitment. Immuno-fluorescent staining for γH2AX and PAR confirms that double strand breaks were induced and that PAR chains were polymerized to damage regions (Figure 2.1A). The lowest damage condition resulted in the immediate phosphorylation of H2AX and the loss of signal within two hours of damage induction. As expected, rapid accumulation of PAR signal was detected within 5 minutes of damage induction but was not present an hour after damage due to rapid degradation by poly(ADP-ribose) glycohydrolase. The medium damage condition exhibited γH2AX signal at the damage site in the minutes following damage, which spread throughout the entire nucleus approximately 2 hours after damage and all signal was reduced 12 hours after damage. Pan-nuclear γH2AX signal at undamaged chromatin may be due to overactivation of the ATM and DNA-PK signaling pathways[43]. The accumulation of PAR signal was strongest at the damage site immediately after damage, but PAR was detected throughout the entire nucleus. PAR signal was not detectable within an hour after damage. For the highest damage condition, the nuclear wide spreading of γH2AX signal occurred within minutes and persisted beyond 12 hours after damage. Similarly, PAR was detected throughout the entire nucleus and gradually diminished over the course of 8 hours after damage.
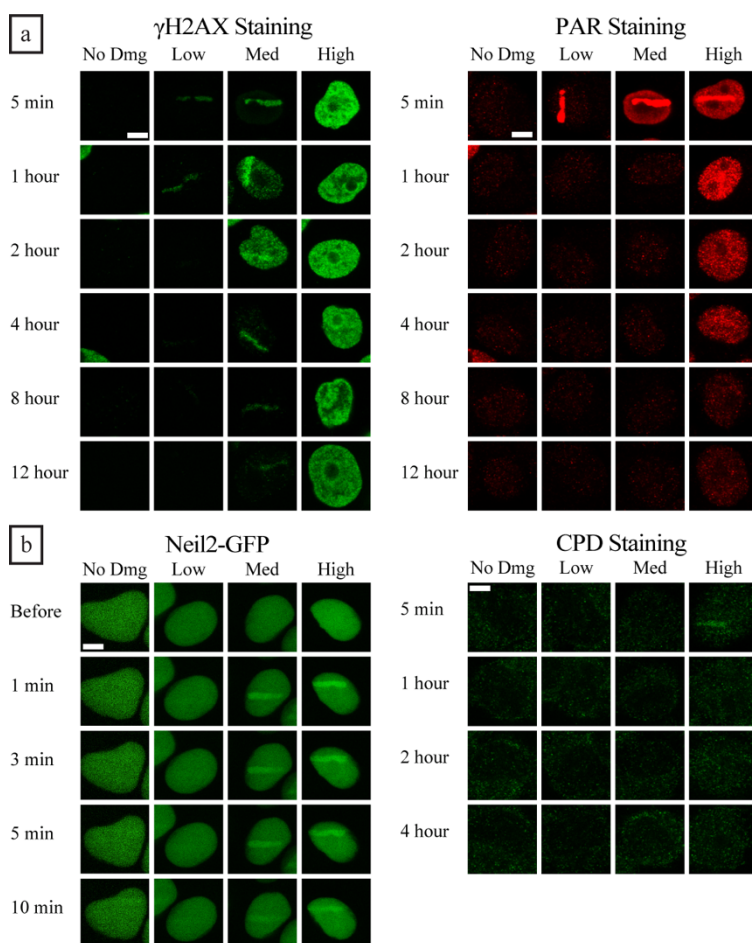
Figure 2.1. Characterization of Laser-Induced DNA Damage. *a) Immuno-fluorescent staining for γH2AX (left) and PAR (right) show that DNA damage has been induced and that DNA repair has been initiated. b) Accumulation of Neil2-GFP (left) and staining for CPD (right) at damage sites shows that complex DNA damage is introduced with high damage conditions. Scale bar = 5 μm.*

Analysis of DNA repair factors reveals that focused near infrared radiation can induce complex DNA damage (Figure 2.1B). The recruitment of the DNA glycosylase, Neil2, tagged with GFP shows that the medium and high damaging conditions can induce base damages in addition to strand breaks. Since base excision repair is very rapid, the recruitment of Neil2 to damage sites occurs within a minute following damage and dissipates within 15 minutes following damage in even the highest damage condition. Alternatively, staining for cyclobutane pyrimidine dimers (CPD) shows that the high

damaging condition can induce bulky DNA adducts, which are processed within an hour following damage. CPD are not detected with the low and medium damaging conditions indicating that DNA damage in these conditions is primarily strand breaks.

2.3 Phasor Approach to Fluorescence Lifetime Imaging Microscopy (FLIM)

Fluorescence lifetime refers to the amount of time between when incident radiation is absorbed and when it is emitted as fluorescence. The fluorescence lifetime of excited molecular species is a commonly used determinant for characterizing the physicochemical properties of emitting fluorophores such as protein conformation and local environment[44]. In this way, fluorescence lifetime can be used as a form of contrast to extract information about molecular activity in complement with emission spectra. The lifetime of a molecular species is determined by constructing a histogram of photon delays and mathematically fitting using an exponential model. For a fluorescent species capable of two conformations, a biexponential process should theoretically be observed. However, given the sensitivity of the lifetime value to microenvironments and the number of unique conformations, there are a number of challenges with interpreting fluorescence lifetimes using statistical fitting procedures[45].

The phasor approach to fluorescence lifetime imaging analysis allows for the examination of lifetime decays without exponential fitting and produces a graphical view of the fluorescence decay curves in each pixel of an image (Figure 2.2)[46].
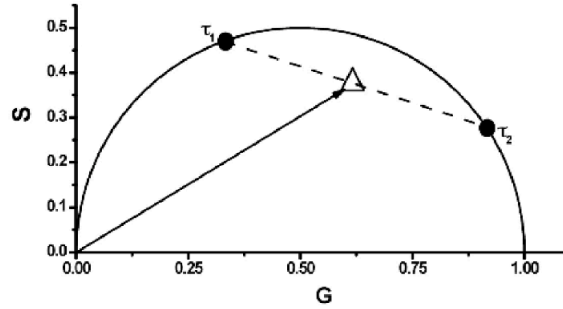
Figure 2.2. The phasor approach to FLIM analysis. *The phasor plot provides a graphical view of fluorescence decay curves in each pixel. Pixels with two pure species (triangle) can be analyzed using phasor addition to calculate the ratio of each component (τ_1 and τ_2).*

A Fourier transform is applied to the histogram of time delays in each pixel using the shown equations to generate coordinates in phasor space, which are represented on a polar plot in which lifetime magnitudes and complexity of decay curves can be easily observed. The vector coordinates in phasor space are given by:

$$g_{i,j}(\omega) = \int_0^\infty I_{i,j}(t)\cos(\omega t)dt \bigg/ \int_0^\infty I_{i,j}(t)dt$$

$$s_{i,j}(\omega) = \int_0^\infty I_{i,j}(t)\sin(\omega t)dt \bigg/ \int_0^\infty I_{i,j}(t)dt$$

where *I(t)* is the intensity decay curve, ω is the laser repetition angular frequency, and the indexes *i* and *j* identify each pixel in the image. Single exponential decays will appear on a "universal circle" and can be associated with a lifetime value whereas complex multi-exponential decays will be within the "universal circle". In the case of the auto-fluorescent coenzyme NADH, freely moving species have a lifetime of 0.4 nanoseconds whereas species bound to a substrate have a longer lifetime, such as 3.2 nanoseconds for NADH binding to lactate dehydrogenase. Once in phasor space, entire images can be analyzed based on lifetime where each point on the phasor plot can be mapped to its pixel on the original

image. In this way, fluorophores can be identified by its position on the phasor plot. For pixels containing some ratio of two pure species, the lifetime phasors are found within the circle between the two single exponentials as a linear combination in phasor space using vector addition and normalization using the following equations:

$$g_{i,j}(\omega) = \sum_k \frac{f_k}{1 + (\omega\tau_k)^2}$$

$$s_{i,j}(\omega) = \sum_k \frac{f_k\omega\tau_k}{1 + (\omega\tau_k)^2}$$

where f_k is the intensity weighted fractional contribution of the component with lifetime τ_k. In this way, the fractional contribution of each of the two species contributing to the phasor can be calculated. Previous research has used this method to study differentiation and metabolism[47-50].

2.4 Two-Dimensional Pair Cross-Correlation Function (2D-pCF) Analysis

The accessibility and diffusive routes of single molecules in submicron regions in an entire image can be described by the spatiotemporal cross-correlation of the fluorescence fluctuations between pairs of points using the two-dimensional pair correlation function (2D-pCF) analysis[51-53] (Figure 2.3A and B). The time of the maximum correlation indicates the average time a molecule takes to move from one point to the other and is inversely proportional to the diffusion coefficient (Figure 2.3C). In this way, this method is capable of providing single-molecule information without tracking individual particles since on average, only the same particle will be able to produce an average correlation between two different points for a given time delay.
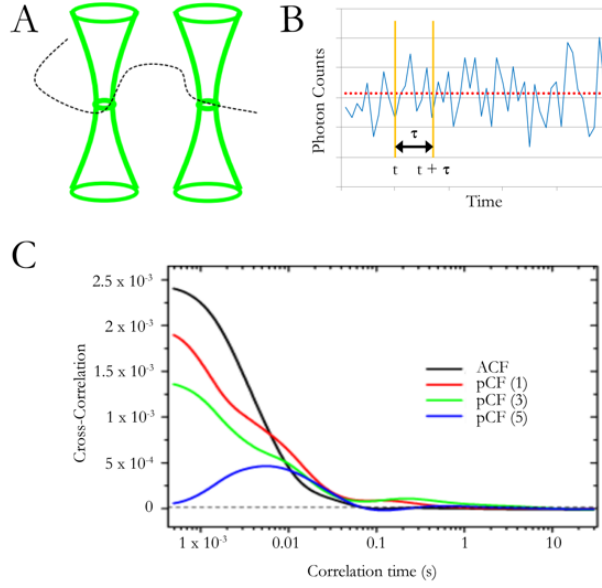
Figure 2.3. Analysis using the pair correlation function. *(A) Pair correlation function analysis cross-correlates fluorescence fluctuations between pairs of points. This can be accomplished via dual foci FCS (as shown), camera-based detection, or confocal laser scanning. (B) Fluctuations in intensity are correlated for time delays τ. (C). The time of the maximum correlation indicates the average time a molecule takes to move from one point to the other and is inversely proportional to the diffusion coefficient.*

The pair correlation function (pCF) for a point $\boldsymbol{r_0}$ = *(x₀, y₀)* in an image of a time series stack *I(**r**,t)* is calculated from the cross-correlation of fluorescence intensity measured at $\boldsymbol{r_0}$ with that measured at coordinates $\boldsymbol{r_1}$ = *(x₁, y₁)* according to

$$pCF = G(\tau, \boldsymbol{r_0}) = \frac{\langle I(t, \boldsymbol{r_0}) \cdot I(t + \tau, \boldsymbol{r_0} + \delta \boldsymbol{r}) \rangle_t}{\langle I(t, \boldsymbol{r_0}) \rangle_t \langle I(t, \boldsymbol{r_0} + \delta \boldsymbol{r}) \rangle_t} - 1$$

where $\langle ... \rangle_t$ indicates the temporal average, $\delta \boldsymbol{r}$ = $\boldsymbol{r_1}$ - $\boldsymbol{r_0}$, and τ is the time delay. The amplitude of the pCF reaches a maximum at the time delay τ that represents the average time it takes for a fluorescent particle to travel between $\boldsymbol{r_0}$ and $\boldsymbol{r_1}$. Obstacles to diffusion will increase the time delay of the pCF and can even result in the absence of correlation such as in the case of impenetrable barriers. Furthermore, the average path of molecular diffusion in a region and the presence of any barriers to this motion can be determined by

calculating the pCF at every point in a two-dimensional (2D) image and evaluating the deformation of the pCF in all directions. Whereas isotropic diffusion yields similarity in the pCF calculations for angles about r_0, a spatially heterogeneous environment that influences molecular trajectories produces asymmetry in the pCF depending on the direction of the obstacle. Thus, parameters that describe the shape of the pCF at each pixel in a 2D image can be used to visualize average molecular trajectories in a cell.
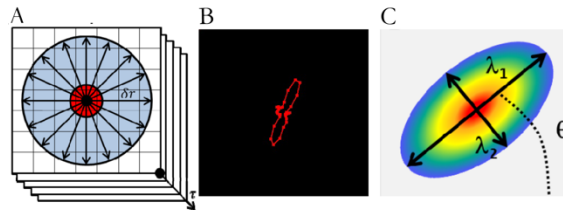
Figure 2.4. Calculation of the 2D-pCF. *(A) Fluorescence fluctuations are correlated at a given distance δr and sampled at 32 angles about each point. (B) Distortion of the 2D-pCF indicates the presence of barriers to motion. (C) The anisotropy of diffusion is quantified using the major and minor axes of the ellipse generated from the first and second order moments of the 2D-pCF distribution.*

To calculate the 2D-pCF, fluorescence fluctuations are correlated at a given distance δr and at different angles around the given point r_0 (Figure 2.4A). The result of the 2D-pCF calculations is a three-dimensional (3D) matrix containing the correlations at time delays τ in log scale for every pixel in the image. In order to reduce the size of this 3D matrix in the experiments conducted herein, the 2D-pCF is sampled on a polar grid $(\delta r, \theta_i)$ where δr is fixed at 6 pixels and θ_i only taking values of $0, \pm\pi/16, \pm\pi/8, \pm3\pi/16... \pm7\pi/8, \pm15\pi/16$, and π for a total of 32 angles (Figure 2.4B). The angular representation of the 2D-pCF is then described by

$$Anisotropy = \frac{\lambda_1 - \lambda_2}{\lambda_1 + \lambda_2}$$

where λ_1 and λ_2 correspond to the major and minor axes of the ellipse generated from the first and second order moments of the 2D-pCF distribution (Figure 2.4C). The resulting

anisotropy value in the range from 0 to 1 indicates the extent of asymmetry in the 2D-pCF ranging from pure isotropic diffusion to pure anisotropic motion, respectively. As determined previously, anisotropies below 0.15 are considered random isotropic diffusion and anisotropies nearing 1 represent increasingly preferred diffusive motion along the major axis of the 2D-pCF ellipse[53]. To only examine regions exhibiting highly anisotropic behavior, the lower threshold for anisotropy was set at 0.3 for analysis. By considering the above-threshold anisotropy values with the angle of the anisotropy direction, the average trajectories of molecules along diffusive paths shaped by penetrable and impenetrable barriers can be visualized by joining line segments that correspond to the major axis of the 2D-pCF. The resulting "connectivity map" provides a high spatial resolution image of the pattern of molecular flow in the cell.

To quantify the preferential orientation of anisotropy in sub-nuclear regions of interest (i.e. damage region, region surrounding damage site, non-damaged region, and nucleolus), the angles θ of the anisotropy were grouped into a normalized histogram and represented by the von Mises probability density function. The parameter κ measures the dispersion of the frequency of angles such that the value 0 suggests a uniform distribution of angles of anisotropy. An increase in the κ value indicates that angles θ become clustered around the mean direction μ and thus, a higher level of preferential orientation in the sub-nuclear region. The analysis was performed in MATLAB (2017a, Mathworks, Natick, MA, USA).

CHAPTER 3

Absence of REV3L Promotes p53-regulated Cancer Cell Metabolism in Cisplatin-treated Lung Carcinoma Cells

3.1 Abstract

Lung cancer is one of the deadliest cancers in the world because of chemo-resistance to the commonly used cisplatin-based treatments. The use of low fidelity DNA polymerases in the translesional synthesis (TLS) DNA damage response pathway that repairs lesions caused by cisplatin also presents a mutational carcinogenic burden on cells that needs to be regulated by the tumor suppressor protein p53. However, there is much debate over the roles of the reversionless 3-like (REV3L) protein responsible for TLS and p53 in regulating cancer cell metabolism. In this study, the fluorescence lifetime of the metabolic coenzyme NADH reveals that the absence of REV3L can promote the p53-mediated upregulation of oxidative phosphorylation in cisplatin-treated H1299 lung carcinoma cells and increases cancer cell sensitivity to this platinum-based chemotherapy. These results demonstrate a previously unrecognized relationship between p53 and REV3L in cancer cell metabolism and may lead to improvements in chemotherapy treatment plans that reduce cisplatin resistance in lung cancer.

3.2 Introduction

Lung carcinoma is one of the deadliest cancers in the world[54]. Cisplatin-based combination chemotherapy is one of the most common methods for managing and treating

lung cancer. Cisplatin reduces cancer cell proliferation by creating DNA crosslinks that stall

replication forks, which are highly toxic to rapidly dividing cells. The covalent bonds

formed at these crosslinks inhibit motion of DNA polymerases at replication forks, forcing

the polymerases to be ejected from the DNA strand[55]. These DNA adducts initiate the DNA

damage response (DDR), activating the tumor suppressor protein p53. Activation of p53

leads to processes that regulate metabolism, limit proliferation, and resist carcinogenesis[56].

Accumulation of cisplatin adducts repeatedly activates DNA damage signaling, which

reduces cyclin-dependent kinase activity leading to cell cycle arrest[2].

Patients typically have favorable initial responses to cisplatin-based regimens, but

these are brief and offer only marginal improvement due to the development of

chemotherapy-resistance. Several mechanisms of resistance have been proposed,

including changes in DNA methylation, alterations of membrane protein trafficking, and

increased DNA repair[57]. In particular, the activation of DNA damage responses at DNA

lesions such as cisplatin-induced crosslinks prevent replication fork collapse and promote

survival, eventually leading to cisplatin resistance[58]. These bulky DNA lesions are

processed by translesional DNA synthesis (TLmS) and mediated by specialized DNA

polymerases, such as Pol ζ. Unlike the highly accurate DNA polymerases used in

replication, such as Pol δ, Pol ζ has low fidelity nucleotide insertion. The reversionless 3-

like (REV3L) protein is the catalytic subunit of Pol ζ that is responsible for TLS[59]. REV3L

has been shown to increase cancer cell viability, especially following cisplatin-induced

damage[60-62].

The use of low fidelity DNA polymerases in TLS presents a mutational carcinogenic

burden on cells that needs to be regulated by the tumor suppressor protein p53. In

addition to suppressing TLS, p53 has many key functions in resisting carcinogenesis including cell cycle arrest, apoptosis, and metabolic regulation. Without p53, cancer cells can proceed with high rates of unregulated glycolysis, known as the Warburg effect and is one of the hallmarks of cancer[63]. This p53-mediated regulation of metabolism occurs through its promotion of target genes such as glutaminase 2 and TIGAR to upregulate oxphos and down-regulate glycolysis, respectively[64]. Furthermore, REV3L may also be involved in metabolic regulation, but its effects on metabolism are still debated with some studies suggesting that REV3L increases reliance on glycolysis and others demonstrating that it promotes oxphos[61,65]. Because one of the hallmarks of cancer cells is Warburg metabolism, understanding the mechanisms that limit the cancerous metabolic phenotype may lead to improvements in chemotherapy treatment plans that reduce cisplatin resistance in cancer cells. Indeed, the expression of p53 in p53-null cisplatin-resistant cell lines has been shown to increase sensitivity to cisplatin[66]. In this study, the absence of REV3L can promote the p53-mediated upregulation of oxphos in cisplatin-treated H1299 lung carcinoma cells and increases cancer cell sensitivity to this platinum-based chemotherapy.

3.3 Materials and Methods

3.3.1 Cell Culture, Plasmids, Transfections, and Treatments

H1299 cells (ATCC) were cultured in RPMI (Invitrogen, Carlsbad, CA) supplemented with 10% fetal bovine serum (FBS) and 1% penicillin-streptomycin. Cells were trypsinized and plated at 60-80% confluency on a glass-bottomed imaging dish. The EGFP and p53-GFP

plasmids are commercially available through Addgene while the p53-R175H-GFP plasmid was kindly constructed and provided by Dr. Lee Bardwell and Dr. Jane Bardwell in the Department of Developmental and Cell Biology at the University of California, Irvine. Lipofectamine 3000 (Invitrogen, Carlsbad, CA) was used to transfect according to manufacturer's instructions. Cells were incubated at 37°C and 5% CO_2 for 12-24 hours prior to imaging. To induce intra-strand crosslinks, cells were treated with 20 μM cis-diamminedichloroplatinum (II) (cisplatin) (Sigma-Aldrich, St. Louis, MO) for the duration of the experiments. For inhibition of oxidative phosphorylation, cells were treated with 10 μM rotenone and 10 μM antimycin A (Sigma-Aldrich, St. Louis, MO) in 0.35% DMSO for 1 hour prior to imaging. For inhibition of glycolysis, cells were treated with 20 mM 2-deoxy-D-glucose and 5 mM dichloroacetate (Sigma-Aldrich, St. Louis, MO) for 6 hours prior to imaging.

3.3.2 shRNA, siRNA, and Western Blot

Short hairpin RNA (shRNA) against REV3L (shREV3L) (pSuperior.puro-shREV3-4, Addgene #38029) and short interfering RNA (siRNA) against REV3L (siREV3L) (UrCUrGrGrCrGrCUrGUrCrArArGUUCTT) were used to silence the *REV3L* gene. The shRNA control (shControl) is commercially available at Sigma and the siRNA control (siControl) is commercially available at QIAGEN. Transfections of shRNA and siRNA were done following DNA plasmid transfection but had identical steps, with shRNA or siRNA in lieu of the DNA plasmid. 1 μg of shRNA or 1 μL of 20 μM siRNA was used for the transfection of each imaging dish. 24 hours after shRNA transfection, 2.0 μg/mL puromycin RPMI 1640 media was applied for 24 hours to select for successfully transfected

shRNA cells. Cells were harvested for Western blot analysis or imaged approximately 24 hours after the final transfection. Whole cell lysates prepared with RIPA buffer were subjected to SDS-PAGE followed by Western blot analysis with the anti-REV3L antibody (MyBioSource) and the anti-β tubulin antibody (Sigma-Aldrich, St. Louis, MO) for the loading control.

3.3.3 Instrumentation and Data Analysis

Confocal and fluorescence lifetime imaging microscopy (FLIM) experiments were performed on an inverted confocal Zeiss LSM710 (Carl Zeiss, Jena, Germany) with a 40x 1.2NA water-immersion objective (Zeiss, Korr C-Apochromat). Green fluorescent protein (GFP) excitation was achieved using a one-photon argon ion laser at 488 nm and emission was captured at 500-600 nm. In FLIM experiments, a Mai Tai titanium-sapphire 100 femtosecond pulsed laser at 80 MHz (Spectra-Physics, Santa Clara, CA) was used for sample excitation. An ISS A320 FastFLIM box (ISS, Champaign, IL) and a photomultiplier tube (H7422P-40, Hamamatsu Photonics, Hamamatsu, Japan) were used for data acquisition. FLIM images were acquired at 740 nm two-photon excitation with image sizes of 256x256 pixels and a scan speed of 25.21 μs/pixel. Fluorescence signal was captured at 420-500 nm for NADH auto-fluorescence. Instrument response time was referenced using coumarin-6 in pure ethanol, which has a known single exponential lifetime of 2.5 ns. FLIM data was processed in the SimFCS software developed at the Laboratory for Fluorescence Dynamics, University of California, Irvine as previously described[46].

3.3.4 Cell Viability Assay

Cells were plated onto gridded imaging dishes to determine cell survival following cisplatin treatment using morphology. Cell viability was measured by vital dye exclusion by propidium iodide (0.8 µg/mL) and total cell count was determined by Hoechst 33342 (0.5 µg/mL).

3.4 Results

3.4.1 Tumor suppressor p53 upregulates oxidative phosphorylation in H1299 cells

The tumor suppressor p53 has been known to regulate metabolism through the upregulation of oxphos and the downregulation of glycolysis. In some situations, however, it has also been known to upregulate glycolysis[56]. We first sought to elucidate the impact of p53 on the fraction of protein-bound NADH in H1299 cancer cells, which can be indicative of the overall metabolic state of the cell. The p53-null H1299 lung carcinoma cells were transfected with wild type p53 (p53-GFP) or the EGFP control. Fluorescence lifetime data of NADH in H1299 cells was acquired to observe changes in the fraction of bound NADH. Previous studies have demonstrated that the phasor approach to fluorescence lifetime analysis provides a graphical representation of lifetime data and by using 740 nm excitation with a bandpass filter, the fluorescence signal from NADH can be isolated. Here, FLIM data of NADH was collected and transformed to coordinates on the phasor plot as previously described (Figure 3.1A)[46]. Once the phasor positions of freely floating NADH and protein-bound NADH are established, the fraction of bound NADH can be determined by the linear combination of the phasors, which follow the rules of vector addition[67].

Images were pseudo-colored based on the fluorescence lifetime along this linear combinatorial trajectory with shorter lifetimes colored red and longer lifetimes colored white to illustrate free and bound NADH, respectively. Brightfield images for both EGFP and p53-GFP cells were taken to demonstrate the nuclear localization of p53 (Figure 3.1B). Pseudo-colored FLIM images of H1299 cells shows the sub-cellular distribution of NADH and that p53 induces a shift toward bound NADH in the cytoplasmic and nuclear compartments. H1299 cells expressing p53 exhibited a significantly higher fraction of bound NADH relative to control p53-null cells. This difference was observed in both the nuclear and the cytoplasmic sub-cellular compartments (Figure 3.1C).
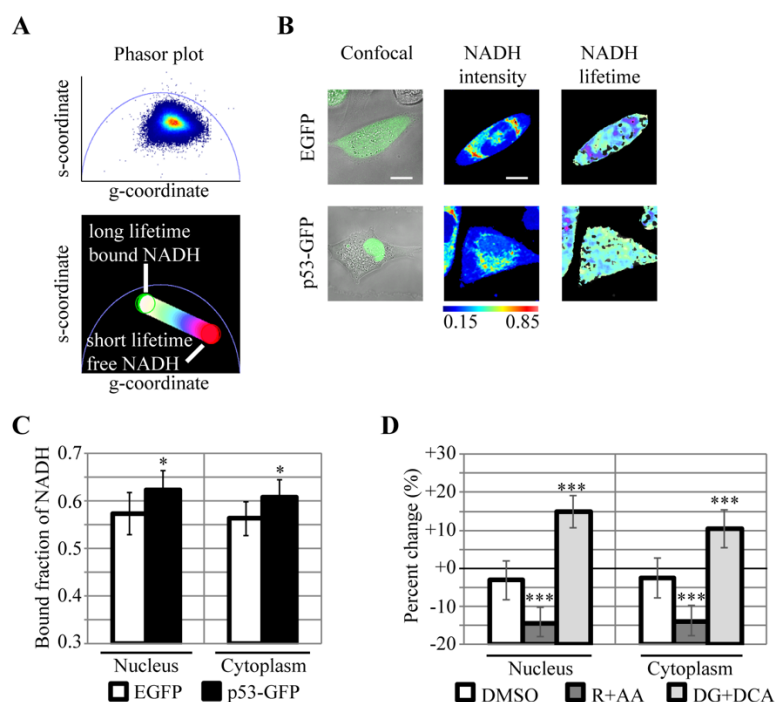
Figure 3.1. p53 promotes oxidative phosphorylation. (A) The fluorescence lifetime histogram on the phasor plot shows the distribution of lifetimes of autofluorescent NADH. A color spectrum indicates the bound fraction of NADH. (B) Fluorescence intensity images of GFP of an EGFP cell and p53-GFP cell (left panels). Normalized fluorescence intensity images of NADH (middle panels) and pseudo-colored FLIM images (right panels) of H1299 lung cancer cells transfected with EGFP and p53-GFP. Pseudo-coloring corresponds to the phasor position according to the color spectrum in Figure 3.1A. Scale bar = 10μm. (C) Bar graphs quantifying the bound fraction of NADH in the nucleus (left) and cytoplasm (right). (D) Percent change in bound fraction of NADH in the nucleus (left) and cytoplasm (right) after treatment with DMSO, rotenone and antimycin A (R+AA), or 2-deoxy-D-glucose and dichloroacetate (DG+DCA). * p<0.05, *** p<0.001, N>7.

To determine whether or not the fraction of bound NADH reflects the cellular metabolic state of H1299 cells, combinations of mitochondrial and glycolytic inhibitors were used as demonstrated previously[68]. For inhibition of mitochondrial oxidative phosphorylation, 10 μM rotenone and 10 μM antimycin A (R+AA) were used to disrupt the electron transport chain at the NADH dehydrogenase and coenzyme Q – cytochrome c reductase, respectively. To inhibit glycolysis, 20 mM 2-deoxy-D-glucose and 5 mM dichloroacetate (DG+DCA) were used to prevent the processing of glucose and to increase pyruvate intake for mitochondrial respiration. Following R+AA treatment, there was a highly significant percent decrease in the bound fraction of NADH relative to basal levels suggesting that a high fraction of bound NADH reflects increased oxidative phosphorylation relative to glycolysis (Figure 3.1D). Following DG+DCA treatment, there was a highly significant percent increase of the fraction of bound NADH for cells treated with DG+DCA relative to basal levels while control cells exhibited no significant changes in the fraction of bound NADH. Thus, for H1299 cells, a higher fraction of bound NADH corresponds to increased rates of oxidative phosphorylation relative to glycolysis, which is consistent with previous studies linking the lifetime of NADH to energy metabolism[67]. Together, the data suggest that investigating the fraction of bound NADH by FLIM can describe cellular metabolism and that p53 upregulates oxidative phosphorylation in H1299 cells.
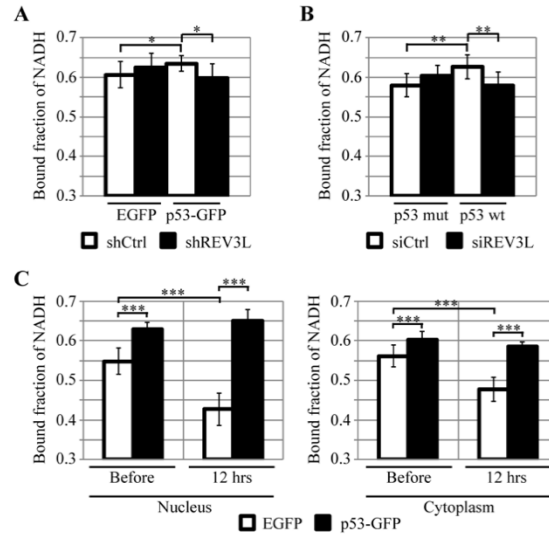
Figure 3.2. REV3L is necessary for metabolic regulation by p53. *(A) The fraction of bound NADH in H1299 cells after manipulation of p53 by transfection and REV3L by shRNA. (B) The fraction of bound NADH after transfection of wild type p53-GFP (p53 wt) or p53-GFP with the R175H mutation (p53 mut) and depletion of REV3L by siRNA. (C) The fraction of bound NADH before cisplatin treatment and with 12 hours of continuous exposure to cisplatin in the nucleus (left) and in the cytoplasm (right). * p<0.05, ** p<0.01, *** p<0.001, N>7.*

3.4.2 REV3L is necessary for p53 metabolic regulation

Previous studies suggest that REV3L may have an impact on glycolysis and oxphos in cancer cells, but its effects are still debated[61,65]. To investigate the effect of REV3L and p53 on cellular metabolism, p53-null H1299 cells and H1299 cells expressing p53 were depleted of REV3L via short hairpin RNA (Appendix A.1). Depletion of REV3L in p53-null H1299 cells did not significantly change the fraction of bound NADH relative to control cells (Figure 3.2A). The expression of p53 in H1299 cells exhibited an increase in the fraction of protein-bound NADH relative to p53-null control cells, demonstrating the upregulation of oxphos by p53 as in Figure 3.1C. The depletion of REV3L by shRNA in p53-expressing cells, however, caused a significant decrease in the fraction of bound NADH relative to cells with functional REV3L. The decrease in protein-bound NADH suggests that oxphos is suppressed in the REV3L-depleted and p53-expressing H1299 cells relative to

REV3L-expressing and p53-expressing cells demonstrating that REV3L is involved in metabolic regulation by p53. To investigate the effect of mutated p53 as commonly found in cancers, p53 with the R175H hotspot mutation (p53 mut) was expressed in H1299 cells and REV3L was depleted via small interfering RNA. As in Figure 3.2A, the fraction of bound NADH was not significantly affected by siREV3L alone, but increased with the expression of wild type p53 (Figure 3.2B). Depletion of REV3L in wild-type p53-expressing cells exhibited a decrease in the fraction of protein bound NADH suggesting that REV3L is necessary for the upregulation of oxphos by p53. Together, the results demonstrate a link between REV3L and p53 in regulating cellular metabolism in H1299 cells.

3.4.3 p53 maintains oxphos in response to cisplatin-induced DNA damage

The role of p53 in response to cisplatin-induced DNA damage is still debated with some studies suggesting p53 suppresses apoptosis while others demonstrating it promotes apoptosis[69]. Here, we investigate cellular metabolism via the fraction of bound NADH in p53-null H1299 cells and p53-expressing H1299 cells continuously treated with cisplatin for 12 hours. The fraction of bound NADH in both the nucleus and cytoplasm of p53-null H1299 cells exhibited significant decreases after treatment with cisplatin for 12 hours, indicating a decrease in oxphos (Figure 3.2C). However, the bound NADH fraction in both the nucleus and cytoplasm of H1299 cells expressing p53 did not change significantly with 12 hours of exposure to cisplatin. The high fraction of bound NADH in cisplatin-treated cells expressing p53 suggests that p53 regulates metabolism in the DNA damage response by maintaining a higher rate of oxphos than glycolysis relative to that in p53-null control cells.

3.4.4 The absence of REV3L increases p53-regulated oxphos following cisplatin treatment

Since REV3L appeared to affect basal p53-regulated metabolism, we investigated the metabolic response of H1299 cells in cisplatin-treated cells expressing p53 with REV3L depletion by shRNA. The significant positive percent change in the fraction of bound NADH after 24 hours of treatment by cisplatin from basal suggests an increase of p53-regulated metabolism in the absence of REV3L (Figure 3.3A). Depletion of REV3L or expression of p53 alone did not exhibit positive percent changes in the fraction of bound NADH with cisplatin treatment. Using the p53-R175H mutant with siRNA depletion of REV3L exhibited similar percent change increases with cisplatin (Figure 3.3B). The percent increase in the bound fraction of NADH was greatest for cells expressing p53 with REV3L depletion via siRNA following cisplatin-induced DNA damage. Depletion of REV3L or expression of p53 alone also exhibited significant positive percent changes in the fraction of bound NADH after 24 hours of exposure to cisplatin, but not as great as that with the combination of p53 expression and REV3L depletion. The FLIM results suggest that there is a significant enhancement of p53-regulated oxphos as a result of cisplatin treatment in the absence of REV3L.
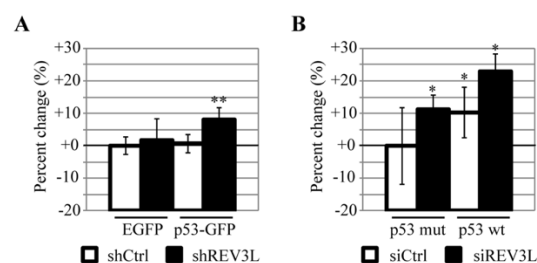
Figure 3.3. The absence of REV3L increases p53-regulated oxphos following cisplatin treatment. *(A) The percent change in the fraction of bound NADH after manipulation of p53 by transfection and REV3L by shRNA*

with 24 hours of 20µM cisplatin treatment. (B) The percent change in the fraction of bound NADH after transfection of p53-GFP with the R175H mutation and depletion of REV3L by siRNA with 24 hours of 20µM cisplatin treatment. * p<0.05, ** p<0.01, N>7.

3.4.5 Cancer cell sensitivity to cisplatin increases with p53 expression and REV3L depletion

Because cancer cells generally exhibit high rates of glycolysis, we aimed to determine whether or not the p53-enhanced oxphos when REV3L is depleted increased cancer cell sensitivity to cisplatin treatment. Cell survival was determined by morphology and a live/dead assay with Hoechst 33342 and propidium iodide (Figure 3.4A). The survival rate of H1299 cells at 24 hours with cisplatin treatment was determined by subtracting the number of cells uptaking propidium iodide from the initial number of cells and normalizing for the number of cells in the field of view (Figure 3.4B). Expression of p53 in the absence of REV3L exhibited a lower survival rate for H1299 cells relative to REV3L depletion or expression of p53 alone as well as the control showing that cancer cell sensitivity to cisplatin increases with p53 expression and REV3L depletion.

3.5 Discussion

The study herein suggests that the absence of REV3L can promote the p53-mediated upregulation of oxphos in H1299 lung carcinoma cells treated with cisplatin and increases cancer cell sensitivity to the cisplatin treatment. By measuring the fluorescence lifetime of NADH and calculating the fraction of protein-bound NADH throughout the cell, it was observed that cancer cells lacking REV3L but expressing functional p53 exhibit higher rates of oxidative phosphorylation than cells lacking REV3L or expressing p53 alone. Without REV3L, TLS and the subsequent repair of cisplatin-induced DNA lesions are greatly reduced

and DNA damage signaling can persist. Furthermore, p53 halts the cell cycle until repair is completed and mediates the upregulation of oxphos, thereby antagonizing the cancerous metabolic phenotype characterized by high rates of glycolysis. These cancer cells then exhibited increased sensitivity to cisplatin treatment relative to cells only lacking REV3L, only expressing wild type p53, and control cells. A model for the roles of REV3L and p53 in lung cancer sensitivity to cisplatin is proposed (Figure 3.4C). This presents a promising area for future development of treatment plans that can address lung cancer resistance to cisplatin.
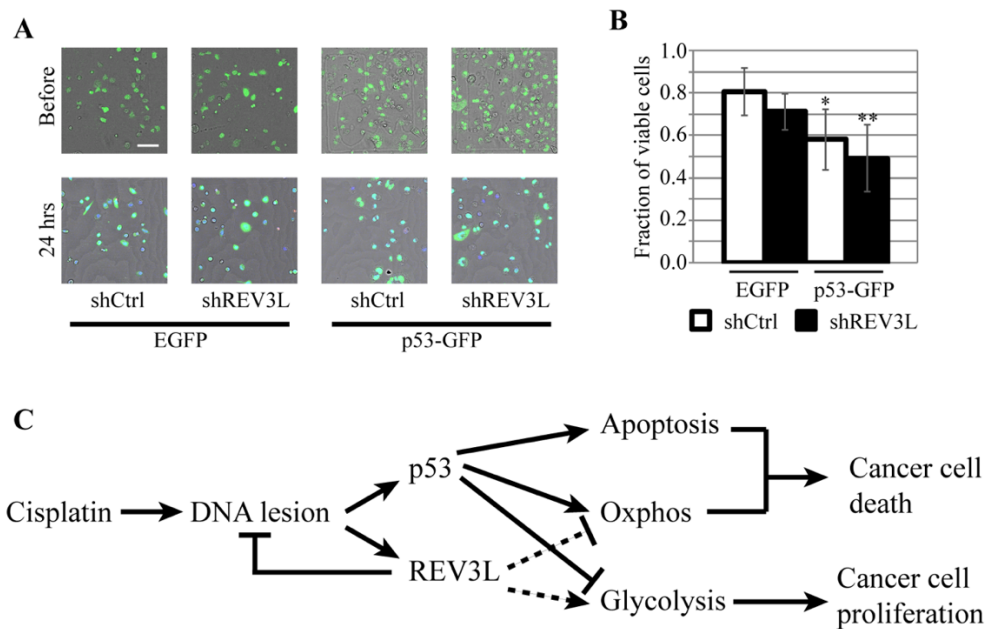
Figure 3.4. Cancer cell sensitivity to cisplatin increases with p53 expression and REV3L depletion. *(A) Brightfield images of cells after manipulation of p53 by transfection and REV3L by shRNA with 24 hours of 20μM cisplatin treatment. Scale bar = 10μm. (B) Bar graph of the cell survival rate of H1299 cells. (C) A proposed model for the role of REV3L and p53 in cancer cell sensitivity to cisplatin. * p<0.05, ** p<0.01.*

We observed an increased fraction of bound NADH in the absence of REV3L even without p53 activity. Other DNA damage signaling events, namely PARP activity, which consumes NAD+ and inhibits glycolysis, can cause an overall cellular increase of bound

NADH[24]. Thus, depleting REV3L in cells that lack functional p53 can still initiate the DDR leading to other signaling cascades that can suppress the cancerous metabolic phenotype and ultimately reduce cancer cell proliferation. While the observed survival rate following cisplatin treatment in H1299 cells lacking both REV3L and functional p53 was comparable to wild type H1299 cells, it is worth investigating treatments that target REV3L in order to reduce resistance to cisplatin.

In this study, p53-null H1299 lung carcinoma cells were used. The introduction of functional p53 into H1299 cancer cells confers the tumor suppressive properties of p53, including metabolic regulation, which were previously not present. In basal conditions, p53 promotes oxphos and inhibits glycolysis[70]. Thus, the higher bound NADH fraction as measured by FLIM in H1299 cells expressing p53 relative to control cells is consistent with previous research. The increased sensitivity to cisplatin treatment in cells expressing both functional p53 and REV3L could occur due to the initiation of multiple DNA repair pathways such as the REV3L-mediated TLS and the ATR signaling pathway[71]. ATR signaling to p53 can increase oxphos, therefore increasing the fraction of bound NADH. Restoring p53, then, in cancer cells lacking functional p53 or expressing mutated p53 presents a very promising option for co-treatment with cisplatin chemotherapy.

The metabolic regulatory functions of p53 have only been recently discovered within the past few decades while the role of REV3L in metabolism is still currently unclear. This study provides some insight into the role of REV3L in metabolism and its interaction with the tumor suppressor p53 in that REV3L appears necessary for p53-mediated upregulation of oxphos. The data show a previously unidentified connection between p53 and REV3L in regulating metabolism and require further research to better

understand the underlying interactions between them in this fight against

chemotherapeutic resistance.

3.6 Acknowledgements

CHAPTER 4

NAD Consumption by PARP1 in Response to DNA Damage Triggers Metabolic Shift Critical for Damaged Cell Survival

4.1 Abstract

DNA damage signaling is critical for the maintenance of genome integrity and cell fate decision. Poly(ADP-ribose) polymerase 1 (PARP1) is a DNA damage sensor rapidly activated in a damage dose and complexity-dependent manner playing a critical role in the initial chromatin organization and DNA repair pathway choice at damage sites. However, the cell-wide consequence of its activation in damaged cells is not well delineated. Using the phasor approach to fluorescence lifetime imaging microscopy (FLIM) and fluorescence-based biosensors in combination with laser microirradiation, we found a rapid cell-wide increase of the bound/free NADH ratio in response to nuclear DNA damage, which is triggered by NAD+/NADH depletion by PARP activation. This change is linked to the metabolic shift to oxidative phosphorylation (oxphos) over glycolysis. Inhibition of the respiratory chain resulted in rapid PARP-dependent ATP reduction and intracellular acidification, and eventually, PARP-dependent, AIF-independent apoptosis indicating that oxphos becomes critical for damaged cell survival. The results reveal the novel pro-survival effect of PARP activation through a change in cellular metabolism, and demonstrate how unique applications of advanced fluorescence imaging technologies in combination with laser microirradiation can be a powerful tool to interrogate damage-induced metabolic changes at high spatiotemporal resolution in a live cell.

4.2 Introduction

Poly(ADP-ribose) polymerase 1 (PARP1) functions as a DNA damage sensor whose enzymatic activity is rapidly activated in response to DNA damage[72]. PARP1 uses oxidized nicotinamide adenine dinucleotide (NAD+) as a substrate to ADP(ribosyl)ate itself and various target proteins. Although initially recognized as a base excision repair (BER) factor, it is now known that PARP1 is involved in multiple DNA repair pathways. Rapid poly(ADP-ribose) (PAR) accumulation at damage sites controls damage site accessibility through the recruitment of various chromatin modifiers and dictates DNA repair pathway choice[72-86]. Since PARP response is fast and was thought to be relatively short-lived, previous studies largely focused on immediate early effects of PARP at DNA damage sites[87]. For example, we demonstrated that PARylation at damage sites suppresses the 53BP1 recruitment to damage sites, providing another explanation for 53BP1- and NHEJ-dependent cytotoxicity by PARP inhibition[88].

In addition to promoting efficient repair and thus cell survival, PARP was also shown to affect metabolism and mediate senescence and cell death (both apoptosis and necrosis) when hyperactivated[72]. Since the oxidized and reduced forms of NAD (NAD+ and NADH, respectively) are metabolic cofactors critical for cellular energy production[89], consumption of NAD+ by damage-induced PARP activation was expected to hinder cellular energy metabolism. In addition, PARP1 inhibits glycolysis through PAR binding to hexokinase (HK), a critical enzyme in the pathway[24,90,91], resulting in ATP deprivation and subsequent cell death termed parthanatos[92]. Parthanatos also requires PAR-dependent nuclear translocation of apoptosis-inducing factor (AIF) from mitochondria[93]. PARP

activation was also shown to cause intracellular acidification, which appears to promote necrosis[94]. Thus, while the downstream effects of PARP activation may be complex, collectively, it was suggested to trigger cell death as the default result of PARP "hyperactivation". However, the precise relationship between the DNA damage dosage and the strength of PARP signaling that affects energy metabolism and/or triggers cell death is unclear, and whether or not damage-induced PARP activation has any cell-wide pro-survival effects distinct from its immediate role at DNA damage sites has not been determined.

Because NADH is an essential cofactor for oxidation-reduction (redox) reactions and production of ATP, multiphoton microscopy techniques to capture NADH autofluorescence and measure metabolic dynamics in living cells have recently garnered attention for their broad applicability in studies ranging from development to cancer and aging[95-97]. The free and protein-bound states of NADH were shown to reflect glycolysis and oxidative phosphorylation (oxphos), respectively, which can be differentiated using fluorescence lifetime imaging microscopy (FLIM). One of the major challenges of FLIM is the fitting routine required to dissect the possible lifetime contributions of different fluorescent species in a single pixel. In our approach, we apply the fit-free phasor approach to FLIM analysis that provides a graphical representation of the fluorescence decay at each pixel[46]. Pixels that have multiple contributions of fluorophore lifetimes can be resolved as a linear combination of the individual species. Furthermore, the absolute concentration of NADH can be measured using the phasor-FLIM method[98], which should sensitively respond to the changes of NAD+ and accurately reflect metabolic dynamics[99].

Using the phasor-FLIM approach in conjunction with fluorescent biosensors and laser microirradiation, we examined the real-time metabolic changes in response to DNA damage with high spatiotemporal resolution and interrogated the contribution of differential PARP signaling in response to different dosage/complexity of DNA damage. Using this comprehensive approach, we observed a rapid reduction of NADH (correlating with the decrease of NAD+) and ATP in both the nucleus and cytoplasm in a PARP1 activity-dependent manner. Interestingly, PARP1 activation also triggers a rapid increase of protein-bound NADH species over free NADH, which correlates with the net increase of oxphos over glycolysis. Importantly, this shift appears to reflect the increased metabolic dependence of damaged cells on oxphos. Inhibitors of oxphos highly sensitized cells to DNA damage with exacerbated ATP deprivation, resulting in AIF-independent apoptosis. This increased dependence on oxphos is rescued by PARP inhibition or NAD replenishment, and thus, is distinct from PARP-dependent HK inhibition in glycolysis. Taken together, the phasor approach to FLIM and fluorescence biosensors in combination with laser microirradiation provides valuable tools to capture high-resolution single cell dynamics of metabolic changes in response to DNA damage and uncovered the key downstream consequence of NAD consumption by PARP1 that promotes cell survival in DNA damage cells.

4.3 Materials and Methods

4.3.1 Cell culture

HeLa adenocarcinoma cells were cultured in DMEM (Invitrogen, Carlsbad, CA) supplemented with 10% fetal bovine serum (FBS), 2 mM L-glutamate, and 1% penicillin-streptomycin. HCT116 colorectal carcinoma cells were cultured in ATCC-formulated McCoy's 5a Medium Modified (ATCC 30-2007) supplemented with 10% FBS and 1% penicillin-streptomycin. HFF-1 human foreskin fibroblast cells were cultured in DMEM (ATCC 30-2002) supplemented with 15% FBS and 1% penicillin-streptomycin.

4.3.2 Inhibitor treatment

Cells were treated for 1 hr before experiments with PARP inhibitor (PARPi) (100 μM NU1025 (Sigma) or 20 μM olaparib (Sigma)), or ATM inhibitor (10 μM KU55933 (Calbiochem)) and DNA-PK inhibitor (10 μM NU7026 (Sigma)), in 0.1% DMSO (Sigma). For respiration inhibition, cells were treated for 1 hr before experiments with the mitochondrial complex I inhibitor rotenone (Sigma, R8875) (1 μM for laser damage and 0.25 μM for MMS or H_2O_2-induced damage) and complex III inhibitor antimycin A (Sigma, A8672) (1 μM for laser damage and 0.25 μM for MMS or H_2O_2-induced damage) in 0.2% DMSO. For nicotinamide (NAM) treatment, cells were treated 1 hr before laser-induced DNA damage induction with 1 mM NAM (Sigma, 72340). For NAMPT inhibition, cells were treated with 10 nM FK866 (Sigma, F8557) for 6 hr before experiments.

4.3.3 MMS and H_2O_2 treatment

For comparison to the effects of laser-induced DNA damage, cells were treated with 1 mM or 3 mM methyl methanesulfonate (MMS) for 1 hr or 500 μM hydrogen peroxide (H_2O_2) for 30 min prior to metabolic and cytotoxic analyses.

4.3.4 Immunofluorescent staining

Immunofluorescent staining (IFA) was performed essentially as described previously (34). Antibodies used are mouse monoclonal antibodies specific for γH2AX (05–636, Millipore), PAR polymers (BML-SA216–0100, Enzo Life Sciences, Inc.), Mre11 (GTX70212, Gene Tex, Inc.), Actin (Sigma) or cyclobutane pyrimidine dimer (CPD) (MC-062, Kamiya Biomedical Company) as well as rabbit polyclonal antibodies specific for AIF antibody (GTX113306, Gene Tex, Inc.). Affinity-purified rabbit anti-PARP1 antibody was previously described[88,100].

4.3.5 Confocal fluorescence microscope

All experiments were performed on an inverted confocal Zeiss LSM710 (Carl Zeiss, Jena, Germany). A 40x 1.2NA water-immersion objective (Zeiss, Korr C-Apochromat) was used. AlexaFluor 488 and GFP were excited using an argon ion laser with a 488 nm line and fluorescence was detected from 490 to 555 nm. Cy3 and mCherry were excited using a 561 nm DPSS laser and fluorescence was detected from 580 to 650 nm.

4.3.6 NIR laser microirradiation

A pulsed titanium-sapphire 100 femtosecond laser (Spectra-Physics, Santa Clara, CA) at 80 MHz tuned for 780 nm two-photon microirradiation was used at the input power of 17.7 mW, 19.9 mW, and 24.6 mW measured after the objective for low, medium, and high damage conditions, respectively. Image sizes of 512x512 pixels were obtained with

defined regions of 45x5 pixels for microirradiation. Microirradiated regions were scanned once with a scan speed of 12.61 µs per pixel for damage induction.

4.3.7 Phasor approach to FLIM and NADH intensity/concentration measurement

Following DNA damage induction, either by laser microirradiation or chemical agents (MMS or H_2O_2), 40 frames of FLIM data were acquired with 740 nm two-photon excitation at approximately 2 mW by an ISS A320 FastFLIM box (ISS, Champaign, IL) with image sizes of 256x256 pixels and a scan speed of 25.21 µs per pixel. Fluorescence excitation signal was separated with a dichroic filter (690 nm) and fluorescence was detected by photomultiplier tubes (H7422P-40, Hamamatsu, Japan) with a blue emission filter (495LP) of 420-500 nm to capture NADH auto-fluorescence. FLIM data was transformed into pixels on the phasor plot using the SimFCS software developed at the Laboratory for Fluorescence Dynamics, University of California, Irvine as described previously[46]. Coumarin-6, which has a known single exponential lifetime of 2.5 ns, was used as a reference for the instrument response time. Nuclear and cytoplasmic compartments were analyzed separately based on the intensity of NADH signal as previously reported[47]. The concentration of NADH was calculated by calibrating with a known concentration of free NADH and correcting for the difference in quantum yield between the free and bound forms of NADH as described previously[98].

4.3.8 NAD+ measurement

The HeLa cell lines stably expressing either the cytoplasm- or mitochondria-targeted NAD+ sensor, or the corresponding cpVenus controls were kindly provided by Dr.

Xiaolu Cambronne (the Oregon Health and Science University)[101]. Cells were plated on a

glass-bottomed imaging dish and were incubated at 37°C for ~40 hr until they reached 60-

80 % confluency. Live images were captured before and 1 hr after indicated treatment. The

fluorescence ratios (488 nm/405 nm) were measured and analyzed as previously

described[101].

4.3.9 ATP measurement

HeLa cells were transfected using Lipofectamine 3000 (Invitrogen) with either

AT1.03 (cytoplasm-localized) or Nuc AT1.03 (nucleus-localized) plasmids[102]. After 18-24

hr, cells were subjected to laser microirradiation or MMS treatment in the presence of

DMSO or indicated inhibitors, and the YFP/CFP fluorescence ratios were measured as

previously described[103]. Experiments are replicated at least three times and 20-30 cells

were examined in total.

4.3.10 Intracellular pH (pHi) measurement

Changes in intracellular pH were measured using the commercial pHrodo Green AM

Intracellular pH Indicator kit (ThermoFisher, P35373) according to manufacturer's

instructions.

4.3.11 Measurement of mitochondria respiration: the Seahorse assay

HeLa cells were plated in a 24-well Seahorse XF-24 assay plate at 1 X 10^5 cells/well

and grown for approximately 20 hr. Cells were then incubated with 3 mM MMS for 1 hr in

the presence of DMSO or PARP inhibitor. At 1 hr after the release from MMS treatment,

Seahorse analysis was performed using an Agilent Seahorse XF24 Extracellular Flux Analyzer following the manufacturer's protocol as described previously[104].

4.3.12 Detection of senescence, apoptosis and necrosis and assessment of cytotoxicity

Cellular senescence was determined by β-galactose staining as described previously[105]. Apoptosis and necrosis were detected using the commercial kit (AB176749, Abcam, Cambridge, England) following manufacturer's instruction. Cytotoxicity was also examined by propidium iodide permeability assay. After damage induction and inhibitors treatment, propidium iodide and Hoechst 33342 were added into the medium to achieve final concentrations of 0.8 μg/mL and 0.5 μg/mL, respectively. The cells were then incubated at 37 °C for 5-15 min and visualized for the total cells (blue) and dead cells (red) under a confocal fluorescence microscope.

4.4 Results

4.4.1 Phasor-approach to FLIM reveals a ratiometric increase of protein-bound NADH over free NADH in response to DNA damage

Using laser microirradiation, DNA damage-induced changes of the free and bound fractions of NADH were measured by FLIM in the cytoplasm and nucleus in HeLa cells. Laser microirradiation can be used to induce DNA damage in a highly controlled fashion[40,88,106-108]. In particular, titration of the input power of near-infrared (NIR) laser allows differential DNA damage induction, from relatively simple strand breaks to complex DNA damage (i.e. single and double strand breaks (SSBs and DSBs), thymine dimer and

base damage) with differential H2AX phosphorylation (γH2AX) and PARP activation (Appendix B.1A; Figure 4.2A)[88,107]. With high input-power, over 70% of irradiated cells were viable after 24 hr and surviving cells were arrested in interphase with no evidence for senescence at least up to 60 hr post irradiation (Appendix B.1B and C). Over 90% of cells were viable at 24 hr after microirradiation with medium input power whereas cells actually recovered and proliferated with low input-power irradiation (Appendix B.1B).

Using these varying laser input powers, we examined the effect of nuclear DNA damage on cellular metabolism in real time. Clusters of pixels were detected on the phasor plot and used to pseudo-color the intensity images according to fluorescence lifetime (Figure 4.1A and B). We also measured both NADH intensity and concentration [98], which are largely concordant with each other and are reduced in a damage dose-dependent manner (Appendix B.2A). This is in agreement with the reduction of NAD+ in the mitochondria and cytoplasm as detected by the NAD+-specific biosensor[101] (Appendix B.2C). FLIM analyses revealed the increase in the ratio of the bound NADH fraction over total NADH within the first 120 min post damage induction in both the cytoplasm and nucleus (Figure 4.1C and E). Interestingly, while this increase was transient for low and medium damage conditions, the fraction of bound NADH remained high for over 12 hr with high input power damage, which is particularly prominent in the nucleus, despite the recovery of NADH intensity/concentration (Figure 4.1C and 4.2B; Appendix B.2A). The results raise the possibility that the shift to bound NADH is not the mere reflection of NADH depletion but represents more long-term metabolic reprogramming in response to damage. Treatment with alkylating (MMS) and oxidizing (H_2O_2) damaging agents exhibited similar transient shifts toward a high fraction of bound NADH (Figure 4.1D and E). Comparable

kinetics of NADH intensity/concentration reduction consistent with NAD+ reduction[101] was also observed (Appendix B.2B and C). Taken together, the results demonstrate that the increase of bound NADH is a general response to DNA damage, not restricted to laser damage.
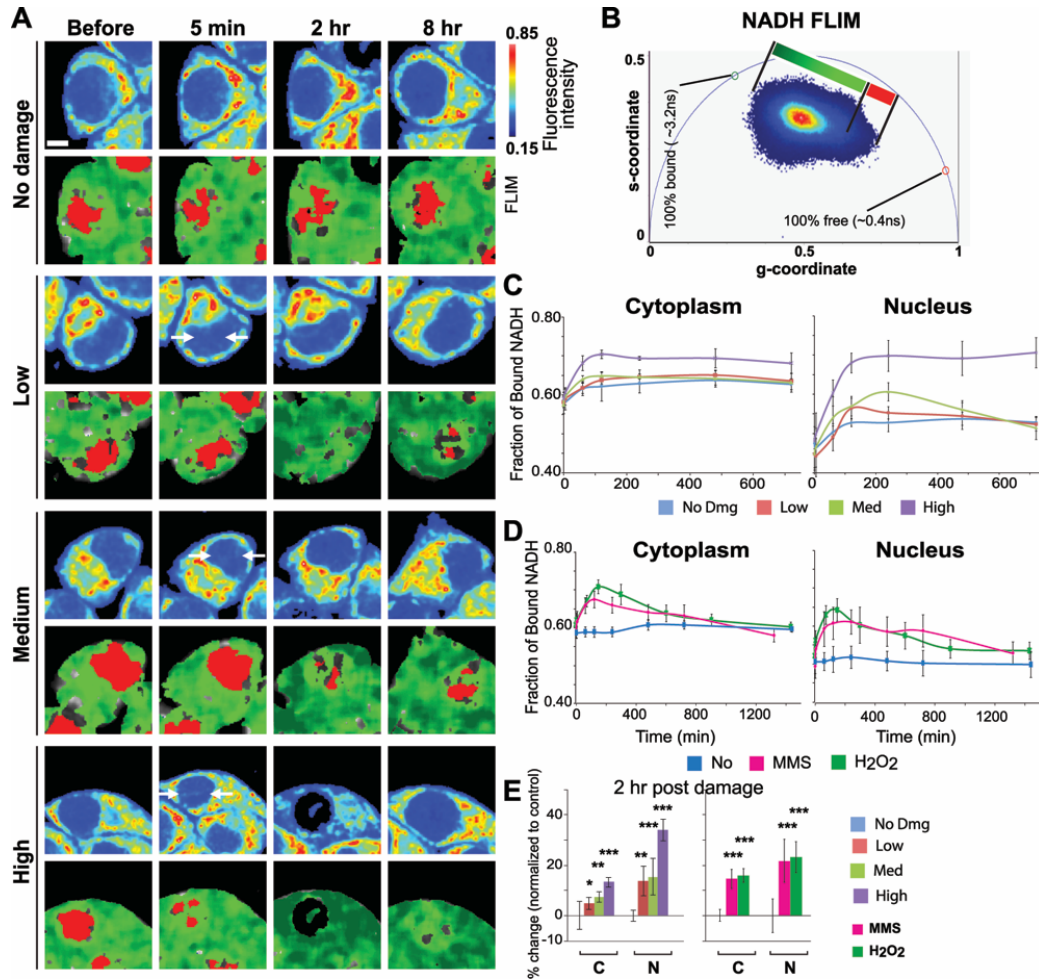
Figure 4.1. DNA damage induces rapid shift from free to bound NADH. *(A) Intensity (top) and pseudo-colored FLIM (bottom) images of undamaged HeLa cells and HeLa cells damaged at low, medium, and high input laser power. In intensity images, the line color from blue to red corresponds to the normalized intensity. Damage sites are indicated by white arrows. The FLIM images are pseudo-colored according to the clusters selected on the phasor plot in (B). Scale bar = 5 μm. (B) Phasor histogram of fluorescence lifetimes on the phasor plot. Each pixel from the intensity image is transformed and plotted on the phasor diagram. Pixels are pseudo-colored based on the position along the line generated by the linear combination of short lifetime free NADH and longer lifetime protein-bound NADH. (C) The fraction of bound NADH in the cytoplasmic and nuclear compartments calculated from the position of the phasor in (B) and plotted over time. (D) The fraction of bound NADH over time in the cytoplasmic and nuclear compartments of HeLa cells treated with either 1 mM methyl methanesulfonate (MMS) or 500 μM hydrogen peroxide (H_2O_2). (E) The percent change in the fraction of bound NADH at 2 hr post damage relative to basal conditions. * $p < 0.05$, ** $p < 0.01$, *** $p < 0.001$.*

4.4.2 Increase of the bound NADH fraction is entirely dependent on PARP1 activity

What regulates the damage-induced increase of bound NADH fraction? Two major damage signaling pathways are the PARP and PIKK pathways, which are both activated in a damage dose/complexity-dependent manner[88]. ATM is a member of the PIKK family, specifically activated by DNA damage to govern cell cycle checkpoint as well as DNA repair through target protein phosphorylation[109]. ATM and another PIKK member DNA-PK, which mediates non-homologous end joining of DSBs, are both involved in the spreading of nuclear-wide γH2AX in response to high-dose complex DNA damage[88,110]. Accordingly, PAR and γH2AX were induced initially at damage sites and spread to the whole nucleus in a damage dose-dependent manner (Figure 4.2A). Thus, we examined the effect of inhibition of PARP or ATM/DNA-PK on the increase of the bound NADH fraction (Figure 4.2 and Appendix B.3). As expected, inhibition of PARP by olaparib (PARPi) blocked the transient decrease of NADH intensity in both cytoplasm and nucleus, suggesting that the decrease of NADH in response to damage reflects deprivation of NAD+ by PARP, and confirmed that PARP activation originating in the nucleus affects NAD+/NADH concentration in the whole cell (Figure 4.2B and C). Importantly, PARPi also dramatically suppressed the damage-induced increase of the bound NADH fraction (Figure 4.2B and C). Similar results were obtained with another PARP inhibitor NU1025 (data not shown). Furthermore, comparable results were obtained with depletion of PARP1 by siRNA, indicating that PARP1, among the multiple PARP family members, is primarily responsible for the observed NADH dynamics (Figure 4.2D). In contrast, ATM and DNA-PK inhibitors (AiDi) have no significant effects on either bound NADH fraction or NADH intensity (Figure 4.2B

and C). Taken together, the results indicate that the change in the NADH state is dependent on PARP1 activity and not ATM or DNA-PK signaling.
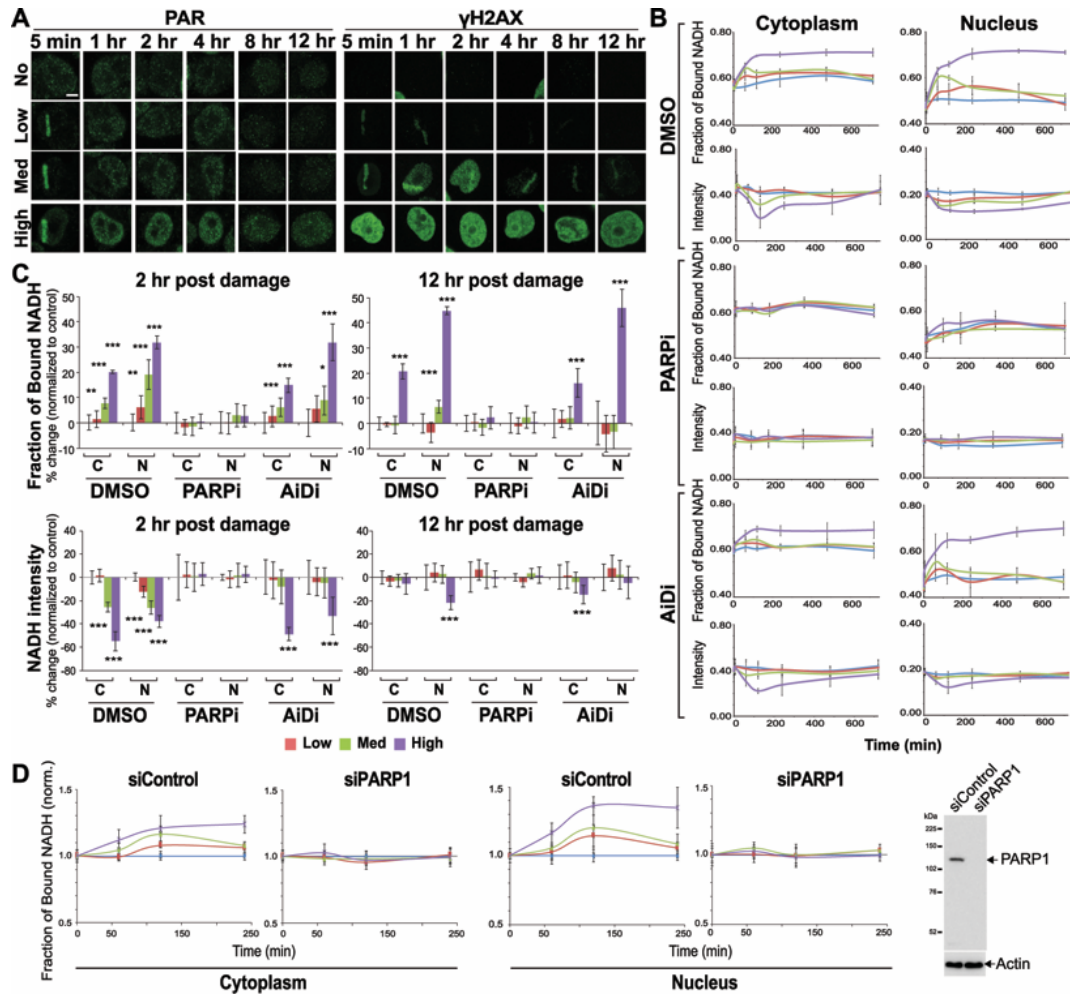
Figure 4.2. Damage-induced increase of the bound to free NADH ratio is PARP1-dependent.
(A) Immuno-fluorescent staining for PAR (left) and γH2AX (right) in HeLa cells fixed at various time points up to 12 hr post damage following low, medium, and high input laser power. Scale bar = 5 μm.
(B) The fraction of bound NADH and intensity of NADH over time in the cytoplasmic and nuclear compartments of HeLa cells treated with either 0.1% DMSO (top), 20 μM PARP inhibitor (olaparib) (middle), or 10 μM ATM inhibitor (KU55933) and 10 μM DNA-PK inhibitor (NU7026) (bottom).
*(C) The percent change in the fraction of bound NADH (top) and the intensity of NADH (bottom) at 2 hr (left) and 12 hr (right) post damage relative to basal conditions. * p < 0.05, ** p < 0.01, *** p < 0.001.*
(D) The fraction of bound NADH over time in the cytoplasmic (left) and nuclear (middle) compartments of HeLa cells with siPARP1 or control siRNA. Western blot analysis (right) of siControl and siPARP1 transfected HeLa cells. The whole cell extracts were run on SDS-PAGE and blotted with anti-PARP1 antibody. Anti-actin antibody served as loading control.

4.4.3 Increase of bound NADH in the cytoplasm and nucleus is sensitive to mitochondrial respiratory chain complex inhibitors and rescued by NAM

The increase in protein-bound NADH in the cell is thought to reflect the oxphos pathway of energy metabolism whereas the increase in free NADH reflects the glycolytic pathway[49]. Since we observed an increase of protein-bound NADH in response to damage (Figure 4.1), we used the mitochondrial complex I and III respiratory chain inhibitors (rotenone and antimycin A, respectively) (R+A) that inhibit oxphos to examine the effect on the damage-induced increase of bound NADH species. We found that these inhibitors increased the overall basal NADH level (both intensity and concentration), which muted the response to DNA damage (Figure 4.3A; data not shown). The inhibitor treatment further suppressed the damage-induced long-term increase of the protein-bound NADH fraction (observed up to 12 hr post damage) (Figure 4.3A). Interestingly, the initial increase of the bound species at 1-2 hr post damage was not inhibited despite the fact that there was no significant change of NADH intensity (Figure 4.3A). This suggests that the initial increase and subsequent maintenance of the high bound/free NADH ratio may be mediated by two different mechanisms.
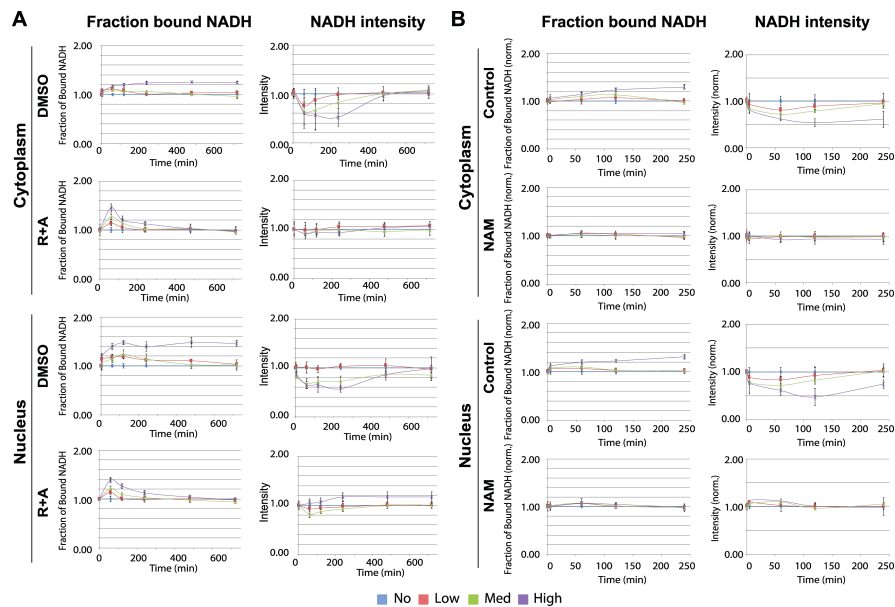
Figure 4.3. Increase of the bound NADH fraction is suppressed by the respiratory chain inhibitors

(A) The fraction of bound NADH (left) and intensity of NADH (right) in the cytoplasmic (top) and nuclear (bottom) compartments plotted over time in cells damaged with low, medium, and high input laser power in the presence of control (0.1% DMSO) or 1 μM rotenone and 1 μM antimycin A (R+A) as indicated.
(B) The change in the fraction of bound NADH (left) and intensity of NADH (right) over time in cells damaged with low, medium, and high input laser power in control cells and cells pre-treated for 1 hr with 1 mM nicotinamide (NAM).

Our analysis revealed that the increase of the bound NADH fraction occurs in both the nucleus and cytoplasm (containing mitochondria) in a highly synchronous fashion, and comparable suppression by PARP and respiratory inhibitors was observed in both subcellular regions, indicating the close communication between the two compartments (Figure 4.1, 4.2B and 4.3A). The observed effect of PARP inhibition can be due to suppression of target protein PARylation and/or blocking the intracellular NAD substrate deprivation. To test the latter hypothesis, we examined whether supplementing NAD+ would reverse the effect. Indeed, NAM, a precursor of NAD+ in the salvage pathway, not only inhibited the decrease of NADH but also suppressed the shift to bound NADH fraction both in the nucleus and cytoplasm (Figure 4.3B). The increase of bound NADH was completely suppressed during the first 4 hr unlike with R+A treatment (Figure 4.3A), but comparable to PARPi (Figure 4.2B). The results demonstrate that NAD+ consumption by PARP is the trigger to induce the observed shift to bound NADH.

The observed reduction of bound NADH by the respiratory chain inhibitors is concordant with the predicted inhibition of oxphos, strongly suggesting that damage-induced changes of NADH state reflect the change in energy metabolism. To further assess the relationship between the free-to-bound NADH shift and energy metabolism, metabolic flux analysis by the Seahorse XF Analyzer was performed in control and MMS-treated cells. The FLIM analyses indicate that the respiratory inhibitors have similar effects on MMS-treated cells (Figure 4.3A and 4.4A). Namely, the partial increase of the basal NADH level

and partial inhibition of the damage-induced shift from free to bound NADH in both the

cytoplasm and nucleus. Under this damaging condition, both oxphos as measured by the

oxygen consumption rate (OCR) and glycolysis by the extracellular acidification rate

(ECAR) were reduced compared to the undamaged cells, with suppression of ECAR much

more severe (Figure 4.4B). While PARPi has no significant effect on both basal OCR and

ECAR in damaged cells, damage-induced inhibition of peak OCR and ECAR are strongly

alleviated by PARPi. Cellular reliance on oxidative metabolism (OCR/ECAR) was also

calculated. The results indicate the significantly elevated maximum, but not basal,

oxidative reliance in MMS-treated cells compared to the control undamaged cells, which is

suppressed by PARPi (Figure 4.4C). Taken together, these results demonstrate that

complex DNA damage that induces robust PARP activation triggers a metabolic shift

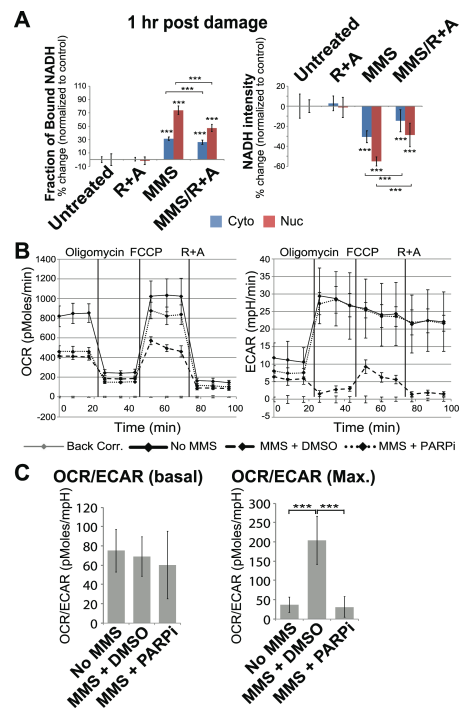resulting in greater reliance on oxphos over glycolysis.

Figure 4.4. Seahorse analysis of MMS-treated cells reveal PARP-dependent increase of oxphos over glycolysis. *(A) The percent change in the fraction of bound NADH (left) and intensity of NADH (right) in the*

*cytoplasmic and nuclear compartments calculated from the position of the phasor in (Figure 4.1B) and plotted over time in control undamaged cells or cells damaged with 3 mM MMS and with or without 1 μM rotenone and 1 μM antimycin A (R+A). *** p < 0.001. (B) The oxygen consumption rate (OCR, left) and extracellular acidification rate (ECAR, right) for untreated cells or cells treated with 3 mM MMS and 0.1% DMSO or 20 μM PARP inhibitor (olaparib) as analyzed by the Agilent Seahorse XF Analyzer. (C) The ratio of OCR to ECAR (oxidative reliance) evaluated at basal conditions (left) or at maximum metabolic capacities calculated following FCCP for OCR and following oligomycin for ECAR (right). *** p < 0.001.*

4.4.4 Oxidative phosphorylation is critical for damaged cell survival

The above results indicate that damaged cells undergo metabolic reprogramming: DNA damage increases cellular reliance on oxidative phosphorylation. Thus, we examined cellular damage sensitivity to the respiratory chain inhibitors (R+A). While the R+A treatment had no significant effect on undamaged cells, cells treated with MMS or H_2O_2 became significantly more sensitive to the inhibitors (Figure 4.5A). This increased cytotoxicity was alleviated by PARP inhibition or PARP1 depletion, indicating that the cytotoxic effect of oxphos inhibition is PARP-mediated (Figure 4.5A, B, and C). Furthermore, the increased damage sensitivity by oxphos inhibition can also be rescued by the addition of NAM (Figure 4.5B). The NAM rescue effect is blocked by the inhibitor of nicotinamide phosphoribosyltransferase (NAMPT), the rate-limiting enzyme for NAD+ synthesis from NAM in the salvage pathway, suggesting that the NAM conversion to NAD is required for the rescue effect (Figure 4.5B and D). As expected, NAMPT inhibitor does not block the rescue effect of PARPi (Figure 4.5D). Similar results were obtained with laser damage (Figure 4.5E and F). Following high input-power laser damage, the survival rate of control cells at 8 hr after damage induction is approximately 83% in control cells compared to 18% in cells treated with R+A (Figure 4.5E and F). This increased damage sensitivity is PARP-dependent and can be suppressed by NAM (Figure 4.5E and F). Damage sensitivity

was also suppressed by adding NAM even at 1 hr post laser damage induction (data not shown).
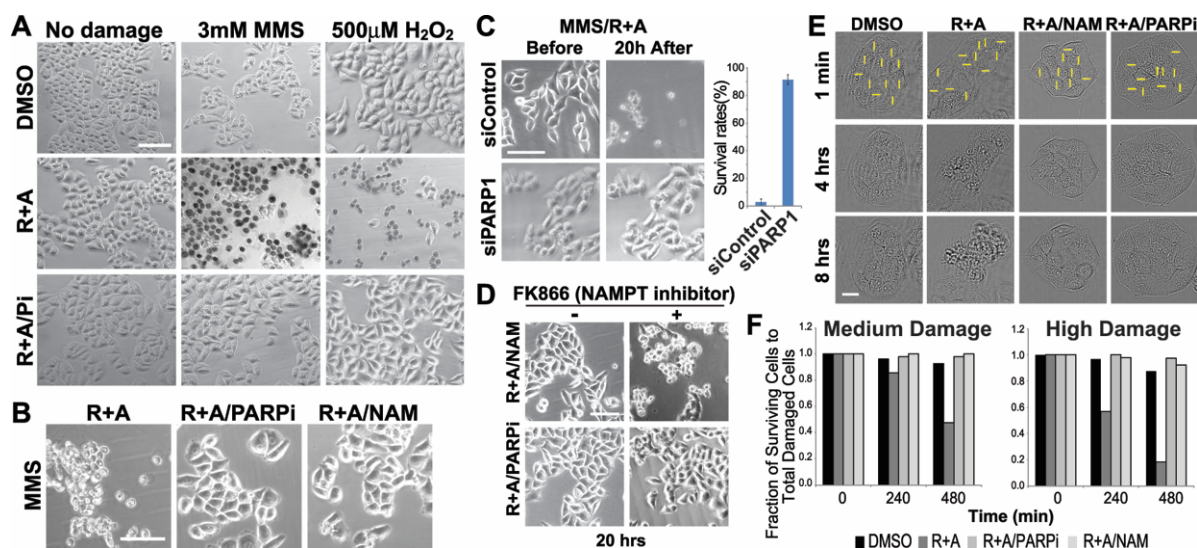
Figure 4.5. Oxphos inhibition results in increased DNA damage sensitivity, which is alleviated by PARP inhibition or NAM. *(A) Cells were either undamaged or treated with MMS or H_2O_2 and released from damage for 20 hr in the presence of DMSO only, R+A, or R+A with PARP inhibitor (Pi). In DMSO-treated cells, no significant cytotoxicity is observed while R+A treatment resulted in significant cell death (as detected by trypan blue) only in MMS- and H_2O_2-treated cells. This cytotoxicity is suppressed by PARP inhibitor treatment. Scale bar = 100 µm. (B) Cytotoxic effect of R+A on MMS-treated cells (left) as in (A) is alleviated by PARPi (middle) or NAM (right). Scale bar = 100 µm. (C) The effect of control siRNA or PARP1-specific siRNA treatment in cells treated with MMS and R+A. Depletion of PARP1 (as shown in western blot in Figure 4.2D) was sufficient to promote cell survival in MMS/R+A-treated cells. N=200. Scale bar = 100 µm. (D) NAM effect is NAMPT-dependent. In the presence of NAMPT inhibitor, addition of NAM failed to suppress the cytotoxicity in MMS/R+A-treated cells. PARPi-treated cells are shown for comparison. Scale bar = 100 µm. (E) Cytotoxic effect of R+A treatment in laser damage cells was suppressed by NAM or PARPi treatment. Scale bar = 20 µm. (F) Cell survival at 4 and 8 hr after laser damage induction in cells treated with DMSO, R+A, R+A with PARPi, R+A with NAM. N>50.*

Staining for PAR revealed that the amount of NAM used (1 mM) is not sufficient to inhibit PARylation, further confirming that the rescue effect of NAM is not due to PARP inhibition (Appendix B.4A). Cell death caused by respiratory inhibition of damaged cells was found to be apoptosis and not necrosis, but is distinct from parthanatos as no AIF relocalization to the nucleus was observed (Appendix B.4B and C). Taken together, the results indicate that the oxphos pathway becomes critical for cell survival in damaged cells specifically to antagonize NAD+ depletion by PARP activation.
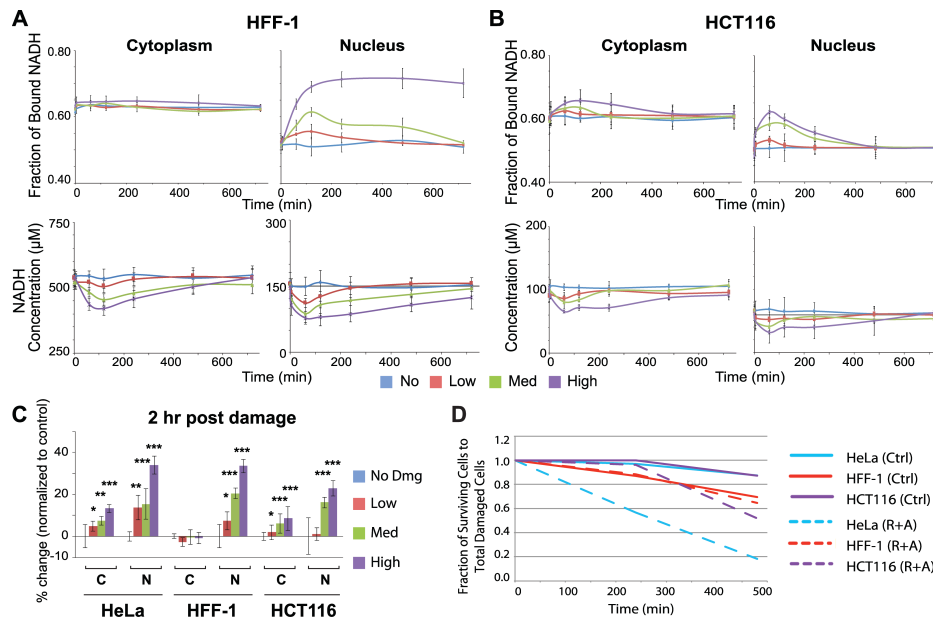
Figure 4.6. Differential free to bound NADH shift in different cell types. *(A) The fraction of bound NADH in the cytoplasmic and nuclear compartments in primary HFF-1 cells following laser damage induction. Corresponding NADH concentration measurement is shown underneath. (B) The same experiments in HCT116 cells. (C) The percent change in the fraction of bound NADH in HeLa, HFF-1, and HCT116 cells at 2 hr post damage relative to basal conditions. * p < 0.05, ** p < 0.01, *** p < 0.001. (D) Differential sensitivity of HeLa, HFF-1, and HCT116 to oxphos inhibition in damaged cells. N>50.*

The observed metabolic shift in response to DNA damage is not a HeLa cell-specific phenomenon (Figure 4.6). Interestingly, however, while transient NADH decrease follows similar kinetics, the extent and duration of the metabolic shift is significantly different in different cell types despite with the same damage conditions (Figure 4.6A, B and C). No significant shift was observed in the cytoplasm of human foreskin fibroblasts (HFF-1) cells while a prominent and persistent shift was observed in the nucleus, especially with high input-power damage (Figure 4.6A). The shift in the HCT116 colorectal carcinoma cell line, in contrast, was transient (restored in less than 8 hr) and no persistent switch was observed in the nucleus even with a high input-power damage unlike HeLa or HFF-1 cells (Figure 4.6B and C). HFF-1 cells are primary cells with high oxphos in contrast to highly glycolytic HCT116 cells[111,112]. Furthermore, we observed that HFF-1 cells under our

growth condition have significantly high basal NADH level (the basal NADH concentration is approximately five times higher in HFF-1 cells than in HCT116 cells in both the cytoplasm and nucleus) (Figure 4.6A). Thus, the observed differences may reflect the differences in basal metabolic states and basal NADH concentration possibly influencing damage-induced metabolic response. Consequently, these cells exhibited different damage-induced sensitivity to respiratory inhibition (Figure 4.6D). Following high input power damage, the survival rate of HCT116 cells treated with the inhibitors was approximately 51% in contrast to 87% without treatment. HFF-1 cells failed to show any increase in sensitivity to respiratory inhibition. It is possible that the amount of inhibitor used might not have been sufficient when the cells are already in the high basal oxphos state. The results reveal differential damage-induced sensitivity to oxphos inhibition in different cells, which may be dictated by the differences of basal metabolic states.

4.4.5 NAM rescues damage-induced PARP-dependent ATP depletion, but not intracellular acidification, in oxphos-inhibited cells

The above results demonstrated that damaged cells are sensitized to oxphos inhibition and either PARP1 inhibition or addition of NAM (and NAD+ generated through the salvage pathway) can rescue them. To address the mechanism, we determined ATP dynamics. DNA damage signaling and repair processes were expected to increase ATP consumption, thus reducing the intracellular ATP level. ATP would also be consumed by PARP during the PARylation reaction and was thought to be depleted as a result of PARP-mediated inhibition of glycolysis through HK leading to cell death[24,91]. Using the FRET-based ATP sensors that are specifically targeted to the cytoplasm and nucleus[103], we

observed the rapid reduction of ATP in the first 20 min, which persists over 6 hr post laser damage induction (Figure 4.7A). ATM and DNA-PK inhibitors had a subtle effect on the initial ATP decrease within the first 20 min in both the nucleus and cytoplasm and partially reduced ATP consumption up to 6 hr in the nucleus, but not in the cytoplasm (Figure 4.7A). This nuclear effect may reflect ATP consumption by DNA damage signaling and repair. In contrast, PARP inhibition completely suppressed ATP consumption in the cytoplasm and had a partial but major effect in the nucleus. The results indicate that ATP concentration in the whole cell is affected by the damage inflicted in the nucleus, and that the cytoplasmic ATP level is dictated by PARP activity.
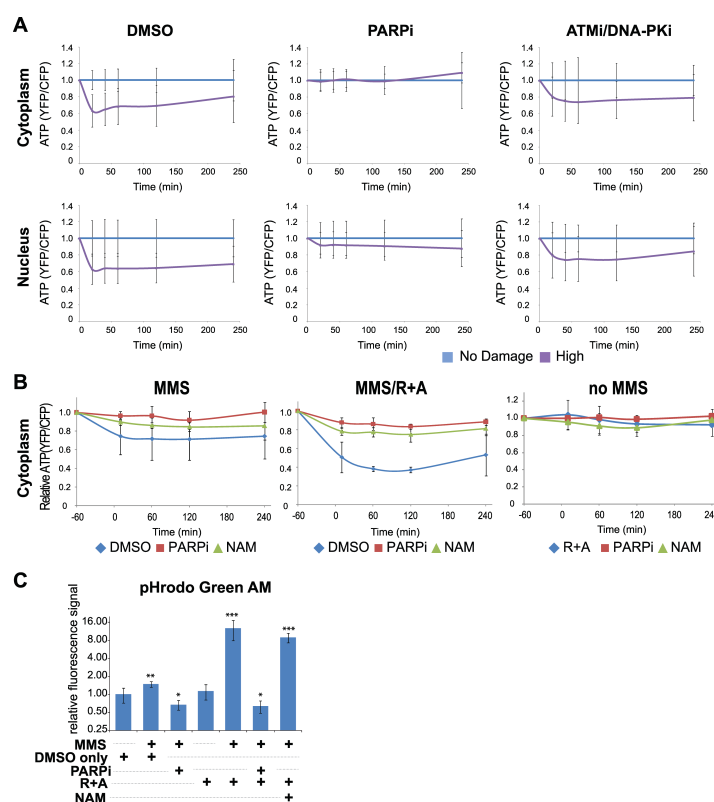
Figure 4.7. Analysis of cellular ATP and intracellular pH dynamics following DNA damage induction using ATP and pH biosensors. (A) Monitoring of relative ATP levels of HeLa cells expressing cytoplasmic (top) or nuclear (bottom) localized ATeam FRET biosensor. Cells were treated with either 0.1% DMSO (left), 20 μM PARP inhibitor (olaparib) (middle), or 10 μM ATM inhibitor (KU55933) and 10 μM DNA-PK inhibitor (NU7026) (right). Average YFP/CFP intensity was normalized with undamaged control cells at each time point. N>30. (B) Monitoring of relative cytoplasmic ATP levels of HeLa cells. Cells expressing cytoplasmic ATP sensor were cultured with medium containing with DMSO, PARPi or NAM at 1 hr before damage induction. 3 mM MMS was

added at time -60 min and removed at 0 min. Averaged YFP/CFP ratio of cells was normalized with undamaged DMSO control cells at each time point. N>10. (C) HeLa cells were treated with indicated chemicals with or without MMS damage induction for 1 hr. After 2 hr, pHrodo Green AM was then added for 30 min and fluorescence intensities were measured by confocal microscopy. Data are shown as relative fluorescence intensities where higher intensities correspond to lower pH. N>25. The pHi changes were compared to cells treated with DMSO only. * p < 0.01, ** p < 0.001, *** p < 0.000001.

We next tested the effect of oxphos inhibition on the cytoplasmic ATP level in MMS-treated cells, and how PARP inhibition or addition of NAM modulates this to see if ATP deprivation can explain the oxphos inhibition-induced cytotoxicity (Figure 4.7B). In undamaged cells, neither respiratory inhibition (R+A), PARPi, nor addition of NAM had any effect on the ATP level (Figure 4.7B, right "no MMS"). Cytoplasmic ATP is decreased in MMS-treated cells, which is reversed by PARPi or NAM (Figure 4.7B, left "MMS"). Notably, the combination of respiratory inhibition and MMS treatment resulted in a significant decrease of ATP, which was also effectively alleviated by PARPi and NAM (Figure 4.7B, middle "MMS/R+A"). The results reveal the damage-specific role of oxphos in ATP replenishment and confirmed that PARP activation is the major cause of cytoplasmic ATP reduction in damaged cells (Figure 4.7B). The fact that addition of NAM was sufficient to also restore the ATP level strongly suggests that NAD+ is central to the maintenance of intracellular ATP in damaged cells (Figure 4.7B). This is in contrast to the previous notion that PAR-dependent HK inhibition in the glycolytic pathway would result in ATP deprivation and cell death[24,90,91].

PARP was also shown to promote intracellular acidification, which was thought to promote cell death[94]. This may possibly be due to proton production during the PARylation reaction. Thus, we also monitored intracellular pH (pHi) using the pHrodo indicator (see section 4.3.10). Although we observed a slight, but significant change in pH by MMS treatment only, we found that oxphos inhibition led to very significant acidification

(Figure 4.7C; Appendix B.5). As expected, PARP inhibition reversed this phenomenon. Interestingly, however, NAM treatment had no significant effect on pHi, indicating that the NAM rescue effect on damage-induced sensitivity to oxphos inhibition is not due to the correction of acidic pHi, separating the two PARP-induced effects (Figure 4.7C; Appendix B.5).

4.5 Discussion

In the current study, we establish that phasor-FLIM can be used effectively to investigate real-time NADH dynamics in response to DNA damage with high spatiotemporal resolution in different subcellular compartments. Our results strongly support that the increase of the protein-bound NADH fraction in response to damage can serve as an indicator for the metabolic shift to oxphos. When combined with laser microirradiation that can focus precisely inside the nucleus, the metabolic effect of nuclear damage can be specifically analyzed as opposed to the conventional damaging methods (i.e. treatment with chemical agents or whole cell irradiation) that may directly damage, and therefore affect the function of, mitochondria. Furthermore, by regulating the laser input power, it is possible to examine the damage complexity/dosage effects on cellular metabolism. Together with using ATP and pH sensors, our results demonstrate complex metabolic consequences of damage-induced PARP1 activation in real time and uncover the crucial role of oxphos as a pro-survival effector of PARP1 signaling.

4.5.1 NADH intensity/concentration and NAD+

The ratio of the photons emitted by the free and protein-bound states of NADH to total photons absorbed, known as the quantum yield, depends on the binding substrate. While the free form of NADH has a relatively low quantum yield, the protein-bound forms of NADH have a much greater quantum yield due to a decreased probability of non-radiative decay of an excited molecule while the radiative emitting pathway is largely unaffected[113,114]. Thus, it is possible that typical calibrating procedures comparing intensities of known concentrations of the fluorophore to those measured in the cell may overestimate the bound NADH species. Thus, it is important to calculate and compare the absolute concentration of NADH species. We confirmed that in response to DNA damage, the changes of intensity and concentration of NADH follow similar kinetics. The concentration measurement clearly indicated comparable profiles of transient depletion of NADH despite the varying levels of basal NADH in different cell types. Importantly, our real-time in situ analysis clearly indicates that although PARP is primarily activated in the nucleus in response to nuclear DNA damage, instantaneous NADH depletion occurs in both cytoplasm and nucleus, further highlighting the cell-wide metabolic effect of nucleus-initiated PARP activation.

The intracellular concentration of NADH was previously used to assess the single-strand break (SSB) repair capacity (as a surrogate indicator for NAD+ consumption by PARP) using a colorimetric assay of the media of a cell population[99,115]. However, no direct measurement at a single cell level in response to damage has been done. In our study, NADH depletion was entirely dependent on PARP1 activity, indicating that it is a consequence of PARP1 activation in response to DNA damage. The addition of NAM, the NAD+ precursor in the salvage pathway, abolished this change without suppressing PARP

activation, demonstrating that NADH reduction is due to NAD+ consumption by PARP1, rather than its PARylation activity. Interestingly, however, respiratory chain inhibition also blocked the NADH reduction despite intact PARP activation, indicating that NADH reduction in damaged cells is dependent on the mitochondrial complex activity and is not always an accurate marker for NAD+ consumption. We attempted to measure NAD+ directly using the recently developed NAD+ sensor[101] (Appendix B.2C). However, we were unable to monitor NAD+ using this sensor in the respiratory chain inhibitor-treated cells because the sensor activity is sensitive to acidic pHi in these cells (Figure 4.7C, data not shown). Nevertheless, it is clear that PARP is active (and thus, NAD+ is consumed) in these cells as additional PARP inhibition rescued the pH and cell death phenotypes. Taken together, the results strongly suggest that NAD+ depletion by activated PARP1 triggers the increased NADH consumption by the electron transport chain pathway in mitochondria, also consistent with the apparent increase of oxphos.
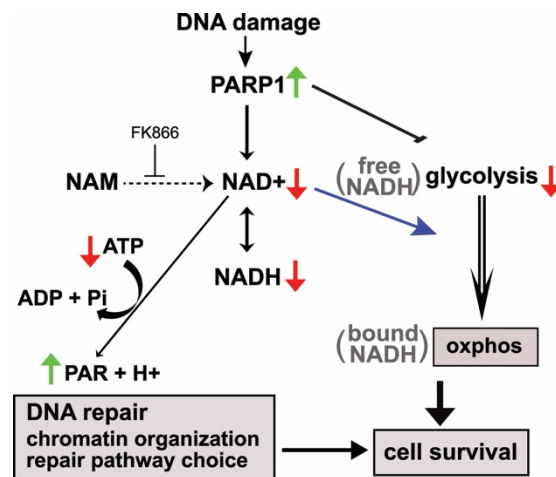
Figure 4.8. Consequences of PARP1 activation critical for damaged cell survival. *DNA damage complexity/dose-dependent PARP1 activation results in accumulation of PAR at damage sites that dictate recruitment of chromatin modifiers and DNA repair pathway choice. PARylation also suppresses glycolysis through inhibition of hexokinase. NAD+ consumption by PARylation also transiently decreases NADH, which can be measured by phasor-FLIM. Decreased NAD+ also triggers the shift NADH from free to bound state, which reflects the metabolic shift from glycolysis to oxphos, respectively. Both PARP-dependent modulation of DNA repair and metabolic switch promotes damaged cell survival.*

4.5.2 Transient and persistent increase of bound NADH by differential PARP activation

PARP signaling was thought to be rapid and transient, affecting immediate and early response at damage sites[76,87]. Indeed the PARP1 protein initially localizes at damage sites but disappears within 2 hr post damage induction[116]. In addition to the localized response at damage sites, however, our results demonstrate that PARP signaling alters both NADH concentration and the free to bound NADH ratio in both the nucleus and cytoplasm (Figure 4.8). NADH depletion is transient even with the high input-power damage induction, and its duration and extent are damage dose-dependent. The shift from free to bound NADH fraction is also transient in a damage dosage-dependent fashion for lower input-power damage. However, the shift becomes stabilized at high input-power damage that induces complex damage and robust PARP activation[88]. This is not associated with cell death, as the majority of cells remain viable with no sign of apoptosis or necrosis during the duration of our study. Since this shift is entirely PARP-dependent, our results demonstrate that there is a threshold PARP activation, above which the metabolic change becomes persistent.

4.5.3 PARP-dependent net increase of oxphos

Mitochondrial respiratory chain complex inhibitors inhibit the prolonged, but not the initial, increase of bound NADH fraction, revealing the biphasic response of NADH shift to the bound form in the cell, and strongly suggesting that the persistent increase reflects a metabolic shift or reprogramming to oxphos. Seahorse experiments suggest the strong suppression of glycolysis by damage-activated PARP as reported previously[24,90,91].

Although oxphos is also decreased by DNA damage, the extent of glycolysis suppression is greater so that there appears to be a net increase of oxphos. Consistent with this, damaged cells explicitly become sensitive to respiratory inhibition, which can be rescued by PARP inhibition.

If oxphos becomes critical in damaged cells, one may predict that cells with differential metabolic state may exhibit different sensitivity to respiration inhibition. Indeed, high basal level oxphos in primary human foreskin fibroblasts (HFF) appeared to mask the change in the cytoplasm. Importantly, these cells were insensitive to the dose of respiratory inhibitors that effectively killed HeLa or HCT116 cells. Thus, our results raise an important possibility that basal respiratory activity critically determines the fate of the damaged cells with robust PARP activation.

4.5.4 PARP-dependent NAD+ depletion results in the shift of metabolism to oxphos

PARP was shown to inhibit glycolysis through PAR-mediated inhibition of the critical enzyme hexokinases resulting in energy depletion and AIF-dependent parthanatos[24]. Our results indicate, however, that the shift to oxphos is the consequence of NAD+ consumption by PARP as the addition of NAM suppresses this shift, suggesting that NAD+ depletion, and not PARP activity, is the critical determinant of the metabolic shift. Thus, our analyses revealed a previously unrecognized long-term effect of NAD+ depletion by PARP activation on energy metabolism in DNA damaged cells.

4.6 Conclusion

In summary, our results demonstrate that the phasor-FLIM method allows the real-time visualization of dynamic single cell metabolic changes in response to DNA damage. With the combinatorial use of laser microirradiation and fluorescence biosensors, the method was highly instrumental in uncovering the damage-specific role of oxphos to promote ATP production and damaged cell survival.

4.7 Acknowledgments

CHAPTER 5

Molecular Dynamics of DNA Repair Factor Recruitment Using Two-Dimensional Pair Correlation of Fluorescence Fluctuations

5.1 Introduction

Responding to and repairing damaged DNA requires coordinating a number of cellular events far from the damage site including activating DNA repair, facilitating chromatin rearrangement, and delaying cell cycle progression. The signaling processes in the DNA damage response are tightly regulated by the molecular dynamics initiated at damage sites[117]. Previous work has analyzed the spatial distribution of double strand break (DSB) repair machinery[118] and DSB-containing chromatin domains[119]. Some proteins are restricted to a small area around the DSB while others spread up to a megabase away[118]. For DSBs, the immobilization of chromosome ends is critical for preventing translocations. Indeed, high precision tracking of broken chromosome ends has shown the ends to be positionally stable[120]. Although the spatial distribution and patterns of protein redistribution following DNA damage have been systematically documented, understanding the complex and often heterogeneous response to damage requires the characterization of the molecular dynamics of these proteins with high spatiotemporal resolution.

In order to visualize the spatiotemporal kinetics of DNA repair factor recruitment to DNA damage sites, highly localized damage in the cell nucleus needs to be induced. Recently, laser technology has been used to induce a variety of different lesions with a

number of excitation wavelengths[40]. In particular, ultrafast pulses of near infrared (NIR) microirradiation can induce localized DNA damage and initiate the DSB checkpoint response[42,88,106]. These methods of inducing DNA damage in a highly localized manner and at a precise time have enabled time-lapse studies to characterize the timing of repair factor recruitment [121]. However, there are still significant technological challenges to determining the dynamics of single molecules over the nuclear-wide landscape.

Current approaches to investigating molecular dynamics are lacking in spatiotemporal resolution, biological applicability, and/or the amount of information they can provide. While single particle tracking (SPT) could quantitatively describe molecular motion, it suffers from the need for specialized labeling with high signal-to-noise ratio (SNR) that introduce steric hindrances and for statistical robustness. Alternatively, fluorescence correlation spectroscopy (FCS) can provide single molecule sensitivity even in systems utilizing relatively dim genetically encoded fluorescent proteins with dense labeling as in living cells. Without needing to extract individual molecular trajectories, fluorescence fluctuation-based methods such as FCS and space-time image correlation spectroscopy (STICS) are able to provide information such as molecular flow and diffusion coefficients, but only for a single pixel or a small region. The development of the pair-correlation-function approach allows for the sensitive detection of barriers to diffusion by cross-correlating fluorescence fluctuations between a pair of points[51]. By scanning along a line, diffusive routes and obstacles to motion can be calculated between pairs of points along the line. This has been applied to the study of protein transport across the nuclear membrane and DNA repair factor motion in a dynamic chromatin environment[122,123]. However, this approach is still limited by predetermining the direction of motion along the

chosen line. Recently, the pair correlation function approach has been developed for two-dimensional images[52,53]. By calculating the spatiotemporal correlation function for every pixel in an image, the molecular dynamics of fluorescently-labeled proteins can be recorded without sacrificing spatial resolution over a large region.

Here we demonstrate the application of the 2D-pCF approach to visualize diffusion pathways of DNA repair proteins in response to NIR microirradiation-induced DNA damage. Comparison of the anisotropy of protein diffusion before and after damage reveals a marked change in the spatial landscape of the nucleus that differentially influences the average trajectories of DNA repair factors. In particular, we observe dramatic increases of anisotropic diffusion immediately surrounding damage sites. Analysis of the directionality of motion relative to the damage site differs between the three DNA repair proteins observed: Ku, Neil2, and PARP1. Furthermore, we observe a cell-cycle dependence on the diffusion of Ku at damage sites. The 2D-pCF approach presents a high spatiotemporal resolution method for characterizing the molecular trajectories of DNA repair proteins in the DNA damage response.

5.2 Materials and Methods

5.2.1 Cell culture and transfections

HeLa adenocarcinoma cells were cultured in DMEM (Invitrogen, Carlsbad, CA) supplemented with 10% fetal bovine serum, 2 mM L-glutamate, and 1% penicillin-streptomycin.

5.2.2 Thymidine block treatment

Cells were synchronized using the double thymidine block as described previously[124]. Briefly, cells were treated for 18 hr with 2.5 mM thymidine (Sigma-Aldrich, St. Louis, MO), released and incubated for 9 hr, and treated again with thymidine for 17 hr. The S phase synchronized cells were imaged 4 hr after release from the double thymidine block. For imaging G1 phase cells, M phase cells were first selected 8 hr after release from thymidine and then imaged in G1 phase after an additional 3 hr.

5.2.3 Confocal fluorescence microscope

All experiments were performed on an inverted confocal Zeiss LSM880 (Carl Zeiss, Jena, Germany) with a 40x 1.2NA water-immersion objective (Zeiss, Korr C-Apochromat).

5.2.4 NIR laser microirradiation

A pulsed Ti:Sapphire 100 fs laser (Spectra-Physics, Santa Clara, CA) at 80 MHz tuned to 780 nm was used for two-photon microirradiation at an input power of 22.6 mW measured after the objective. Defined regions of 0.8 x 7.5 microns that avoided the nuclear membrane and nucleolus were scanned once at 16.38 μs per pixel for damage induction.

5.2.5 Two-dimensional pair correlation function analysis

To acquire the fluorescence fluctuations for 2D-pCF analysis, image stacks of 128x128 pixels were acquired with a pixel size of 170 nm and a pixel time of 1.34 μs per pixel for 4,100 frames. GFP was excited using an argon ion laser with a 488 nm line and fluorescence was detected from 490 to 555 nm. mCherry was excited using a 561 nm DPSS

laser and fluorescence was detected from 580 to 650 nm. Fluorescence intensity images were generated from the sum of the image stacks using Fiji[125]. Images were segmented to isolate the nucleus including the nuclear membrane for analysis based on the intensity and brightfield images.

Data processing and calculation of the pair correlation functions were performed using the SimFCS software developed at the Laboratory for Fluorescence Dynamics as described previously[52,53]. Briefly, the pair correlation function (pCF) for a point $r_0 = (x_0, y_0)$ in an image of a time series stack $I(r,t)$ is calculated from the cross-correlation of fluorescence intensity measured at r_0 with that measured at coordinates $r_1 = (x_1, y_1)$ according to

$$pCF = G(\tau, r_0) = \frac{\langle I(t, r_0) \cdot I(t + \tau, r_0 + \delta r) \rangle_t}{\langle I(t, r_0) \rangle_t \langle I(t, r_0 + \delta r) \rangle_t} - 1$$

where $\langle \ldots \rangle_t$ indicates the temporal average, $\delta r = r_1 - r_0$, and τ is the time delay. The 2D-pCF measures the average path for a molecule diffusion in the cell and is subsequently able to detect obstacles to diffusion using the delay time of the correlation maximum. The angular representation of the 2D-pCF is then described by

$$Anisotropy = \frac{\lambda_1 - \lambda_2}{\lambda_1 + \lambda_2}$$

where λ_1 and λ_2 correspond to the major and minor axes of the ellipse generated from the first and second order moments of the 2D-pCF distribution. To reduce noise, only 2D-pCF values greater than 0.1 were considered for this analysis. The resulting anisotropy value in the range from 0 to 1 indicates the extent of asymmetry in the 2D-pCF ranging from pure isotropic diffusion to pure anisotropic motion, respectively. By considering the anisotropy values with the angle of the anisotropy direction, the average trajectories of molecules

along diffusive paths shaped by penetrable and impenetrable barriers can be visualized by joining line segments that correspond to the major axis of the 2D-pCF. The resulting "connectivity map" provides a high spatial resolution image of the pattern of molecular flow in the cell. To only examine regions exhibiting highly anisotropic behavior, the lower threshold for anisotropy was set at 0.3 for generating the connectivity maps.

To quantify the preferential orientation of anisotropy in sub-nuclear regions of interest (i.e. damage region, region surrounding damage site, non-damaged region, and nucleolus), the angles θ of the anisotropy were grouped into a normalized histogram and represented by the von Mises probability density function. The parameter κ measures the dispersion of the frequency of angles such that the value 0 suggests a uniform distribution of angles of anisotropy. An increase in the κ value indicates that angles θ become clustered around the mean direction μ and thus, a higher level of preferential orientation in the anisotropy. The angle that represents the preferred orientation of anisotropy is determined by the maximum value of the von Mises probability density function and is indicated by $\perp$ and || for perpendicular and parallel to the length of the rectangular region of damage, respectively. The analysis was performed in MATLAB (2017a, Mathworks, Natick, MA, USA).

5.3 Results

5.3.1 Visualization of the Molecular Flow of Ku Following NIR Microirradiation

A femtosecond two-photon NIR laser was used to induce highly localized DNA damage in HeLa cells stably expressing Ku-GFP. Localization of Ku to the damage site was

observed immediately following damage induction (Figure 5.1A, top panels). The fluorescence fluctuations between two points at a fixed distance of 6 pixels were sampled for 32 angles about one of the points and cross-correlated to calculate the 2D-pCF for every point in the image. The first and second order moments of the 2D-pCF were then used to calculate the anisotropy of the diffusion of Ku and generate a heat map based on the anisotropy value at each point (Figure 5.1A, middle panels). Connectivity maps generated from joining line segments exhibiting highly anisotropic motion (anisotropy values between 0.3 and 1.0) were plotted to visualize the average trajectories of Ku proteins (Figure 5.1A, bottom panels). The nuclear membrane is an impenetrable barrier to Ku as indicated by a high anisotropy of preferred motion and visualized by connectivity segments tangential to the membrane. The nucleolar periphery also exhibits anisotropic diffusion that is tangential to the edge of the nucleolus. The diffusion of Ku in the remainder of the nucleoplasm is primarily isotropic or weakly anisotropic.
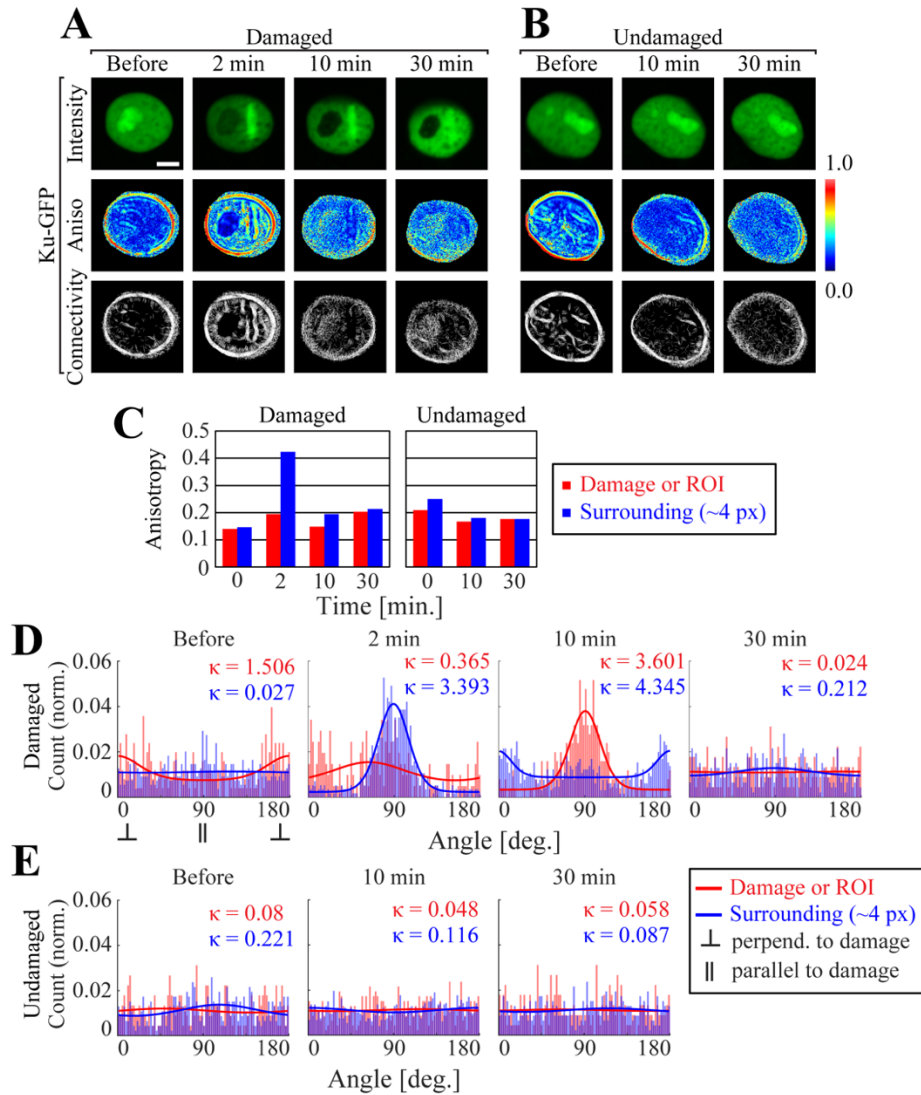
Figure 5.1. 2D-pCF analysis of Ku-GFP recruitment to microirradiation-induced DNA damage. *(A)
Fluorescence intensity images of Ku-GFP following microirradiation generated from the sum of 4100 frames.
Heat maps of anisotropy were generated from the 2D-pCF. Connectivity maps were generated from joining
segments of high anisotropy (anisotropy > 0.3). Scale bar = 5 μm. (B) Fluorescence intensity, anisotropy heat
map, and connectivity map images for non-microirradiated cells. (C) Bar graph of the anisotropy over time in
damaged and undamaged cells. (D) The von Mises probability density function represents the preferential
orientation of anisotropy within the damage site (red) or in the region surrounding the damage site (blue, within
4 pixels). The symbols ⊥ and || indicate a preferred orientation perpendicular and parallel to the length of the
rectangular region of damage, respectively. (E) The von Mises function for non-microirradiated region of
interest (ROI, red) or in the region surrounding the ROI (blue).*

Upon damage, Ku diffusion becomes highly anisotropic at the edge of the damage

site suggesting that DNA damage causes barriers to form around the region of damage

(Figure 5.1C, Appendix C.1). However, Ku diffusion within the damage site exhibits low anisotropy, but this may be due to the loss of chromatin structure (Appendix C.2). The connectivity map indicates that Ku tends to move around the rectangular region of damage suggesting that the diffusion of Ku in response to localized damage may have a transient initial response of Ku accumulation at the damage site and a more persistent effect of excluding excess Ku from the damage site. Representing the preferential orientation of anisotropy using the von Mises probability density function shows that the region surrounding the damage site immediately following damage induction has a strong preference for diffusion that is parallel to edge of the damage site as evidenced by a high κ parameter (Figure 5.1D, Appendix C.1). Interestingly, this preferred orientation of Ku diffusion in the region surrounding the damage site changes to perpendicular to the damage site at 10 min after damage. Although the anisotropy value within the region of damage is low, the orientation of Ku diffusion is strongly aligned parallel to the length of the microirradiated tract. Without DNA damage, there is not strong preferential orientation of anisotropy (Figure 5.1E). Ku found in the nucleolus rapidly vacates upon DNA damage induction and moves radially outward from the nucleolus as shown on the connectivity map (Figure 5.1A, bottom panels). The directionality of Ku movement around the nucleolus completely changes from tangential to perpendicular with respect to the nucleolar periphery. At 10 min after damage, Ku is still accumulated at the damage site as indicated by the intensity image, but barriers to Ku motion begin to disappear enabling isotropic diffusion by 30 min after damage. There does not appear to be a significant change in the anisotropy of Ku diffusion without damage (Figure 5.1B and C).

5.3.2 Differential Effect of Cell Cycle on Molecular Flow of Ku

DNA double strand breaks (DSBs) are repaired by homologous recombination (HR) and non-homologous end joining (NHEJ). Because it requires a homologous DNA template, HR is only active in the S/G2 phase of the cell cycle whereas NHEJ directly ligates DNA ends and is not restricted to a certain phase of the cell cycle. HR is believed to be the preferred DNA repair pathway in S/G2 phase when sister chromatids are present while NHEJ is assumed to be the dominant repair pathway in G1 phase. HR and NHEJ factors compete for the DNA ends for repair and so the phase of the cell cycle may influence the behavior of these proteins. In particular, the Ku heterodimer is a ring-like structure that strongly binds to free DNA ends to initiate NHEJ and competes with the Mre11-Rad50-NBS1 (MRN) complex, which initiates HR. Thus, cells were synchronized via thymidine block for S/G2 or G1 phase and the 2D-pCF of Ku-GFP following microirradiation was calculated. Ku accumulation at the damage site was observed immediately following damage induction in both S/G2 and G1 phase cells (Figure 5.2). As with asynchronous cells, the anisotropy of Ku diffusion increases directly adjacent to damage sites independent of the cell cycle. However, the magnitude of anisotropic motion of Ku in S/G2 phase cells at the damage site is greater than that in G1 phase cells (Figure 5.2). Furthermore, the increased anisotropy at damage sites persists for more than 30 min in S/G2 phase cells whereas in G1 phase cells, the anisotropy of Ku becomes homogenous throughout the nucleus beginning 10 min after damage. The connectivity maps of Ku trajectories in S/G2 and G1 phase cells show that barriers to Ku diffusion are more persistent in S/G2 phase cells than G1 phase cells indicating a cell cycle dependence on the molecular motion of Ku.
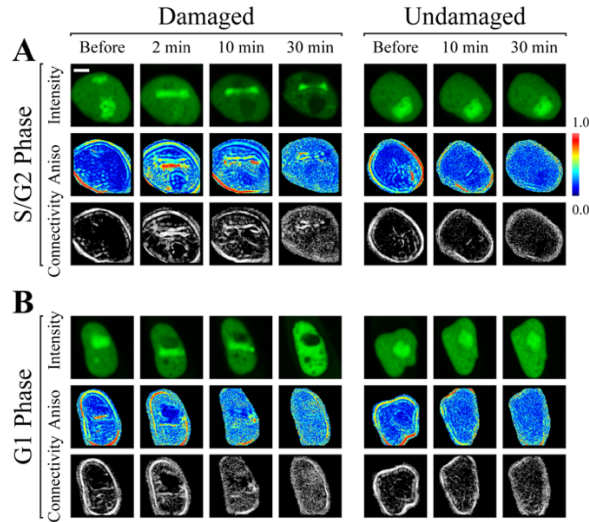
Figure 5.2. Molecular flow of Ku-GFP following DNA damage is cell cycle dependent. *(A) Fluorescence intensity, anisotropy heat map, and connectivity map images for damaged and undamaged cells synchronized to S/G2 phase by double thymidine block. Scale bar = 5 μm. (B) Fluorescence intensity, anisotropy heat map, and connectivity map images for damaged and undamaged cells synchronized to G1 phase.*

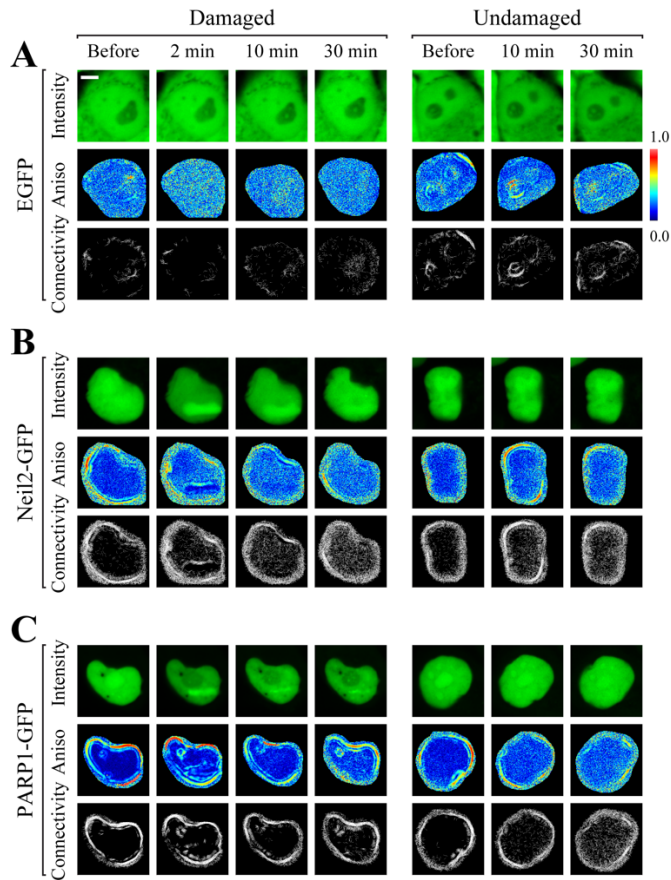**Figure 5.3. Differential formation of barriers to the molecular flow of DNA repair proteins following microirradiation.** *Fluorescence intensity, anisotropy heat map, and connectivity map images for damaged and undamaged cells expressing (A) EGFP, (B) Neil2-GFP, or (C) PARP1-GFP. Scale bar = 5 μm.*

5.3.3 Differential Formation of Barriers to the Molecular Flow of DNA Repair Proteins Following NIR Microirradiation

To compare the molecular trajectories of different DNA damage-associated proteins following localized DNA damage, HeLa cells expressing Neil2-GFP, PARP1-GFP, or EGFP were microirradiated and the 2D-pCF was calculated for each image. While the motion of EGFP appears to be affected by the nucleolus, it does not appear to be influenced by microirradiation (Figure 5.3A). The lack of anisotropic diffusion at the nuclear periphery suggests that EGFP is able to diffuse across the nuclear membrane. Analysis of the angles of anisotropic motion yields no preferential orientation (Figure 5.4A, Appendix C.3). Microirradiation can introduce complex DNA damage and the recruitment of Neil2-GFP to irradiated regions suggests the induction of base damages (Figure 5.3B, top panels). The 2D-pCF calculations show that Neil2-GFP has a damage-dependent increase of anisotropy surrounding the damage site (Figure 5.3B, middle panels). As was observed with Ku-GFP, the connectivity map indicates that Neil2 also tends to diffuse around the damage site (Figure 5.3B, bottom panels, Figure 5.4B). In contrast, while PARP1 also demonstrates an increase of anisotropy surrounding the damage site, the connectivity maps suggest the formation of channels that facilitate diffusion toward and away from the damage site for PARP1 instead of barriers that restrict motion toward the damage site as was observed for Neil2 and Ku (Figure 5.3C, bottom panels, Figure 5.4C).
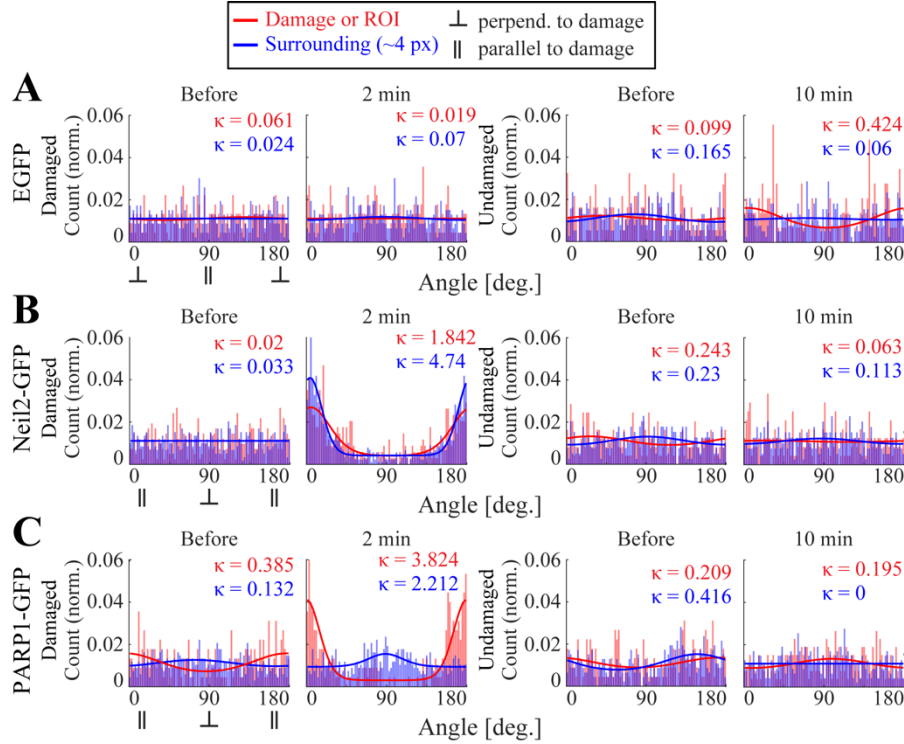
Figure 5.4. von Mises probability density function analysis of EGFP, Neil2-GFP, or PARP1-GFP following microirradiation. *The 2D-pCF is calculated for HeLa cells expressing (A) EGFP, (B) Neil2-GFP, or (C) PARP1-GFP. The von Mises probability density function represents the preferential orientation of anisotropy within the damage site (red) or in the region surrounding the damage site (blue, within 4 pixels) (left). The symbols ⊥ and || indicate a preferred orientation perpendicular and parallel to the length of the rectangular region of damage, respectively. The von Mises function for non-microirradiated region of interest (ROI, red) or in the region surrounding the ROI (blue) (right).*

5.4 Discussion

Here, we use the 2D-pCF to characterize the average molecular trajectories of Ku,

Neil2, and PARP1 in the DNA damage response following nanoscale induction of DNA

damage. While previous methods have been able to extract spatial information about DNA

repair activity using confocal microscopy and temporal dynamics of recruitment at damage

sites using techniques such as fluorescence recovery after photobleaching (FRAP), dual foci

FCS and pCF for a line scan, the 2D-pCF approach demonstrated here is able to characterize

the spatial landscape consisting of barriers and pathways for diffusion in the entire nucleus

and describe the molecular dynamics of specific DNA repair proteins distant and adjacent to damage sites simultaneously. Using the von Mises probability density function to represent the preferred orientation of the angles of anisotropic diffusion reveals that there is a significant damage-dependent change in the diffusion patterns of different DNA repair proteins.

Using the 2D-pCF, we were able to observe the dynamics of Ku diffusion that differed from the intensity image that showed its spatial distribution. Because Ku strongly binds to DNA ends, it will continue to accumulate at the damage site as long as there are exposed DNA ends, which depends on the number of DSBs induced[9]. Although Ku continued to be present at damage sites up to 30 min after microirradiation, the lack of high anisotropy of Ku diffusion and connectivity suggests that additional Ku proteins are not recruited to the damage site after the initial response. Neil2 demonstrated similar trends on the connectivity map and with preferential orientation of anisotropy given by the von Mises probability density function as was observed with Ku. Neil2 binds to DNA and undergoes a processive search in order to find DNA lesions[126,127]. In this way, interactions between these DNA repair proteins Ku and Neil2 and DNA are relatively long-lived. However, PARP1 remains active following the initial response to DNA damage[7]. PARylation of target proteins and autoPARylation facilitates multiple waves of DNA repair factor recruitment and additional PARP1 accumulation at damage sites. The 2D-pCF analysis and connectivity map is able to capture this phenomenon and visualize PARP1 motion toward and away from the damage site.

We also observed a cell cycle dependence of the molecular trajectories of Ku. It is known that HR and NHEJ require distinct sets of DNA repair proteins[16,128]. Furthermore,

HR repair factors compete with NHEJ factors for repair pathway choice[116,129,130]. Analysis with the 2D-pCF shows that the anisotropy of Ku around damage sites is more persistent in S/G2 phase than in G1 phase. This could be due to the competition between HR and NHEJ repair factors that prolongs the accumulation of Ku at damage site and thus, efficient repair of damaged DNA.

5.5 Conclusion

In summary, we present a high spatiotemporal resolution method using fluorescence fluctuations in the entire nucleus for characterizing the molecular trajectories of DNA repair proteins in the DNA damage response. Analysis by 2D-pCF indicates that microirradiation induces significant changes to the trajectories of molecular flow of DNA repair proteins in and around the damage site as well as in the nucleolus. Representation using the von Mises probability density function shows that the preferential orientation of anisotropy is strongly affected by the DNA damage site. This technique can be applied to a number of biological systems not limited to the nucleus including vesicle motion, membrane protein dynamics, and metabolic signaling to identify pathways for diffusion of fluorescently labeled proteins.

CHAPTER 6

Summary and Conclusions

The DNA damage response is a complex signal transduction pathway that is capable of responding to a variety of threats to genome integrity and can coordinate a number of cellular events including DNA repair, chromatin rearrangement, and cell cycle progression. Beginning at damage sites, DNA repair signaling is transduced throughout the entire cell and needs to be tightly regulated in a spatial, temporal, and DNA-lesion specific manner. Experimental tools that enable analysis of DNA repair mechanisms and signaling with high spatiotemporal resolution can provide information on how the DDR can control critical regulatory functions in cells.

The enzymatic pathways such as cellular metabolism that catabolize and anabolize cellular components enable cells to immediately respond to urgent needs. As demonstrated in Chapters 3 and 4 using fluorescence lifetime imaging microscopy, DNA repair signaling can influence cellular metabolism. The combinatorial use of sub-cellular-targeted fluorescent biosensors helped to elucidate the role of metabolic regulation in responding to damaged DNA. We found that the ubiquitous tumor suppressor protein p53 can upregulate oxidative phosphorylation in the absence of the reversionless 3-like (REV3L) translesional synthesis DNA repair protein in response to cisplatin-induced intrastrand crosslinks. This study provides some insight into the role of REV3L in metabolism and its interaction with the tumor suppressor p53, which is critical for understanding how drug resistance can develop in H1299 lung carcinoma cells to this commonly used chemotherapy treatment. Furthermore, although it was known that over-activation of PARP could dramatically consume NAD+ leading to an overall metabolic collapse and subsequent cell death, high

resolution spatiotemporal analyses here showed that NAD+ and NADH levels are not necessarily concordant and that cellular reliance on oxphos could be modulated in a PARP-dependent manner for cell survival. This led to the discovery of a previously unrecognized long-term effect of DNA repair signaling on energy metabolism in DNA damaged cells.

Methods using fluorescence correlations have enabled the characterization of the molecular dynamics of proteins with high spatiotemporal resolution. However, there remained significant technological barriers to expanding these techniques to entire sub-cellular regions. With spatial pair cross-correlation function analysis in two-dimensions, the molecular motion of DNA repair proteins in response to DNA damage was visualized in a new way. In the study in Chapter 5, traditional laser scanning technology was used to acquire the fluorescence fluctuations, but it is possible that fast processes are not captured due to slow acquisition speeds. Recently, a hexagonal array of 32 GaAsP PMT detectors coupled with shaping the excitation beam before it enters the objective lens back aperture has been developed to enable fast acquisition speeds without sacrificing pixel dwell times[131]. Because of the increase in frame acquisition speed, a very high temporal resolution can be achieved and the fluorescence fluctuations of fast moving molecules in very transient processes can be correlated. Thus, there is still more that can be done to increase the spatiotemporal resolution of fluorescence correlation methods to investigate the DNA damage response.

REFERENCES

1   Hoeijmakers, J. H. J. DNA Damage, Aging, and Cancer. *N Engl J Med* **361**, 1475-1485 (2009).

2   Jackson, S. P. & Bartek, J. The DNA-damage response in human biology and disease. *Nature* **461**, 1071-1078, doi:10.1038/nature08467 (2009).

3   Hoeijmakers, J. H. J. Genome maintenance mechanisms for preventing cancer. *Nature* **411**, 366-374 (2001).

4   Genois, M. M. *et al.* DNA repair pathways in trypanosomatids: from DNA repair to drug resistance. *Microbiol Mol Biol Rev* **78**, 40-73, doi:10.1128/MMBR.00045-13 (2014).

5   Ciccia, A. & Elledge, S. J. The DNA damage response: making it safe to play with knives. *Mol Cell* **40**, 179-204, doi:10.1016/j.molcel.2010.09.019 (2010).

6   Lee, S. E. *et al.* Saccharomyces Ku70, Mre11/Rad50, and RPA Proteins Regulate Adaptation to G2/M Arrest after DNA Damage. *Cell* **94**, 399-409 (1998).

7   Mortusewicz, O., Ame, J. C., Schreiber, V. & Leonhardt, H. Feedback-regulated poly(ADP-ribosyl)ation by PARP-1 is required for rapid response to DNA damage in living cells. *Nucleic Acids Res* **35**, 7665-7675, doi:10.1093/nar/gkm933 (2007).

8   Hassa, P. O., Haenni, S. S., Elser, M. & Hottiger, M. O. Nuclear ADP-ribosylation reactions in mammalian cells: where are we today and where are we going? *Microbiol Mol Biol Rev* **70**, 789-829, doi:10.1128/MMBR.00040-05 (2006).

9   Walker, J. R., Corpina, R. A. & Goldberg, J. Structure of the Ku heterodimer bound to DNA and its implications for double-strand break repair. *Nature* **412**, 607-614 (2001).

10   Cary, R. B. *et al.* DNA looping by Ku and the DNA-dependent protein kinase. *Proc Natl Acad Sci U S A* **94**, 4267-4272 (1997).

11   Ramsden, D. A. & Gellert, M. Ku protein stimulates DNA end joining by mammalian DNA ligases: a direct role for Ku in repair of DNA double-strand breaks. *EMBO J* **17**, 609-614 (1998).

12   Gottlieb, T. M. & Jackson, S. P. The DNA-Dependent Protein Kinase: Requirement for DNA Ends and Association with Ku Antigen. *Cell* **72**, 131-142 (1993).

13   Lees-Miller, S. P., Sakaguchi, K., Ullrich, S. J., Appella, E. & Anderson, C. W. Human DNA-Activated Protein Kinase Phosphorylates Serines 15 and 38 in the Amino-Terminal Transactivation Domain of Human p53. *Mol Cell Biol* **12**, 5041-5049 (1992).

14   Ko, L. J. & Prives, C. p53: puzzle and paradigm. *Genes Dev* **10**, 1054-1072 (1996).

15   Williams, R. S., Williams, J. S. & Tainer, J. A. Mre11-Rad50-Nbs1 is a keystone complex connecting DNA repair machinery, double-strand break signaling, and the chromatin template. *Biochem Cell Biol* **85**, 509-520, doi:10.1139/O07-069 (2007).

16   West, S. C. Molecular views of recombination proteins and their control. *Nature Reviews Molecular Cell Biology* **4**, 435-445, doi:10.1038/nrm1127 (2003).

17   Stark, J. M. & Jasin, M. Extensive Loss of Heterozygosity Is Suppressed during Homologous Repair of Chromosomal Breaks. *Molecular and Cellular Biology* **23**, 733-743, doi:10.1128/mcb.23.2.733-743.2003 (2003).

18   Rouse, J. & Jackson, S. P. Interfaces between the detection, signaling, and repair of DNA damage. *Science* **297**, 547-551, doi:10.1126/science.1074740 (2002).

19   Rogakou, E. P., Pilch, D. R., Orr, A. H., Ivanova, V. S. & Bonner, W. M. DNA Double-stranded Breaks Induce Histone H2AX Phosphorylation on Serine 139. *J Biol Chem* **273**, 5858-5868 (1998).

20   Downs, J. A. *et al.* Binding of chromatin-modifying activities to phosphorylated histone H2A at DNA damage sites. *Mol Cell* **16**, 979-990, doi:10.1016/j.molcel.2004.12.003 (2004).

21   Stucki, M. & Jackson, S. P. gammaH2AX and MDC1: anchoring the DNA-damage-response machinery to broken chromosomes. *DNA Repair (Amst)* **5**, 534-543, doi:10.1016/j.dnarep.2006.01.012 (2006).

22   Ishikawa, K., Ishii, H. & Saito, T. DNA Damage-Dependent Cell Cycle Checkpoints and Genomic Stability. *DNA Cell Biol* **25**, 406-411 (2006).

23   Krebs, H. A. The history of the tricarboxylic acid cycle. *Perspect Biol Med* **14**, 154-170 (1970).

24   Andrabi, S. A. *et al.* Poly(ADP-ribose) polymerase-dependent energy depletion occurs through inhibition of glycolysis. *Proc Natl Acad Sci U S A* **111**, 10209-10214, doi:10.1073/pnas.1405158111 (2014).

25   Korkes, S., del Campillo, A., Gunsalus, I. C. & Ochoa, S. Enzymatic Synthesis of Citric Acid. *J Biol Chem* **193**, 721-735 (1951).

26   Williamson, J. R. & Cooper, R. H. Regulation of the Citric Acid Cycle in Mammalian Systems. *FEBS Lett* **117**, K73-K85 (1980).

27   Lukas, J., Lukas, C. & Bartek, J. More than just a focus: The chromatin response to DNA damage and its role in genome integrity maintenance. *Nat Cell Biol* **13**, 1161-1169, doi:10.1038/ncb2344 (2011).

28   Gut, P. & Verdin, E. The nexus of chromatin regulation and intermediary metabolism. *Nature* **502**, 489-498, doi:10.1038/nature12752 (2013).

29   Lehninger, A. L. The Mitochondrion. *Benjamin* (1966).

30   Wainio, W. The Mammalian Mitochondrial Respiratory Chain. *Academic Press* (1970).

31   Rossetto, D., Truman, A. W., Kron, S. J. & Cote, J. Epigenetic modifications in double-strand break DNA damage signaling and repair. *Clin Cancer Res* **16**, 4543-4552, doi:10.1158/1078-0432.CCR-10-0513 (2010).

32   Dizdaroglu, M., Nackerdien, Z., Chao, B.-C., Gajewski, E. & Rao, G. Chemical Nature of in Vivo DNA Base Damage in Hydrogen Peroxide-Treated Mammalian Cells. *Arch Biochem Biophys* **285**, 388-390 (1991).

33   Henle, E. S. & Linn, S. Formation, Prevention, and Repair of DNA Damage by Iron/Hydrogen Peroxide. *J Biol Chem* **272**, 19095-19098 (1997).

34   Lundin, C. *et al.* Methyl methanesulfonate (MMS) produces heat-labile DNA damage but no detectable in vivo DNA double-strand breaks. *Nucleic Acids Res* **33**, 3799-3811, doi:10.1093/nar/gki681 (2005).

35   Chu, G. Cellular Responses to Cisplatin. *J Biol Chem* **269**, 787-790 (1994).

36   Eastman, A. Reevaluation of Interaction of cis-Dichloro(ethylenediamine)platinum(II) with DNA. *Biochemistry* **25**, 3912-3915 (1986).

37   Dinant, C. *et al.* Activation of multiple DNA repair pathways by sub-nuclear damage induction methods. *J Cell Sci* **120**, 2731-2740, doi:10.1242/jcs.004523 (2007).

38   Essers, J., Vermeulen, W. & Houtsmuller, A. B. DNA damage repair: anytime, anywhere? *Curr Opin Cell Biol* **18**, 240-246, doi:10.1016/j.ceb.2006.03.004 (2006).

39   Rapp, A. & Greulich, K. O. After double-strand break induction by UV-A, homologous recombination and nonhomologous end joining cooperate at the same DSB if both systems are available. *J Cell Sci* **117**, 4935-4945, doi:10.1242/jcs.01355 (2004).

40   Kong, X. *et al.* Comparative analysis of different laser systems to study cellular responses to DNA damage in mammalian cells. *Nucleic Acids Res* **37**, e68., doi:10.1093/nar/gkp221 (2009).

41   Gomez-Godinez, V., Wakida, N. M., Dvornikov, A. S., Yokomori, K. & Berns, M. W. Recruitment of DNA damage recognition and repair pathway proteins following near-IR femtosecond laser irradiation of cells. *J Biomed Opt* **12**, 020505, doi:10.1117/1.2717684 (2007).

42   Meldrum, R. A., Botchway, S. W., Wharton, C. W. & Hirst, G. J. Nanoscale spatial induction of ultraviolet photoproducts in cellular DNA by three-photon near-infrared absorption. *EMBO Rep* **4**, 1144-1149, doi:10.1038/sj.embor.7400028 (2003).

43   Meyer, B. *et al.* Clustered DNA damage induces pan-nuclear H2AX phosphorylation mediated by ATM and DNA-PK. *Nucleic Acids Res* **41**, 6109-6118, doi:10.1093/nar/gkt304 (2013).

44   Gratton, E. *et al.* Fluorescence Lifetime Distribution of Folded and Unfolded Proteins. *Int J Quantum Chem* **42**, 1479-1489 (1992).

45   Alcala, J. R., Gratton, E. & Prendergast, F. G. Interpretation of Fluorescence Decays in Proteins Using Continuous Lifetime Distribution. *Biophys J* **51**, 925-936 (1987).

46   Digman, M. A., Caiolfa, V. R., Zamai, M. & Gratton, E. The phasor approach to fluorescence lifetime imaging analysis. *Biophys J* **94**, L14-16, doi:10.1529/biophysj.107.120154 (2008).

47   Wright, B. K. *et al.* NADH distribution in live progenitor stem cells by phasor-fluorescence lifetime image microscopy. *Biophys J* **103**, L7-9, doi:10.1016/j.bpj.2012.05.038 (2012).

48   Wright, B. K. *et al.* Phasor-FLIM analysis of NADH distribution and localization in the nucleus of live progenitor myoblast cells. *Microsc Res Tech* **75**, 1717-1722, doi:10.1002/jemt.22121 (2012).

49   Stringari, C. *et al.* Phasor approach to fluorescence lifetime microscopy distinguishes different metabolic states of germ cells in a live tissue. *Proc Natl Acad Sci U S A* **108**, 13582-13587, doi:10.1073/pnas.1108161108 (2011).

50   Kong, L., Murata, M. M. & Digman, M. A. Absence of REV3L promotes p53-regulated cancer cell metabolism in cisplatin-treated lung carcinoma cells. *Biochem Biophys Res Commun* **496**, 199-204, doi:10.1016/j.bbrc.2018.01.026 (2018).

51   Digman, M. A. & Gratton, E. Imaging barriers to diffusion by pair correlation functions. *Biophys J* **97**, 665-673, doi:10.1016/j.bpj.2009.04.048 (2009).

52   Di Rienzo, C., Cardarelli, F., Di Luca, M., Beltram, F. & Gratton, E. Diffusion Tensor Analysis by Two-Dimensional Pair Correlation of Fluorescence Fluctuations in Cells. *Biophys J* **111**, 841-851, doi:10.1016/j.bpj.2016.07.005 (2016).

53   Malacrida, L., Hedde, P. N., Ranjit, S., Cardarelli, F. & Gratton, E. Visualization of barriers and obstacles to molecular diffusion in live cells by spatial pair-cross-correlation in two dimensions. *Biomed Opt Express* **9**, 303-321, doi:10.1364/BOE.9.000303 (2018).

54   Ferlay, J. *et al.* Cancer incidence and mortality worldwide: sources, methods and major patterns in GLOBOCAN 2012. *Int J Cancer* **136**, E359-386, doi:10.1002/ijc.29210 (2015).

55   Dasari, S. & Tchounwou, P. B. Cisplatin in cancer therapy: molecular mechanisms of action. *Eur J Pharmacol* **740**, 364-378, doi:10.1016/j.ejphar.2014.07.025 (2014).

56   Zilfou, J. T. & Lowe, S. W. Tumor suppressive functions of p53. *Cold Spring Harb Perspect Biol* **1**, a001883, doi:10.1101/cshperspect.a001883 (2009).

57   Shen, D. W., Pouliot, L. M., Hall, M. D. & Gottesman, M. M. Cisplatin resistance: a cellular self-defense mechanism resulting from multiple epigenetic and genetic changes. *Pharmacol Rev* **64**, 706-721, doi:10.1124/pr.111.005637 (2012).

58   Waters, L. S. *et al.* Eukaryotic translesion polymerases and their roles and regulation in DNA damage tolerance. *Microbiol Mol Biol Rev* **73**, 134-154, doi:10.1128/MMBR.00034-08 (2009).

59   Gan, G. N., Wittschieben, J. P., Wittschieben, B. O. & Wood, R. D. DNA polymerase zeta (pol zeta) in higher eukaryotes. *Cell Res* **18**, 174-183, doi:10.1038/cr.2007.117 (2008).

60   Wang, W. *et al.* REV3L modulates cisplatin sensitivity of non-small cell lung cancer H1299 cells. *Oncol Rep* **34**, 1460-1468, doi:10.3892/or.2015.4121 (2015).

61   Singh, B. *et al.* Human REV3 DNA Polymerase Zeta Localizes to Mitochondria and Protects the Mitochondrial Genome. *PLoS One* **10**, e0140409, doi:10.1371/journal.pone.0140409 (2015).

62   Knobel, P. A., Kotov, I. N., Felley-Bosco, E., Stahel, R. A. & Marti, T. M. Inhibition of REV3 Expression Induces Persistent DNA Damage and Growth Arrest in Cancer Cells. *Neoplasia* **13**, 961-IN928, doi:10.1593/neo.11828 (2011).

63   Warburg, O., Wind, F. & Negelein, E. The metabolism of tumors in the body. *J Gen Physiol* (1927).

64   Puzio-Kuter, A. M. The Role of p53 in Metabolic Regulation. *Genes Cancer* **2**, 385-391, doi:10.1177/1947601911409738 (2011).

65   Sullivan, E. J. Metabolic Changes Associated with Acquired Cisplatin Resistance. *Open Access Dissertations* **1192** (2014).

66   Chappell, W. H. *et al.* p53 expression controls prostate cancer sensitivity to chemotherapy and the MDM2 inhibitor Nutlin-3. *Cell Cycle* **11**, 4579-4588, doi:10.4161/cc.22852 (2012).

67   Stringari, C., Nourse, J. L., Flanagan, L. A. & Gratton, E. Phasor fluorescence lifetime microscopy of free and protein-bound NADH reveals neural stem cell differentiation potential. *PLoS One* **7**, e48014, doi:10.1371/journal.pone.0048014 (2012).

68   Fath, M. A. *et al.* Mitochondrial electron transport chain blockers enhance 2-deoxyD-glucose induced oxidative stress and cell killing in human colon carcinoma cells. *Cancer Biol Ther.* **8**, 1228-1236 (2009).

69   di Pietro, A. *et al.* Pro- and anti-apoptotic effects of p53 in cisplatin-treated human testicular cancer are cell context-dependent. *Cell Cycle* **11**, 4552-4562, doi:10.4161/cc.22803 (2012).

70   Shen, L. *et al.* The fundamental role of the p53 pathway in tumor metabolism and its implication in tumor therapy. *Clin Cancer Res* **18**, 1561-1567, doi:10.1158/1078-0432.CCR-11-3040 (2012).

71   Caldon, C. E. Estrogen signaling and the DNA damage response in hormone dependent breast cancers. *Front Oncol* **4**, 106, doi:10.3389/fonc.2014.00106 (2014).

72   Gupte, R., Liu, Z. & Kraus, W. L. PARPs and ADP-ribosylation: recent advances linking molecular functions to biological outcomes. *Genes Dev.* **31**, 101-126. (2017).

73   Ahel, D. *et al.* Poly(ADP-ribose)-dependent regulation of DNA repair by the chromatin remodeling enzyme ALC1. *Science* **325**, 1240-1243., doi:10.1126/science.1177321 (2009).

74   Altmeyer, M. *et al.* Liquid demixing of intrinsically disordered proteins is seeded by poly(ADP-ribose). *Nat Commun* **6**, 8088. (2015).

75   Ayrapetov, M. K., Gursoy-Yuzugullu, O., Xu, C., Xu, Y. & Price, B. D. DNA double-strand breaks promote methylation of histone H3 on lysine 9 and transient formation of repressive chromatin. *Proc Natl Acad Sci U S A* **111**, 9169-9174., doi:10.1073/pnas.1403565111 (2014).

76   Ball, A. R., Jr. & Yokomori, K. Damage site chromatin: open or closed? *Curr Opin Cell Biol* **23**, 277-283., doi:10.1016/j.ceb.2011.03.012 (2011).

77   Bouwman, P. *et al.* 53BP1 loss rescues BRCA1 deficiency and is associated with triple-negative and BRCA-mutated breast cancers. *Nat Struc Mol Biol* **17**, 688-695., doi:10.1038/nsmb.1831 (2010).

78   Chou, D. M. *et al.* A chromatin localization screen reveals poly (ADP ribose)-regulated recruitment of the repressive polycomb and NuRD complexes to sites of DNA damage. *Proc Natl Acad Sci U S A* **107**, 18475-18480., doi:10.1073/pnas.1012946107 (2010).

79   Gottschalk, A. J. *et al.* Poly(ADP-ribosyl)ation directs recruitment and activation of an ATP-dependent chromatin remodeler. *Proc Natl Acad Sci U S A* **106**, 13770-13774., doi:10.1073/pnas.0906920106 (2009).

80   Izhar, L. *et al.* A Systematic Analysis of Factors Localized to Damaged Chromatin Reveals PARP-Dependent Recruitment of Transcription Factors. *Cell Rep* **11**, 1486-1500. , doi:10.1016/j.celrep.2015.04.053 (2015).

81   Jaspers, J. E. *et al.* Loss of 53BP1 causes PARP inhibitor resistance in Brca1-mutated mouse mammary tumors. *Cancer Discov.* **3**, 68-81., doi:10.1158/2159-8290.CD-12-0049 (2013).

82   Khoury-Haddad, H. *et al.* PARP1-dependent recruitment of KDM4D histone demethylase to DNA damage sites promotes double-strand break repair. *Proc Natl Acad Sci U S A* **111**, E728-737., doi:10.1073/pnas.1317585111 (2014).

83   Larsen, D. H. *et al.* The chromatin-remodeling factor CHD4 coordinates signaling and repair after DNA damage. *J Cell Biol* **190**, 731-740., doi:10.1083/jcb.200912135 (2010).

84   Polo, S. E., Kaidi, A., Baskcomb, L., Galanty, Y. & Jackson, S. P. Regulation of DNA-damage responses and cell-cycle progression by the chromatin remodelling factor CHD4. *EMBO J* **29**, 3130-3139., doi:10.1038/emboj.2010.188 (2010).

85   Smeenk, G. *et al.* The NuRD chromatin-remodeling complex regulates signaling and repair of DNA damage. *J Cell Biol* **190**, 741-749., doi:10.1083/jcb.201001048 (2010).

86   Sun, Y. *et al.* Histone H3 methylation links DNA damage detection to activation of the tumour suppressor Tip60. *Nat Cell Biol* **11**, 1376-1382., doi:10.1038/ncb1982 (2009).

87   Polo, S. E. & Jackson, S. P. Dynamics of DNA damage response proteins at DNA breaks: a focus on protein modifications. *Genes Dev* **25**, 409-433, doi:10.1101/gad.2021311 (2011).

88   Cruz, G. M. S. *et al.* Femtosecond near-infrared laser microirradiation reveals a crucial role for PARP signaling on factor assemblies at DNA damage sites. *Nucleic Acids Res* **44**, e27., doi:10.1093/nar/gkv976 (2015).

89   Heikal, A. A. Intracellular coenzymes as natural biomarkers for metabolic activities and mitochondrial anomalies. *Biomark. Med.* **4**, 241-263. (2010).

90   Feng, F. Y., de Bono, J. S., Rubin, M. A. & Knudsen, K. E. Chromatin to Clinic: The Molecular Rationale for PARP1 Inhibitor Function. *Mol Cell* **58**, 925-934., doi:10.1016/j.molcel.2015.04.016 (2015).

91   Fouquerel, E. *et al.* ARTD1/PARP1 negatively regulates glycolysis by inhibiting hexokinase 1 independent of NAD+ depletion. *Cell Rep* **8**, 1819-1831, doi:10.1016/j.celrep.2014.08.036 (2014).

92   Andrabi, S. A., Dawson, T. M. & Dawson, V. L. Mitochondrial and nuclear cross talk in cell death: parthanatos. *Ann. N. Y. Acad. Sci.* **1147**, 233-241. (2008).

93   Fatokun, A. A., Dawson, V. L. & Dawson, T. M. Parthnatos: mitochondrial-linked mechanisms and therapeutic opportunities. *Br. J. Pharmacol.* **171**, 2000-2016. (2014).

94   Affar, E. B., Shah, R. G., Dallaire, A. K., Castonguay, V. & Shah, G. M. Role of poly(ADP-ribose) polymerase in rapid intracellular acidification induced by alkylating DNA damage. *Proc Natl Acad Sci U S A* **99**, 245-250. (2002).

95   Stringari, C. *et al.* Metabolic trajectory of cellular differentiation in small intestine by Phasor Fluorescence Lifetime Microscopy of NADH. *Sci Rep* **2**, 568. (2012).

96   Stringari, C., Sierra, R., Donovan, P. J. & Gratton, E. Label-free separation of human embryonic stem cells and their differentiating progenies by phasor fluorescence lifetime microscopy. *J Biomed Opt* **17**, 046012. (2012).

97   Skala, M. & Ramanujam, N. Multiphoton redox ratio imaging for metabolic monitoring in vivo. *Methods Mol Biol* **594**, 155-162, doi:10.1007/978-1-60761-411-1_11 (2010).

98   Ma, N., Digman, M. A., Malacrida, L. & Gratton, E. Measurements of absolute concentrations of NADH in cells using the phasor FLIM method. *Biomed Opt Express* **7**, 2441-2452, doi:10.1364/BOE.7.002441 (2016).

99   Nakamura, J. *et al.* Quantitation of intracellular NAD(P)H can monitor an imbalance of DNA single strand break repair in base excision repair deficient cells in real time. *Nucleic Acids Res* **31**, e104. (2003).

100   Heale, J. T. *et al.* Condensin I interacts with the PARP-1-XRCC1 complex and functions in DNA single-stranded break repair. *Mol Cell* **21**, 837-848., doi:10.1016/j.molcel.2006.01.036 (2006).

101   Cambronne, X. A. *et al.* Biosensor reveals multiple sources for mitochondrial NAD(+). *Science* **352**, 1474-1477, doi:10.1126/science.aad5168 (2016).

102   Kioka, H. *et al.* Evaluation of intramitochondrial ATP levels identifies G0/G1 switch gene 2 as a positive regulator of oxidative phosphorylation. *Proc Natl Acad Sci U S A* **111**, 273-278. (2014).

103   Imamura, H. *et al.* Visualization of ATP levels inside single living cells with fluorescence resonance energy transfer-based genetically encoded indicators. *Proc Natl Acad Sci U S A* **106**, 15651-15656. (2009).

104   Chen, Y., Chernyavsky, A., Webber, R. J., Grando, S. A. & Wang, P. H. Critical role of the neonatal Fc receptor (FcRn) in the pathogenic action of antimitochondrial autoantibodies synergizing with anti-desmoglein autoantibodies in pemphigus vulgaris. *J Biol Chem* **290**, 23826–23837. (2015).

105   Gey, C. & Seeger, K. Metabolic changes during cellular senescence investigated by proton NMR-spectroscopy. *Mech. Ageing Dev.* **134**, 130-138. (2013).

106   Gomez-Godinez, V. *et al.* Analysis of DNA double-strand break response and chromatin structure in mitosis using laser microirradiation. *Nucleic Acids Res* **38**, e202. (2010).

107   Kong, X. *et al.* Condensin I recruitment to base damage-enriched DNA lesions is modulated by PARP1. *PLoS One* **6**, e23548, doi:10.1371/journal.pone.0023548 (2011).

108   Silva, B. A., Stambaugh, J. R., Yokomori, K., Shah, J. V. & Berns, M. W. DNA damage to a single chromosome end delays anaphase onset. *J Biol Chem* **289**, 22771-22784., doi:10.1074/jbc.M113.535955 (2014).

109   Shiloh, Y. ATM and related protein kinases: safeguarding genome integrity. *Nat Rev Cancer* **3**, 155-168. (2003).

110   Burma, S., Chen, B. P., Murphy, M., Kurimasa, A. & Chen, D. J. ATM phosphorylates histone H2AX in response to DNA double-strand breaks. *J Biol Chem* **276**, 42462-42467. (2001).

111   Zheng, J. Energy metabolism of cancer: Glycolysis versus oxidative phosphorylation (Review). *Oncol Lett* **4**, 1151-1157. (2012).

112   Nickens, K. P., Wikstrom, J. D., Shirihai, O. S., Patierno, S. R. & Ceryak, S. A bioenergetic profile of non-transformed fibroblasts uncovers a link between death-resistance and enhanced spare respiratory capacity. *Mitochondrion* **13**, 662-667, doi:10.1016/j.mito.2013.09.005 (2013).

113   Scott, T. G., Spencer, R. D., Leonard, N. J. & Weber, G. Synthetic spectroscopic models related to coenzymes and base pairs. V. Emission properties of NADH. Studies of fluorescence lifetimes and quantum efficiencies of NADH, AcPyADH, [reduced acetylpyridineadenine dinucleotide] and simplified synthetic models. *J Am Chem Soc* **92**, 687-695. (1970).

114   Vishwasrao, H. D., Heikal, A. A., Kasischke, K. A. & Webb, W. W. Conformational dependence of intracellular NADH on metabolic state revealed by associated fluorescence anisotropy. *J Biol Chem* **280**, 25119-25126. (2005).

115   Yoshimura, M. *et al.* Vertebrate POLQ and POLbeta cooperate in base excision repair of oxidative DNA damage. *Mol Cell* **24**, 115-125. (2006).

116   Kim, J.-S. *et al.* Independent and sequential recruitment of NHEJ and HR factors to DNA damage sites in mammalian cells. *J Cell Biol* **170**, 341-347., doi:10.1083/jcb.200411083 (2005).

117   Zhou, B.-B. S. & Elledge, S. J. The DNA damage response: putting checkpoints in perspective. *Nature* **408**, 433-439 (2000).

118   Bekker-Jensen, S. *et al.* Spatial organization of the mammalian genome surveillance machinery in response to DNA strand breaks. *J Cell Biol* **173**, 195-206, doi:10.1083/jcb.200510130 (2006).

119   Aten, J. A. *et al.* Dynamics of DNA Double-Strand Breaks Revealed by Clustering of Damaged Chromosome Domains. *Science* **303**, 92-95 (2004).

120   Soutoglou, E. *et al.* Positional stability of single double-strand breaks in mammalian cells. *Nat Cell Biol* **9**, 675-682, doi:10.1038/ncb1591 (2007).

121   Bekker-Jensen, S., Lukas, C., Melander, F., Bartek, J. & Lukas, J. Dynamic assembly and sustained retention of 53BP1 at the sites of DNA damage are controlled by Mdc1/NFBD1. *J Cell Biol* **170**, 201-211, doi:10.1083/jcb.200503043 (2005).

122   Cardarelli, F. & Gratton, E. In vivo imaging of single-molecule translocation through nuclear pore complexes by pair correlation functions. *PLoS One* **5**, e10475, doi:10.1371/journal.pone.0010475 (2010).

123   Hinde, E., Kong, X., Yokomori, K. & Gratton, E. Chromatin dynamics during DNA repair revealed by pair correlation analysis of molecular flow in the nucleus. *Biophys J* **107**, 55-65, doi:10.1016/j.bpj.2014.05.027 (2014).

124   Kong, X. *et al.* Distinct functions of human cohesin-SA1 and cohesin-SA2 in double-strand break repair. *Mol Cell Biol* **34**, 685-698, doi:10.1128/MCB.01503-13 (2014).

125   Schindelin, J. *et al.* Fiji: an open-source platform for biological-image analysis. *Nat Methods* **9**, 676-682, doi:10.1038/nmeth.2019 (2012).

126   Lee, A. J., Warshaw, D. M. & Wallace, S. S. Insights into the glycosylase search for damage from single-molecule fluorescence microscopy. *DNA Repair (Amst)* **20**, 23-31, doi:10.1016/j.dnarep.2014.01.007 (2014).

127   Mugesh, G. 2015 Nobel Prize in Chemistry for DNA Repair. *Curr Science* **109**, 1533-1536 (2015).

128   Lieber, M. R., Ma, Y., Pannicke, U. & Schwarz, K. Mechanism and regulation of human non-homologous DNA end-joining. *Nat Rev Mol Cell Biol* **4**, 712-720, doi:10.1038/nrm1202 (2003).

129   Shao, Z. *et al.* Persistently bound Ku at DNA ends attenuates DNA end resection and homologous recombination. *DNA Repair (Amst)* **11**, 310-316, doi:10.1016/j.dnarep.2011.12.007 (2012).

130   Couto, C. A. *et al.* PARP regulates nonhomologous end joining through retention of Ku at double-strand breaks. *J Cell Biol* **194**, 367-375, doi:10.1083/jcb.201012132 (2011).

131   Bergter, A. & Huff, J. ZEISS LSM 880 with Airyscan: Introducing the Fast Acquisition Mode. *ZEISS Technology Note* (2016).

Supplemental Information for Chapter 3

A.1 Western blot for REV3L depletion by shREV3L
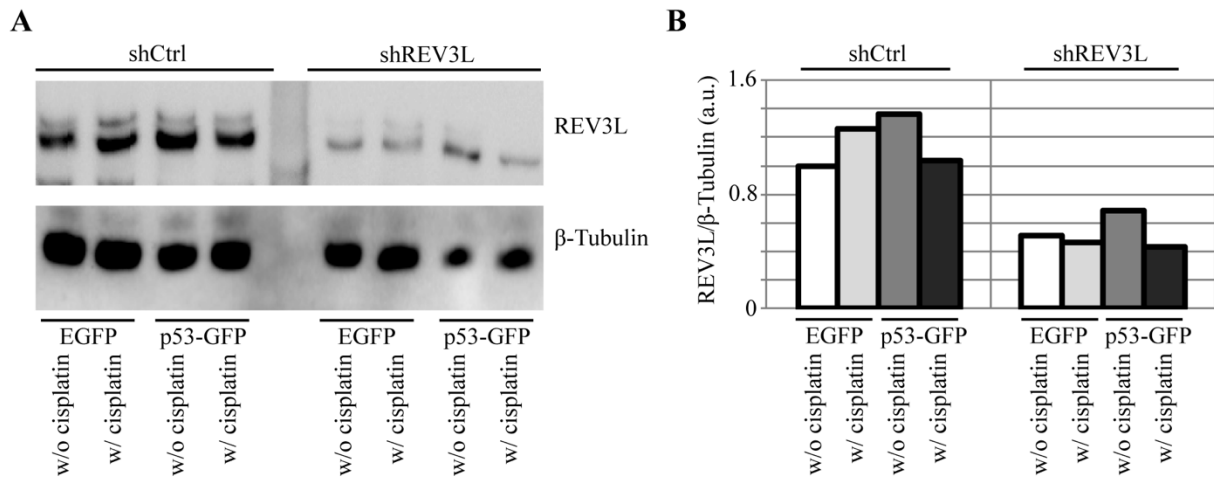
(A) Western blot for REV3L and β-tubulin. (B) Bar graph of the relative intensity of

REV3L/β-tubulin.

Supplemental Information for Chapter 4

B.1 Characterization of DNA damage and cell fate following laser microirradiation using different input power
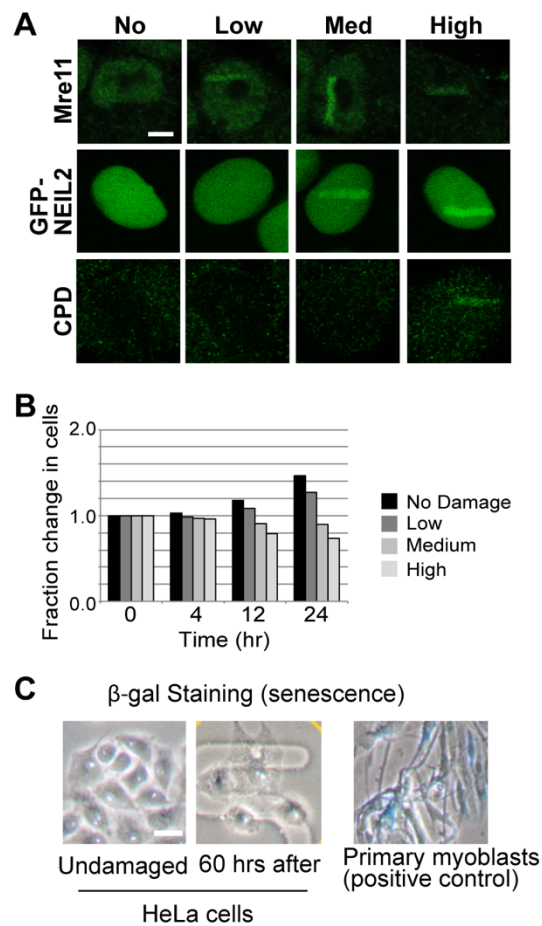

(A) Immuno-fluorescent staining for Mre11 (top) and CPD (bottom) in HeLa cells fixed at 1 hr post damage following low, medium, and high input laser power. Fluorescent images for

HeLa cells expressing GFP-Neil2 (middle) at approximately 2 min following low, medium, and high input laser power. Scale bar = 5 μm.

(B) The fraction change in the total number of HeLa cells over time following low, medium, and high input laser power.

(C) β-galactosidase staining of undamaged HeLa cells and cells at 60 hr post laser microirradiation at high input-power. Primary myoblasts were stained as a positive control. Scale bar = 20 μm.

B.2 Laser Damage Induces Dose-Dependent Decrease in NADH Intensity and Concentration
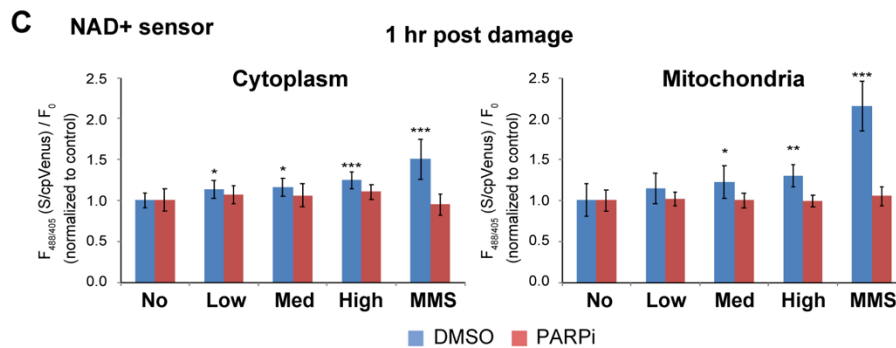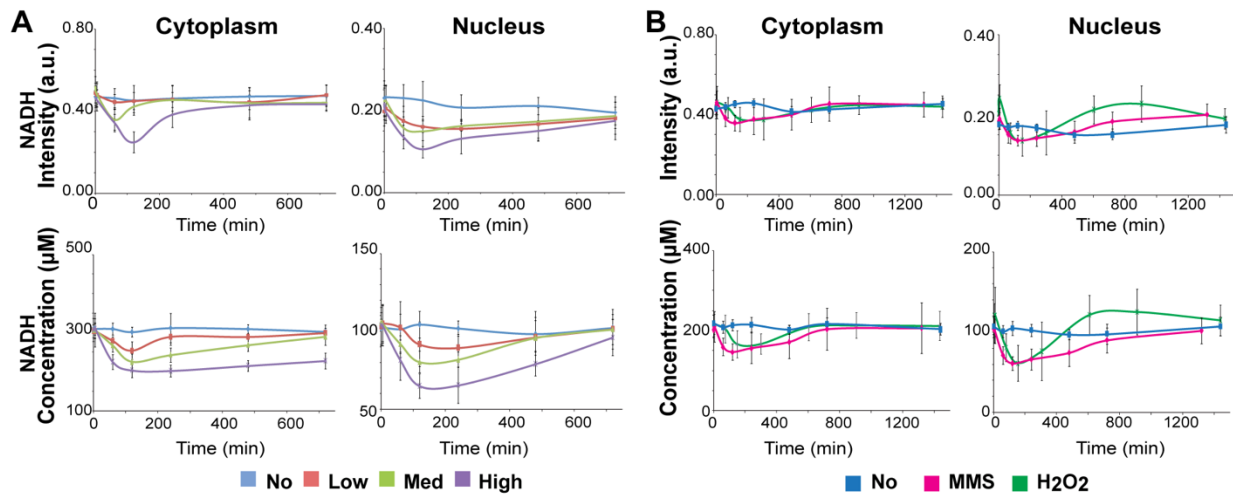
(A) The intensity of NADH and concentration of NADH over time in the cytoplasmic and nuclear compartments of HeLa cells following low, medium, and high input laser power.

(B) The intensity of NADH and concentration of NADH over time in the cytoplasmic and nuclear compartments of HeLa cells treated with either 1 mM MMS or 500 µM H_2O_2.

(C) The change in the ratiometric fluorescence intensity of the cytoplasmic or mitochondrial NAD+ biosensor at 1 hr post damage following low, medium, and high laser microirradiation or 3 mM MMS treatment for 1 hr. Cells were treated with either 0.1% DMSO or 20 µM PARP inhibitor (olaparib). An increased fluorescence ratio reflects decreased NAD+ binding. * $p < 0.05$, ** $p < 0.01$, *** $p < 0.001$.

B.3 Damage-induced changes in NADH intensity and FLIM images are PARP, but not ATM/DNA-PK,-dependent
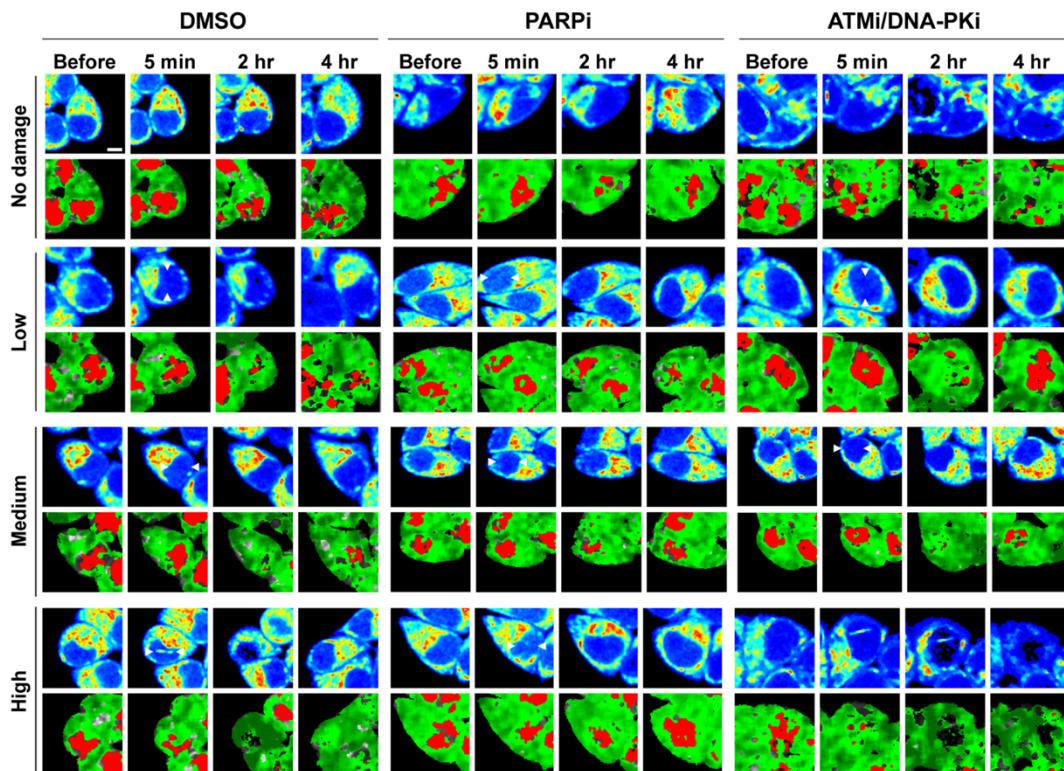
Intensity (top) and pseudo-colored FLIM (bottom) images of undamaged HeLa cells and HeLa cells damaged at low, medium, and high input laser power and treated with either 0.1% DMSO (left), 20 μM PARP inhibitor (olaparib) (middle), or 10 μM ATM inhibitor (KU55933) and 10 μM DNA-PK inhibitor (NU7026) (right). In intensity images, the line color from blue to red corresponds to the normalized intensity. Damage sites are indicated by white arrows. The FLIM images are pseudo-colored according to the clusters selected on the phasor plot in (Figure 4.1B). Scale bar = 5 μm.

B.4 Damage-specific cell death induced by R+A treatment is AIF-independent apoptosis
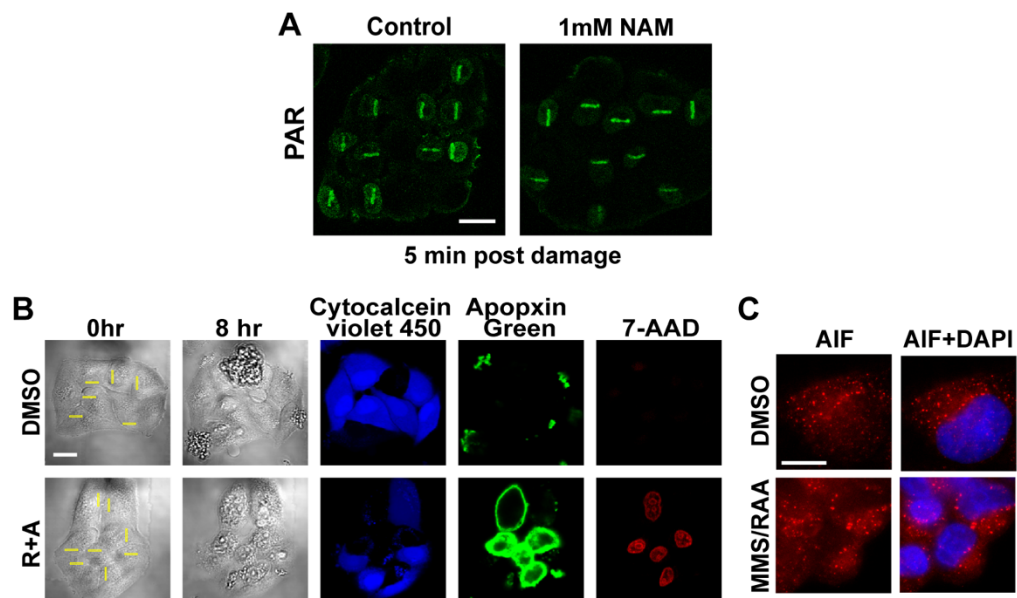

(A) Immuno-fluorescent staining for PAR (green) in HeLa cells pre-treated with or without 1 mM NAM for 1 hr and fixed 5 min post damage following low, medium, and high input laser power. Scale bar = 20 μm.

(B) Brightfield images of HeLa cells treated with either 0.2 % DMSO or 1 µM rotenone and 1 µM antimycin A before damage and 8 hr post damage. Apoptosis and necrosis was detected using a commercial kit (AB176749) for live cells (cytocalcein violet 450, blue), phosphatidylserine exposure (apopxin green, green), and loss of plasma integrity (7-aminoactinomycin D, red). Scale bar = 20 µm.

(C) Immuno-fluorescent staining for apoptosis inducing factor (AIF) and DAPI in HeLa cells treated with either 0.1% DMSO or 1 mM MMS, 1 µM rotenone, and 1 µM antimycin A. Scale bar = 10 µm.

B.5 Intracellular pH (pHi) measurement using pHrodo Green AM reveal significant damage-specific acidification by R+A, which is alleviated by PARPi but not by NAM
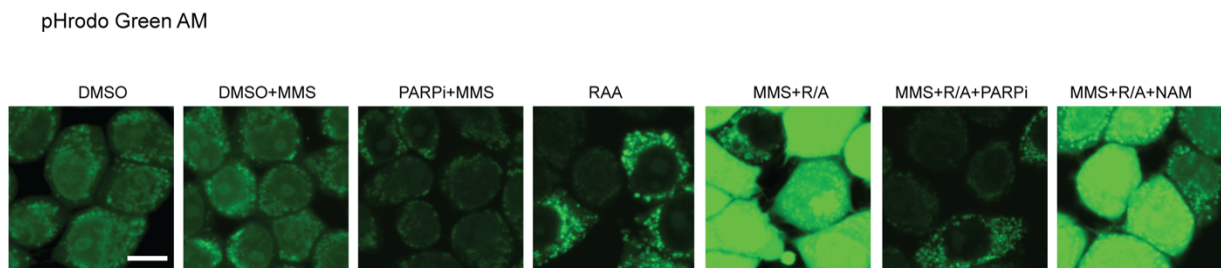

Fluorescence images of HeLa cells were treated with indicated chemicals with or without MMS damage induction for 1 hr with pHrodo Green AM. Relative fluorescence intensities were quantified in Fig. 4.7C where higher intensities correspond to lower pH. Scale bar = 10 µm.

APPENDIX C

Supplemental Information for Chapter 5

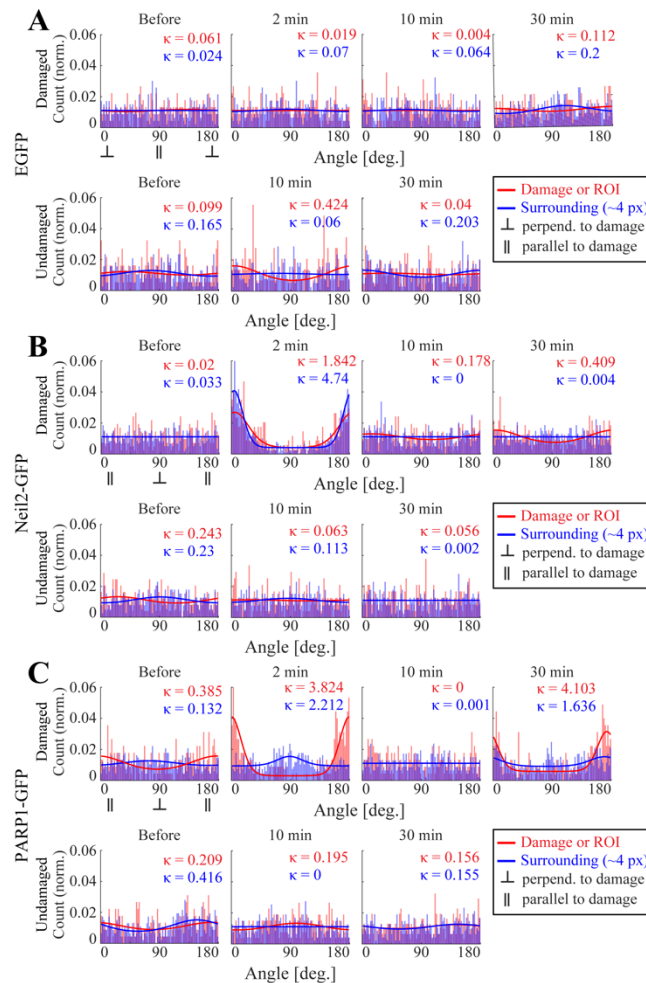### C.1 Anisotropy and von Mises probability density function analysis of Ku-GFP in region surrounding damage site
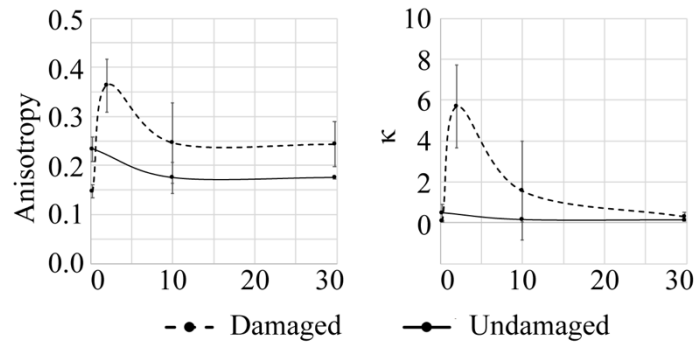
(A) Bar graph of the average anisotropy over time in the region surrounding the damage site. (B) Bar graph of the change in κ parameter of the von Mises probability density function analysis over time in the region surrounding the damage site.

C.2 Laser microirradiation recruits Ku-GFP to damage site and results in loss of H2B-mCherry signal
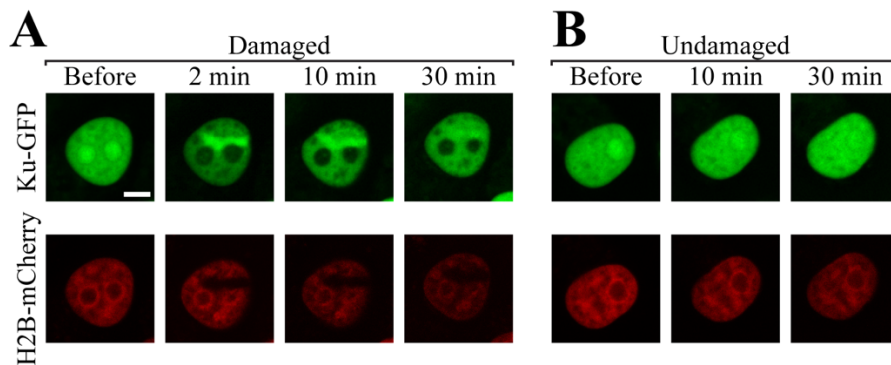
Fluorescence intensity images of (A) damaged or (B) undamaged HeLa cells expressing Ku-GFP and H2B-mCherry.

C.3 von Mises probability density function analysis of EGFP, Neil2-GFP, or PARP1-GFP following microirradiation

The 2D-pCF is calculated for HeLa cells expressing (A) EGFP, (B) Neil2-GFP, or (C) PARP1-GFP. The von Mises probability density function represents the preferential orientation of anisotropy within the damage site (red) or in the region surrounding the damage site (blue, within 4 pixels) (top row). The symbols $\perp$ and || indicate a preferred orientation

perpendicular and parallel to the length of the rectangular region of damage, respectively. The von Mises function for non-microirradiated region of interest (ROI, red) or in the region surrounding the ROI (blue) (bottom row).